Cite as: ReLUIS-INGV Workgroup (2016), *Preliminary study on strong motion data of the 2016 central Italy seismic sequence V6*. available at http://www.reluis.it.

PRELIMINARY STUDY ON STRONG MOTION DATA OF THE 2016 CENTRAL ITALY SEISMIC SEQUENCE V6

INGV: ITACA-ESM Working Group,[1] SHAKEMAP working group.[2]

ReLUIS: Iunio Iervolino (iunio.iervolino@unina.it),[3] Georgios Baltzopoulos,[4] Eugenio Chioccarelli,[4] Akiko Suzuki.[3]

Warning: This report may be subjected to editing and revisions. In particular, data status is that of November 8 2016. A revision is possible after all data provided at ran.protezionecivile.it will be fully consolidated. Check www.reluis.it, esm.mi.ingv.it and www.itc.cnr.it for updates. [Ver. date: Dec. 11 2016]

INDEX

[1] The ITACA-ESM Working Group is: Lucia Luzi (lucia.luzi@ingv.it); Francesca Pacor; Rodolfo Puglia; Maria D'Amico; Emiliano Russo; Chiara Felicetta; Giovanni Lanzano. INGV-Milano, Italy.
[2] The SHAKEMAP Working Group is: Alberto Michelini (alberto.michelini@ingv.it); Licia Faenza; Valentino Lauciani. INGV-CNT, Italy.
[3] Dipartimento di Strutture per l'Ingegneria e l'Architettura, Università degli Studi di Napoli Federico II, Italy.
[4] Istituto per le Tecnologie della Costruzione ITC-CNR, URT Università degli Studi di Napoli Federico II, Italy.

1. What's New

This report was formerly titled PRELIMINARY STUDY OF RIETI EARTHQUAKE GROUND MOTION DATA as it dealt with the event occurred on August 24 2016. This version contains information regarding the whole seismic sequence, with specific reference to the three largest earthquakes occurring until October 30 2016 (some analyses include the fourth largest-magnitude earthquake). In particular this report focuses on the sequence as a whole and on the analysis of ground motions from different events recorded at sites in the vicinity of the sources.

2. Introduction

The Italian Accelerometric Network (RAN), managed by the Department of Civil Protection (DPC), and the Italian seismic network (RSN), managed by the Istituto Nazionale di Geofisica e Vulcanologia (INGV) have made available the records of the recent earthquakes with epicenters located in the area between the villages of Amatrice and Visso, central Italy (24/08/2016 1.36:32 UTC, Mw 6.0; 26/10/2016 19:18:06 Mw 5.9; 2016-10-30 06:40:18, Mw 6.5; ref. Bollettino Sismico INGV).

About 650 accelerometric signals, manually processed using the procedure by Paolucci et al (2011), are used to evaluate the peak ground motion, acceleration and displacement spectral ordinates, integral parameters and measures of duration. **Corrected records and details of correction are available on the Engineering Strong-Motion database website (http://esm.mi.ingv.it). The unprocessed records are available at http://ran.protezionecivile.it/IT/index.php?evid=340867 for the RAN network and at the European Integrated Data Archive (http://www.orfeus-eu.org/data/eida/) for the RSN, that also distributes local networks (University of Genova, University of Trieste, OGS, AMRA, among others).**

In order to analyze peak values and spectral acceleration (Sa or PSA), data have been processed and compared to the Ground Motion Prediction Equation (GMPE) by Bindi et al (2011) and Akkar et al (2014) for rock and soil. The geometric mean of the horizontal components and the vertical component are used in the analysis. The median of the GMPE (and its standard deviation) is compared to the observations at various stations.

Peak Ground Acceleration (PGA), *Peak Ground Velocity* (PGV) and *Peak Ground Displacement* (PGD), *Arias Intensity* (I_A) and Housner Intensity (or spectral intensity - SI) are calculated for the three components of ground motion for the stations closest to the epicentre. Durations is also computed for each record as *Significant Duration*, estimated between 5% and 95% (D_{5-95}) and between 5% and 75% (D_{5-75}) of the I_A.

3. Geographic Information

The first strong earthquake of the sequence (Mw 6.0) struck central Italy on 2016-08-24 at 01:36:32 GMT, in the vicinity of Amatrice, causing diffuse building collapse and about 300 casualties. After 2 months, on 2016-10-26 two events of moment magnitude 5.4 (17:10:36 UTC) and 5.9 (19:18:06 UTC) extended to the NW the seismogenic volume. After 4 days, on 2016-10-30 at 06:40:18 UTC an event of Mw 6.5, struck the area corresponding to the Sibillini mountains with epicenter located in the vicinity of Norcia.

The four events have been caused by normal faulting, the prevalent style of faulting in the area, all of them having NW-SE or NNW-SSE strike and dip towards SW. The location of the three epicentres together with events having magnitude larger than 4.0 is shown in Figure 3.1.

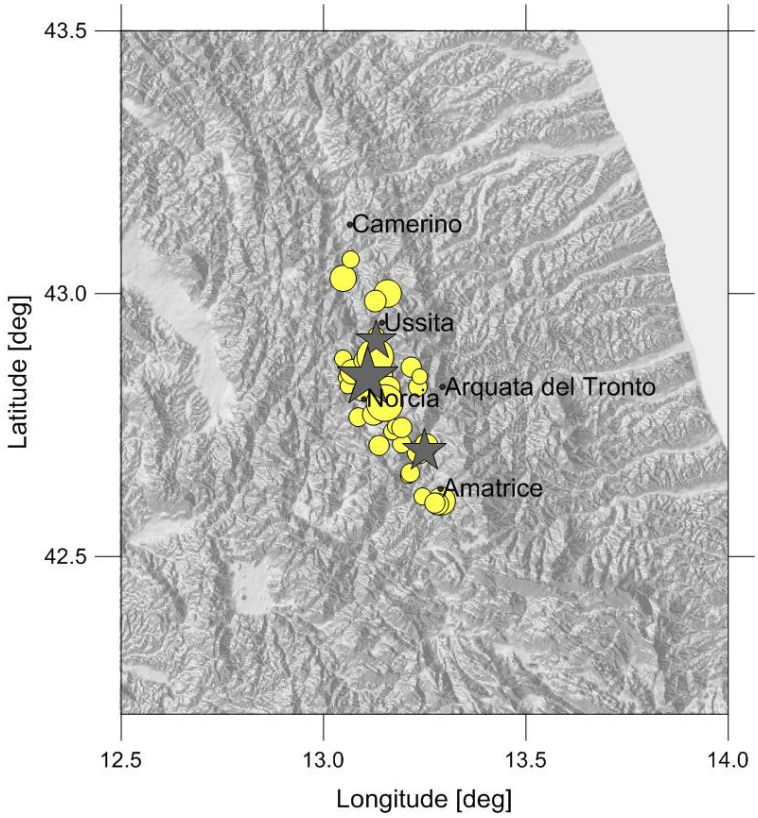

Figure 3.1: Epicentres of the events with M >= 4.0 in period time from 24-08-2016 to 3-11-2016. The size of the symbols is proportional to the magnitude. The grey stars represent the three mainshocks: Amatrice, 24-08-2016, Mw 6.0; Ussita, 28-10-2016, Mw 5.9 and Norcia, 30-10-2016, Mw 6.5 (coordinates from http://cnt.rm.ingv.it/).

The seismic sequence struck an area where several large earthquakes occurred in the past; in particular, a long lasting seismic sequence that affected the central-southern Apennines in the 18th century is well documented. According to the most recent historical catalog CPTI15 (Rovida et al., 2016 **http://emidius.mi.ingv.it/CPTI15-DBMI15/**, updated to 2015) the strongest earthquake of the area occurred on 1703 (Norcia, Io = 11) that destroyed large part of the villages in the neighborhood of Norcia (Figure 3.2).

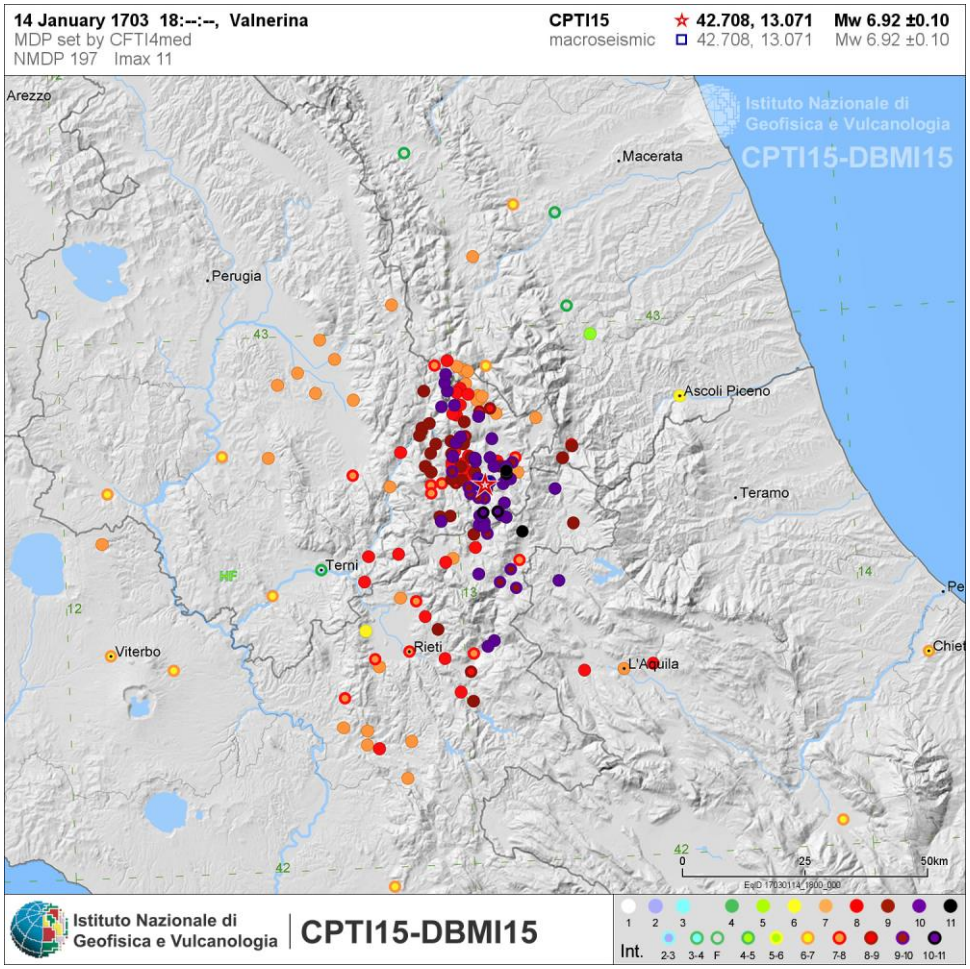

Figure 3.2: macroseismic field of the 1703 (Io = 11) Norcia earthquake (from http://emidius.mi.ingv.it/CPTI15-DBMI15/)

4. Strong Motion Data

The Italian Accelerometric Network (RAN), managed by the Department of Civil Protection (DPC), and the Italian seismic network, managed by the Istituto Nazionale di Geofisica e Vulcanologia (INGV) have made available the records of about 650 accelerometric stations. Figure 4.1 shows the the distribution of the closest strong-motion stations of the three main events. Each earthquake has been recorded by about 100 stations within 100 km from the epicentre and about 10 stations within 10 km.

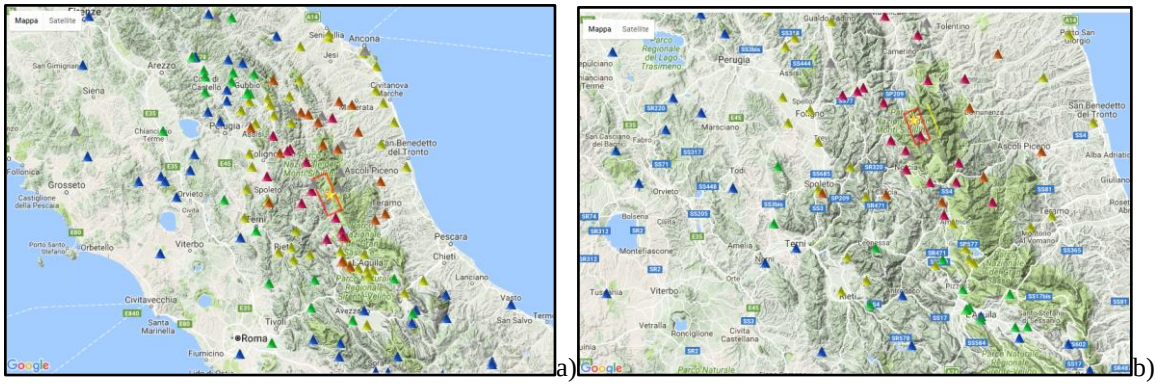

AMATRICE EARTHQUAKE, Mw 6.0 USSITA EARTHQUAKE, Mw 5.9

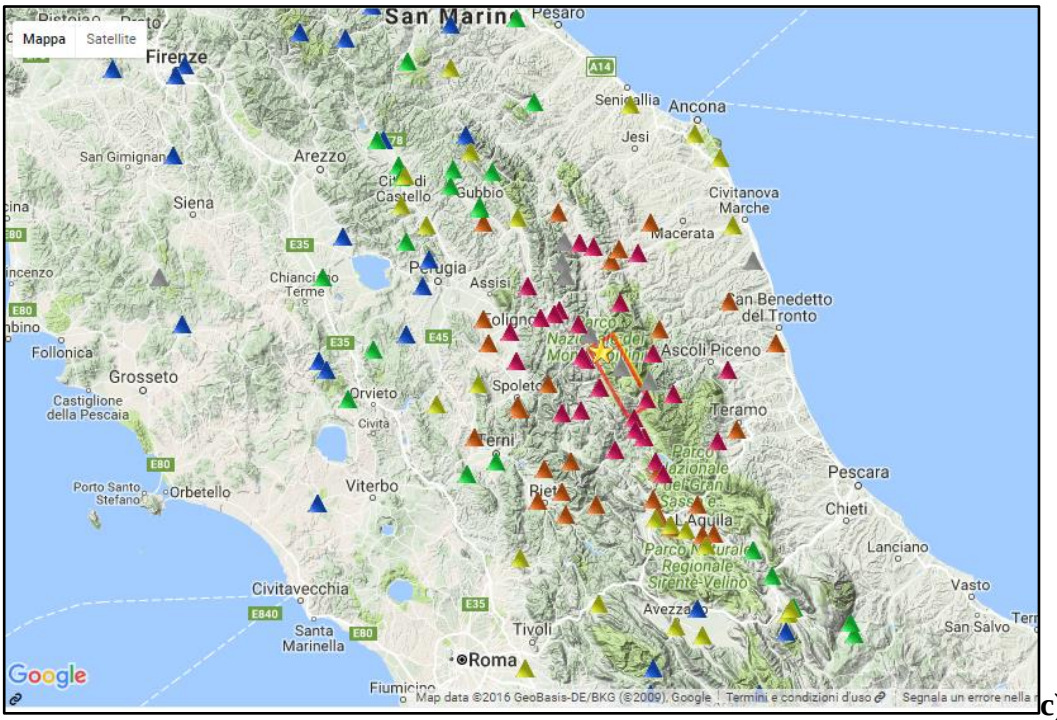

NORCIA EARTHQUAKE, Mw 6.5

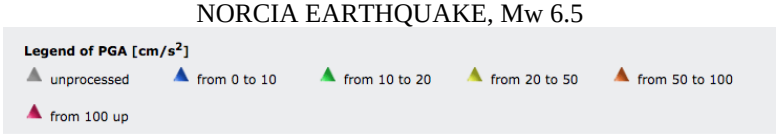

Figure 4.1: location of the epicentres (yellow star) and strong motion stations within 150 km from the epicenter of a) 2016-08-24 Mw 6.0; b) 2016-10-26 Mw 5.9; c) 2016-10-30 Mw 6.5. The triangles indicate strong-motion stations and the colors correspond to the PGA values (gal). The red boxes are the surface fault projections: the fault geometries are preliminary for the Ussita and Norcia events.

Among data released officially so far, the largest Peak Ground Acceleration (PGA) among the three events have been recorded at short epicentral distances (< 15 km) at the stations Campi (CMI, 638 gal, E-W processed waveform), Norcia (NRC, 376.96, N-S component) and Arquata del Tronto (RQT, 447.87 gal, E-W component; N-S component not available). Figures 4.2 to 4.5 are the maps showing the spatial distribution of the peak ground values. Note however that the station of Forca Canapine (FCC shows PGA of about 1g) and although it is going further revisions its spectrum is discussed in section 8.

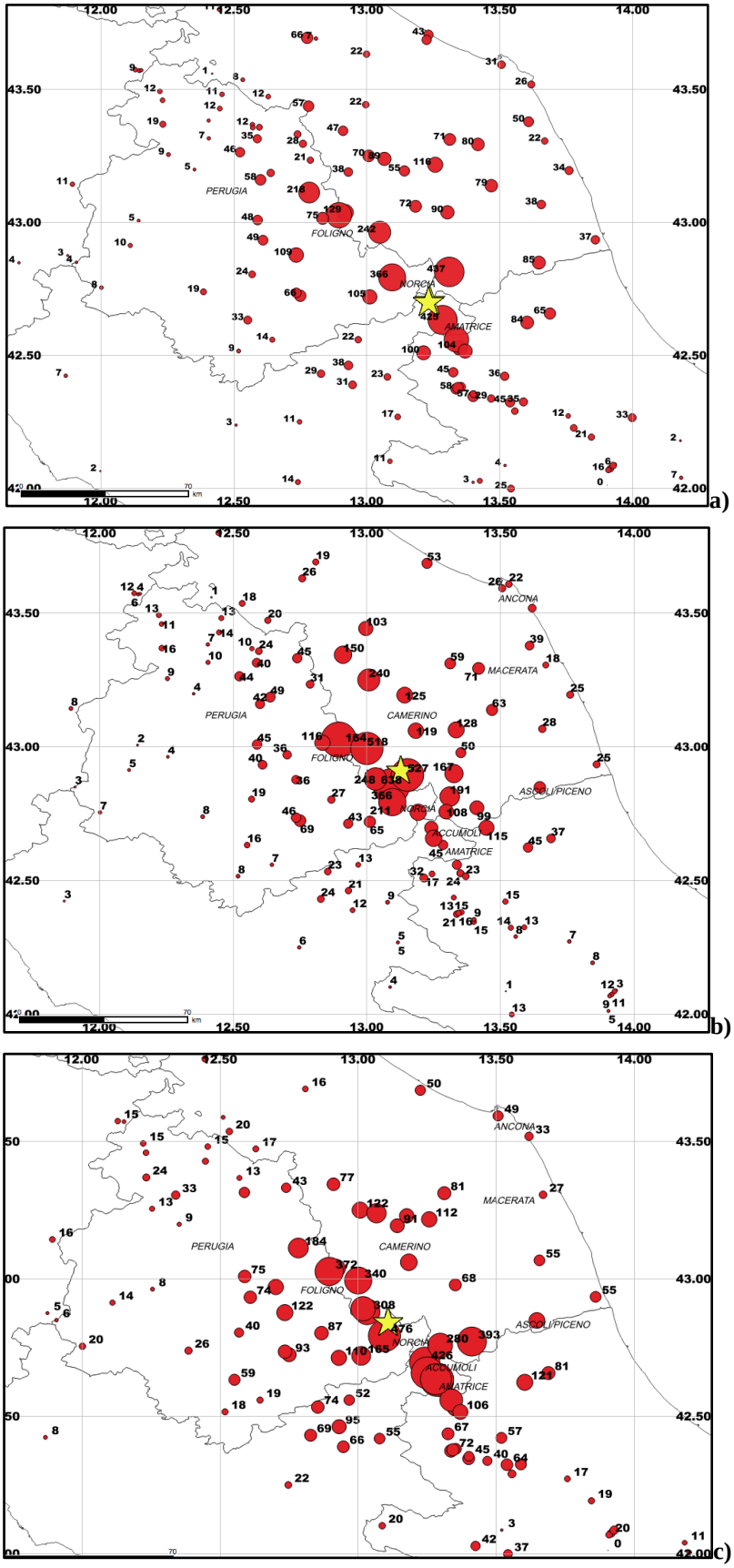

Figure 4.2 Map of the Peak Ground Acceleration (maximum between E and N components, cm/s^2). The star indicates the epicenter of the mainshock. a) Amatrice, M 6.0, b) Ussita, M 5.9, c) Norcia, M 6.5.

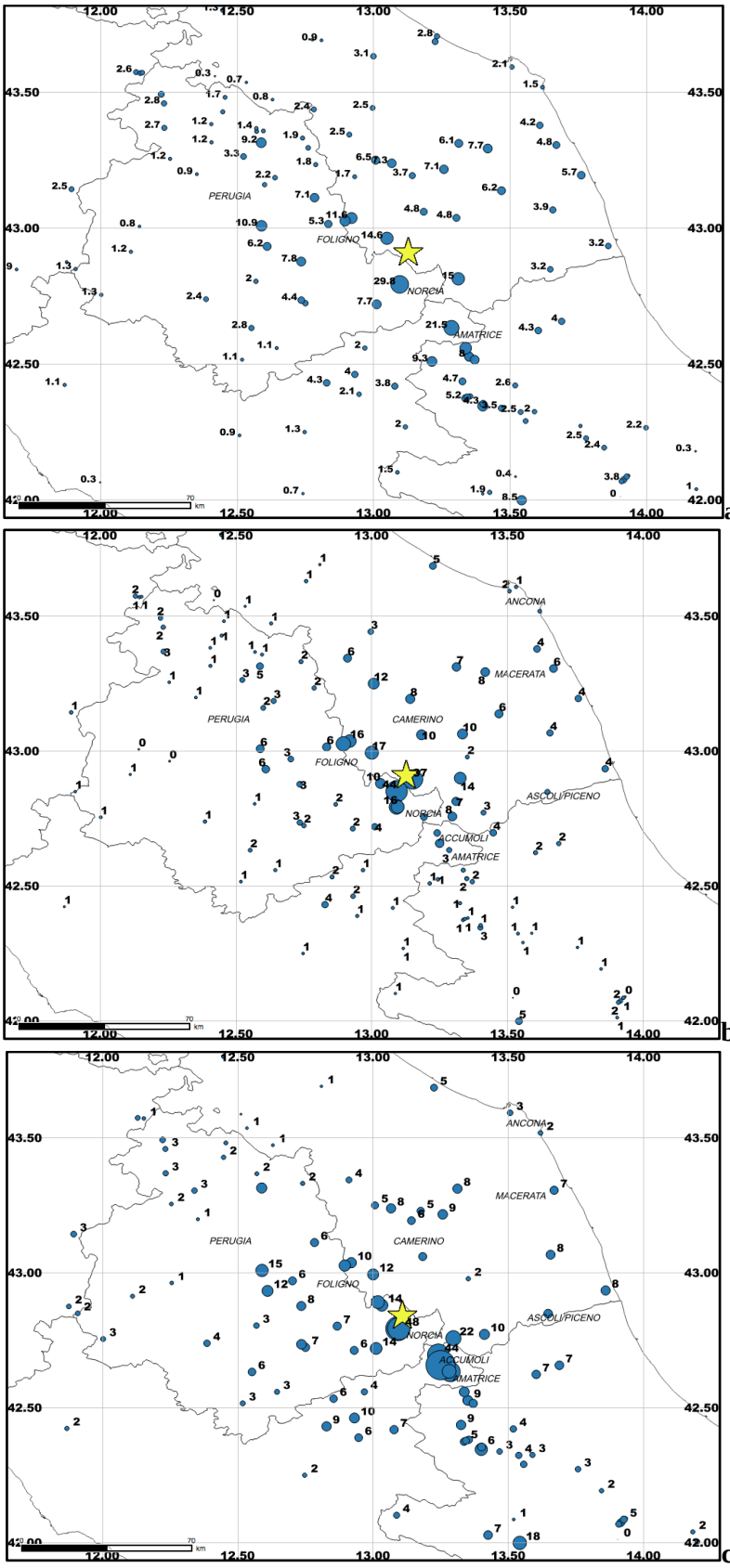

Figure 4.3 Map of the Peak Ground Velocity (maximum between E and N components, in cm/s). The star indicates the epicenter of the mainshocks. a) Amatrice, M 6.0, b) Ussita, M 5.9, c) Norcia M 6.5.

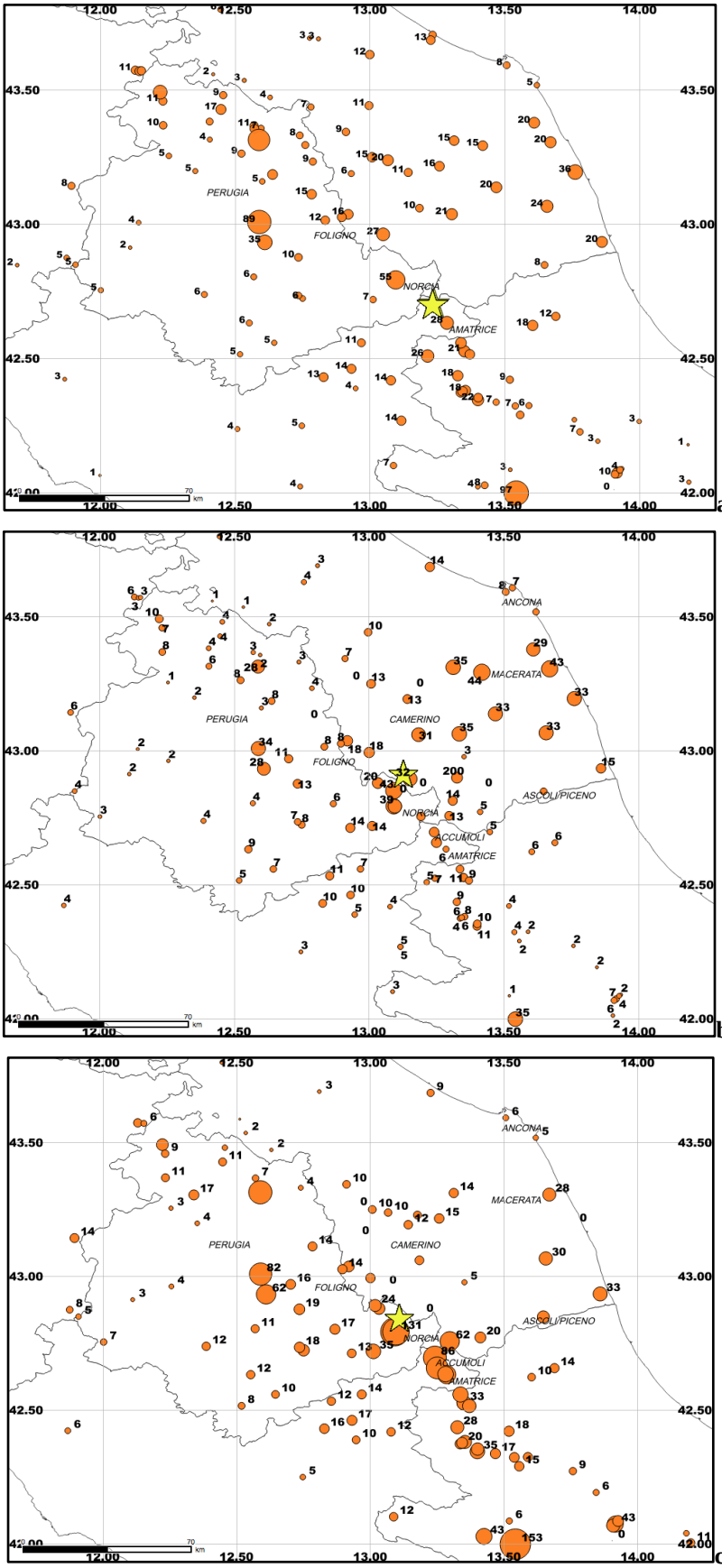

Figure 4.4. Map of the Spectral Acceleration at T = 3s (maximum between E and N components, cm/s^2). The star indicates the epicenter of the mainshocks. a) Amatrice, M 6.0, b) Ussita, M 5.9, Norcia, M 6.5.

Figures 4.5 and 4.6 show the direction of the maximum horizontal and vertical peak displacements and velocities for the Norcia, Mw 6.5, earthquake. The horizontal directions have been calculated rotating the E and N components by steps of 10 degrees and identifying the largest value and the corresponding azimuth.

The largest horizontal displacements and velocities are observed in the fault normal direction.

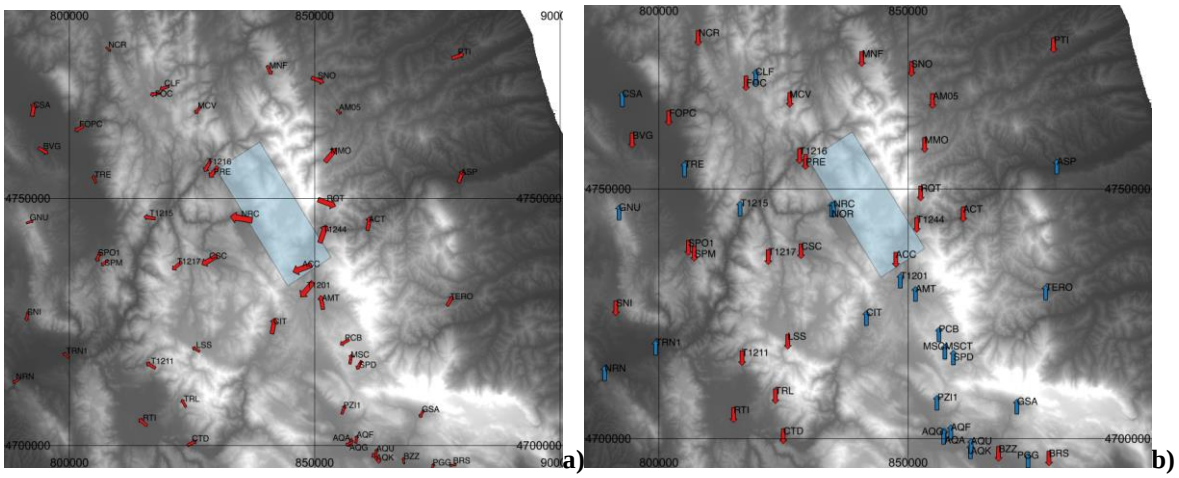

Figure 4.5. Map of the direction of the maximum peak displacement for the Norcia, M 6.5, event. a) Horizontal component; b) vertical component.

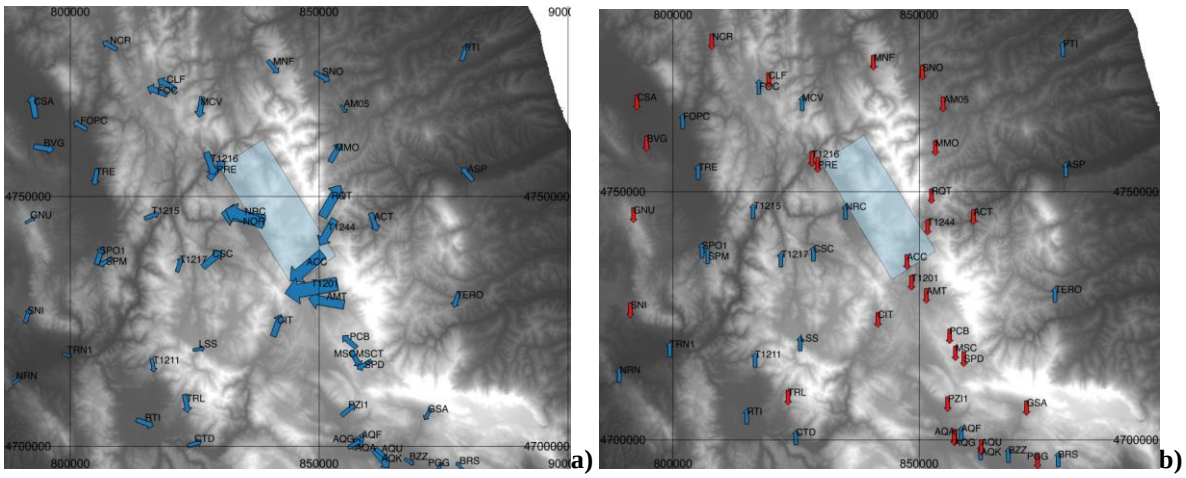

Figure 4.6. Map of the direction of the maximum peak velocity for the Norcia, M 6.5, event. a) Horizontal component; b) Vertical component.

5. SHAKEMAPS

The distribution of the ground shaking has been determined using the ShakeMap software (Wald et al., 1999; Michelini et al., 2008). Shakemaps are routinely calculated at INGV (http://shakemap.rm.ingv.it) using the same accelerometric data described in the previous section and the non-saturated broadband recordings. Data

processing is performed through an automatic procedure and they are published in a few minutes from the earthquake occurrence. As the manually revised PGM data become available in the ESM DB, a procedure has been implemented to update the maps using these better quality manually processed and revised data. For relevant earthquakes (M>=5.5), fault finiteness is important and a manual procedure is in place to insert the fault based on the parameters provided by the moment tensor inversion mechanism (Scognamiglio et al., 2009), the moment magnitude and the scaling laws developed by Wells and Coppersmith (1994). The MCS instrumental intensity (Faenza and Michelini, 2010, 2011), PGA and PGV shakemaps of the three main shocks (M6.0, M5.9 and M6.5) are shown in Figures 5.1-5.3.

The MCS instrumentally derived intensity maps show at a glance the different levels of ground shaking produced by the three earthquakes. Specifically, the maps of Fig. 5.1 show remarkable differences although the earthquakes are very close and feature very similar normal fault mechanisms.

The maps in MCS intensity (Fig. 5.1) identify well the areas most affected by the three main shocks (VII+). For the M6.0 August 24 earthquake, the PGA shakemaps show that the region close to the fault(s) experienced PGAs larger than 40%g at the closest stations and PGVs larger than 20 cm/s. The pattern of the PGA ground motion indicates a larger lobe toward the N-NW (Fig. 5.2) consistent with the preliminary findings obtained from the rapid finite fault inversion of Tinti et al. (2016). To some degree the same pattern is observable also on the PGV shakemaps (Fig. 5.3). The area that suffered VI-VII MCS intensities is approximately 100x100 km^2.

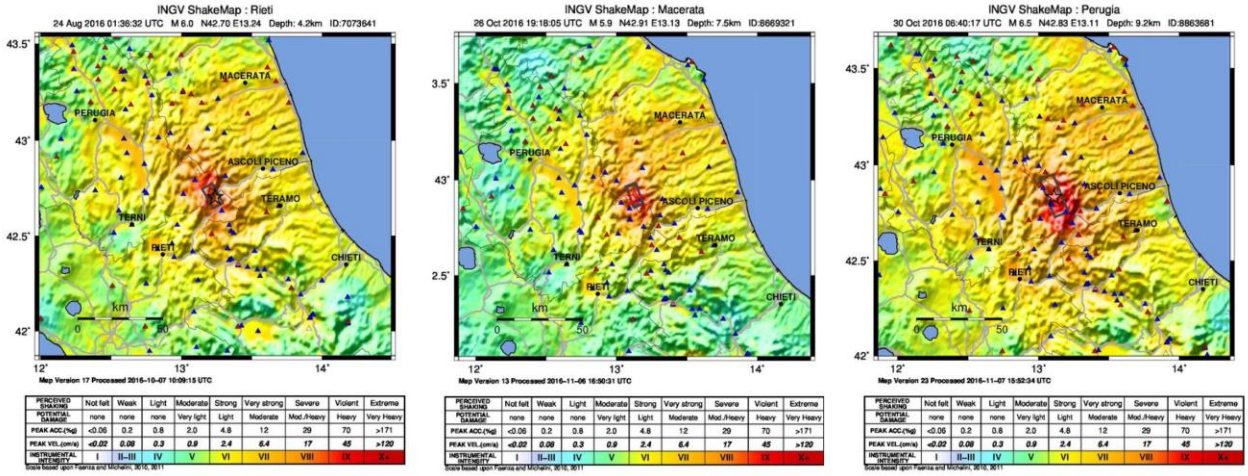

Fig. 5.1. MCS instrumental intensity shakemaps of the three main shock of the sequence. M6.0 August 24, 2016 (left), M5.9 October 26, 2016 (center), M6.5 October 30, 2016 (right).

The shakemaps of the M5.9 earthquake on October 30 (center panels in Fig. 5.1, 5.2 and 5.3) show a pattern of MCS intensities that differs significantly from that of the 6.0 August 24, 2016, main shock. Peak accelerations larger than 50%g have been recorded at stations CNE and CMI (65%g) and peak ground velocities above 35 cm/s at the same stations, both very close or above the finite causative fault. Of importance are the larger peak ground motion values (and associated instrumental intensities) observed north of the epicenter. The MCV station to the north of the earthquake epicenter (~14 km) recorded PGA values ~53%g. The overall area affected displaying intensities VI-VII is slightly smaller than that of the August 24 earthquake but the PGV maps evidence a prominent lobe of the 9 cm/s contour line to the north of the causative fault.

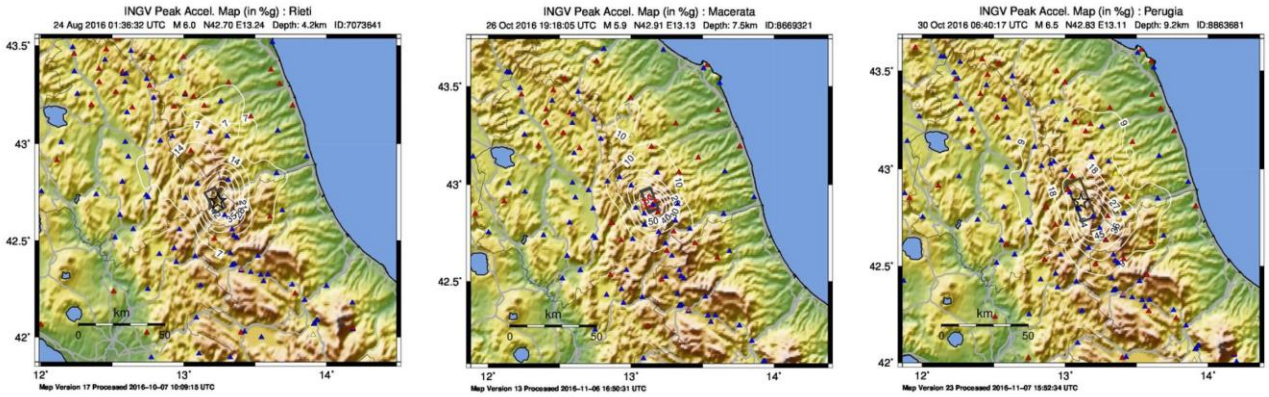

Fig. 5.2. PGA shakemaps of the three main shock of the sequence. M6.0 August 24, 2016 (left), M5.9 October 26, 2016 (center), M6.5 October 30, 2016 (right).

The shakemaps of the M6.5 October 30 earthquake - the largest shock of the sequence as the writing of this report - show, because of the larger earthquake size (~8 and ~5 times bigger than the M5.9 and M6.0 earthquakes, respectively), an overall larger area affected by the VI-VII intensities when compared to the previous earthquakes. The intensity VIII+ area is located toward the south of the fault displayed in the map. PGAs close or larger than 50%g have been recorded at several stations next to the epicenter with a prominent lobe of both the acceleration and peak ground velocities to the SE of the epicenter. Specifically, ground velocities larger than 40 cm/s were recorded both next to the epicenter (NRC and NOR stations in Norcia) and to the SE as far south as 20 km from the epicenter at ACC (Accumoli).

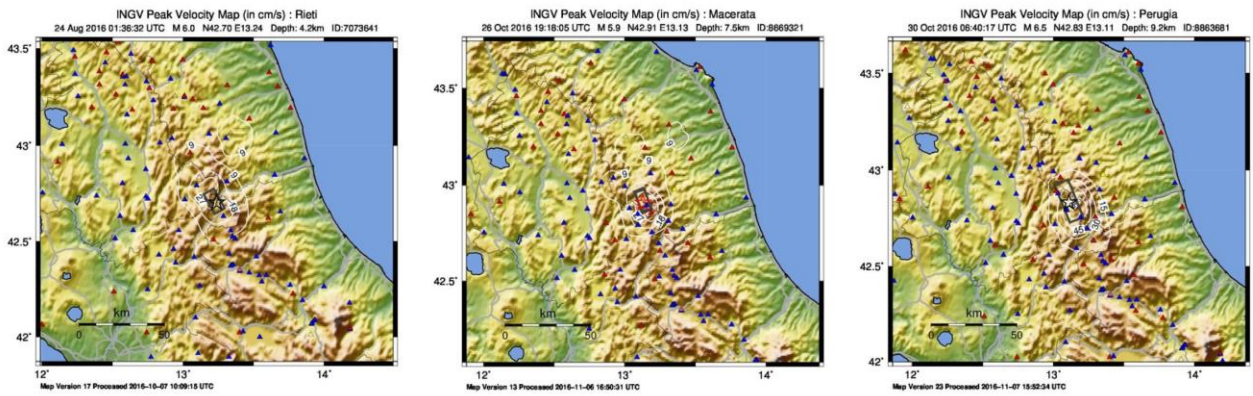

Fig. 5.3. PGV shakemaps of the three main shock of the sequence. M6.0 August 24, 2016 (left), M5.9 October 26, 2016 (center), M6.5 October 30, 2016 (right).

In order to evidence the differences between the different ground shaking produced by the three main shocks of the sequence, we have calculated the decimal logarithm of the ratio between the PGA and PGV shakemap (Fig. 5.4 and 5.5). In addition and in order to display the difference over a larger area, we have extended the

shakemap calculation to include the whole central part of the Italian peninsula (top panels of Figs. 5.4 and 5.5).

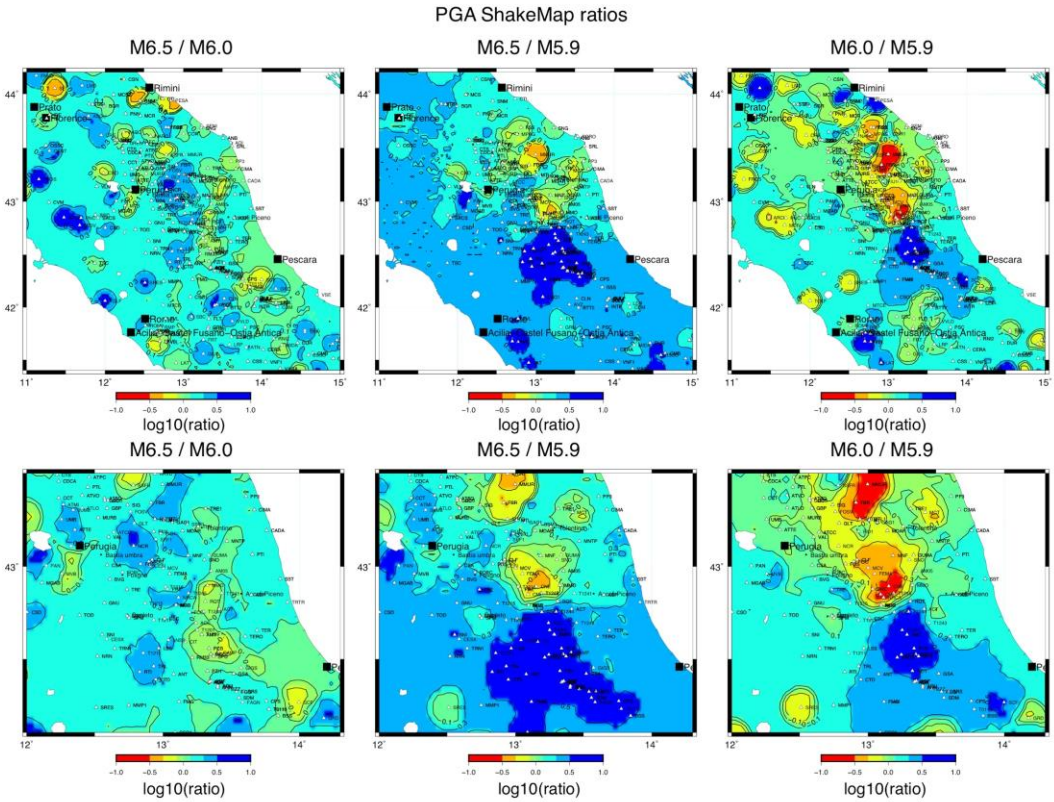

Fig. 5.4. PGA shakemap ratios calculated at regional scale (top) and at the same scale as the maps shown in Figures 5.1-5.3 (bottom). The base 10 logarithm is applied to the ratios determined over PGA values 2 minutes grid spaced.

For simplicity in the description below we will refer to the three main shocks according to their magnitude and indicate M6.5/M6.0 the ratio between the events of October 30 and August 24, M6.5/M5.9 for ratio between the events of October 30 and October 26 and M6.0/M5.9 the ratio between the August 24 and October 26 events. We see that the shakemap ratios maps evidence quite well the main differences between the strong ground motion shaking resulting from the three shocks. Overall we see that the M6.5/M6.0 PGA and PGV ratios evidence overall larger values of the ground shaking throughout most of the area. There are zones, however, of somewhat smaller relative values of the shaking produced by the M6.5 when compared to the M6.0 to indicate that despite the larger magnitude and very similar focal mechanisms other factors can affect ground motion locally. These include rupture directivity primarily. The M6.5/M5.9 ratio is quite interesting since, despite the two epicenters occur less that 8 km away and the size of the two earthquakes is different, we observe that the area NW of the M5.9 earthquake suffered higher levels of ground shaking (e.g., the historical town of Camerino was severely damaged by the M5.9). This increased level of ground motion is likely the result of NW source directivity. This difference in the level of ground shaking produced by the M5.9 is even more clear when

compared to the M6.0 that, however, was almost 25 km away. In general the two "< 0.0" ratio lobes observable on NW of the M5.9 earthquake for both the M6.5 and M6.0 indicate more similarity between the two latter shocks when compared to the M5.9.

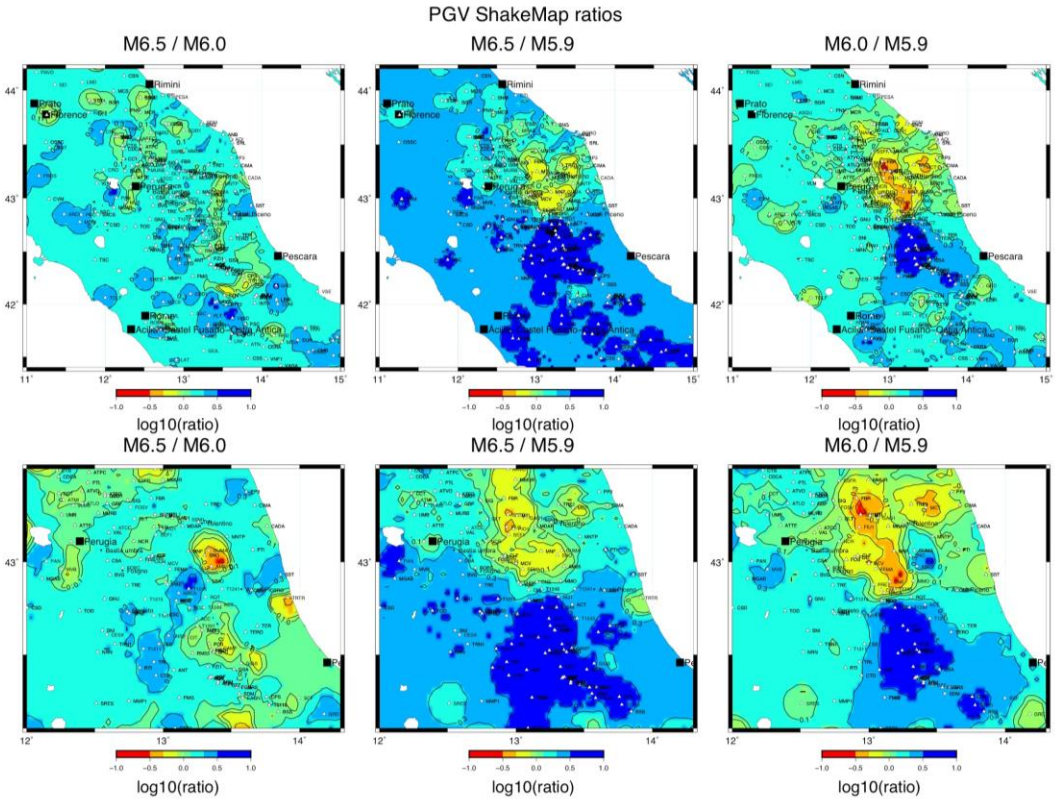

Fig. 5.5. Same as Figure 5.4 for the PGV shakemap ratios.

6. Comparison with GMPE

Some horizontal GM parameters are compared to the predictions by Bindi et al (2011) Ground Motion Prediction Equation (ITA10), valid for Italian territory and Akkar et al. (2014) GMPE (ASB14), calibrated with European strong motion data. The vertical components have been compared to the Bindi et al (2010) as Akkar et al (2014) provides coefficients only for the horizontal components of ground motion. The predictions are computed for moment magnitude values and for Joyner-Boore distances. The parameters of the fault geometries adopted to compute the distances are reported in Table 1

Table 1. Parameters of the causative faults of the three main events

	Amatrice	**Ussita**	**Norcia**
Strike/Dip [°]	156/50	159/47	151/47
Length/Width [Km]	26/16	11/7.56	30/16
Mw	6.0	5.9	6.5
Reference	Tinti et al., 2016a	Tinti et al., 2016b	ESM

The results of the comparison can still be considered as preliminary since: i) the Joyner-Boore distance has been estimated using the preliminary fault plane geometries for Ussita and Norcia earthquakes; ii) the comparison at 3s is outside the range of validity of the Bindi et al (2010), as authors recommend its up to 2s.

We calculated the prediction for: PGA, PGV, SA at 0.3s, 1s and 3s (the intensity measures used for shakemaps) for the geometric mean of the horizontal components and the vertical component. For the vertical component, the SA at 3s was not implemented by the Bindi et al (2010), therefore we evaluated the goodness of fit at 2s. Figures from 6.1 to 6.10 show the comparison between observations and GMPEs for peak ground acceleration and velocity, for the Ec8 (CEN 2003) soil categories (class A: Vs30 > 800 m/s; class B: Vs30 = 360 − 800 m/s; class C: Vs30 = 180 − 360 m/s; class D: Vs30 < 180 m/s; class E: 5 to 20 m of C- or D-type alluvium underlain by stiffer material with Vs30 > 800 m/s, where Vs30 is the average shear wave velocity in the uppermost 30 m).

The main difference between GMPEs is the modelling of site effects. While Bindi et al (2010) accounts for linear site effects, through soil classes, Akkar e al (2014) consider a nonlinear behaviour of soils. In particular, the non-linear site term depends on the PGA at the reference site, that is the larger the PGA at the reference site the larger the non-linear site effects. The major differences between GMPEs are in fact observed at large magnitudes and at long periods.

For the horizontal components, there is a general good agreement between GMPEs and observations for PGA and short periods (T = 0.3s) and rock and stiff sites. The observations for soft sites seems to be better described by a linear model (Figure 6.1 and 6.2).

At periods up to 1s and PGV rock and stiff sites are adequately represented by the two models, while for soft soils and short distances the discrepancy between the two models are large. Observations are generally underestimated by Akkar et al (2014) predictions.

At longer periods (T = 3s) both models underpredicts the observations.

The vertical components are well described by Bindi et al (2010) model at short periods (T = 0.04 - 1s), whereas at long periods (T > 1 s) the fit with GMPEs is poor, especially at large distances.

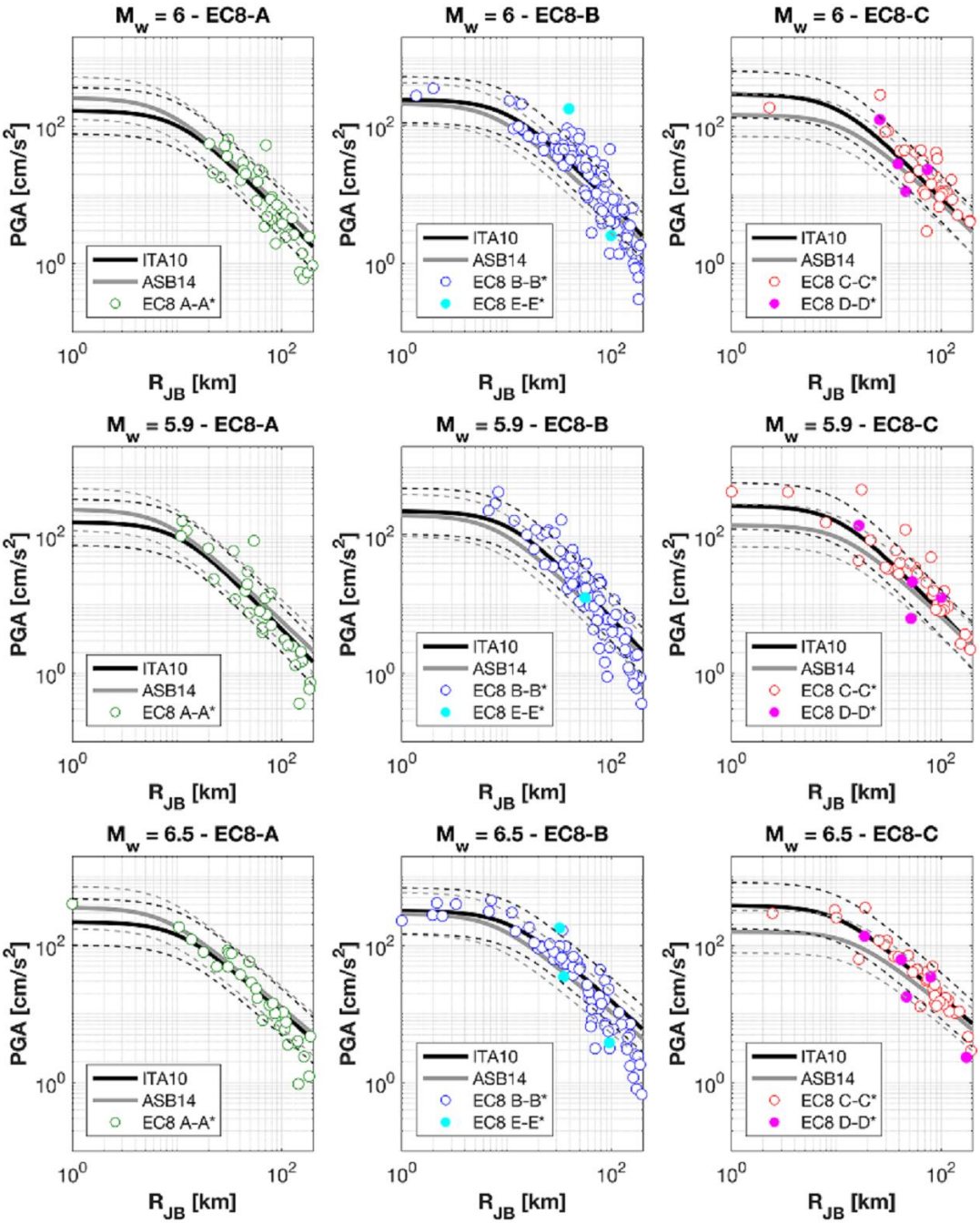

Figure 6.1: Observed horizontal PGA against ITA10 (black curve) and ASB14 (grey line): left EC8 A sites, Middle EC8 B and E sites; right EC8 C and D sites. Top: Amatrice earthquake, Middle: Ussita earthquake, Bottom: Norcia earthquake

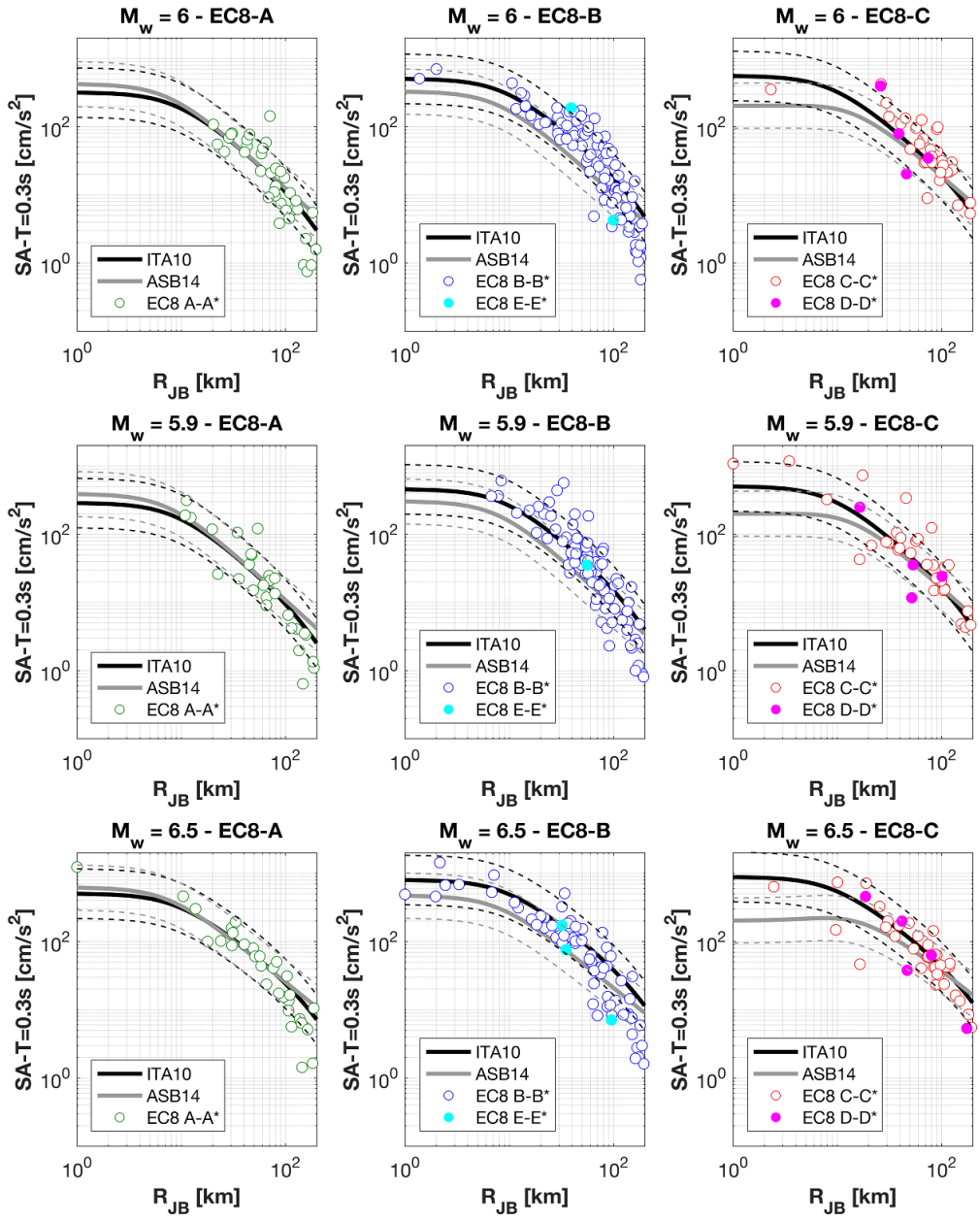

Figure 6.2: Observed horizontal SA (0.3s) against ITA10 (black curve) and ASB14 (grey line): left EC8 A sites, Middle EC8 B and E sites; right EC8 C and D sites. Top: Amatrice earthquake, Middle: Ussita earthquake, Bottom: Norcia earthquake

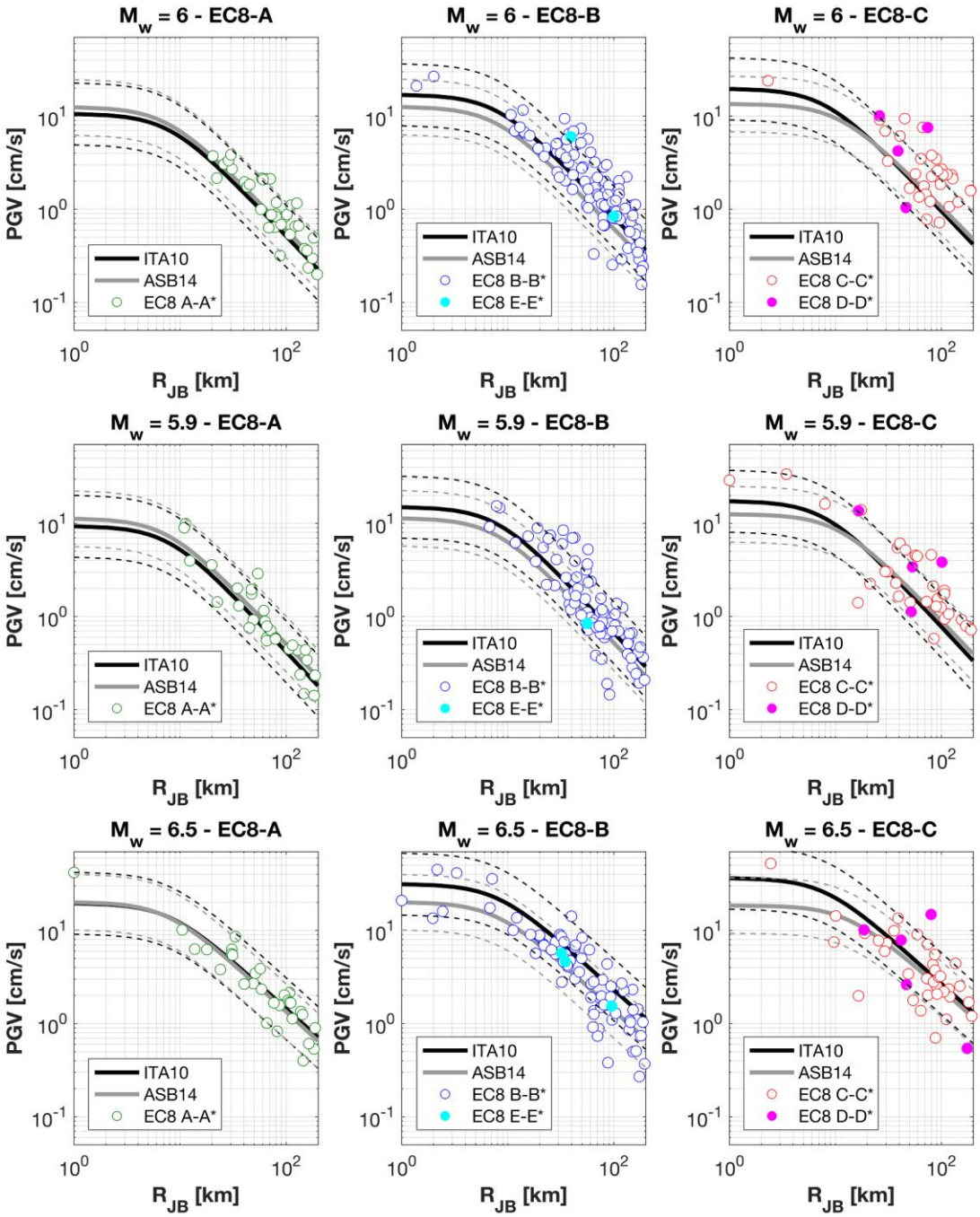

Figure 6.3: Observed horizontal PGV against ITA10 (black curve) and ASB14 (grey line): left EC8 A sites, Middle EC8 B and E sites; right EC8 C and D sites. Top: Amatrice earthquake, Middle: Ussita earthquake, Bottom: Norcia earthquake

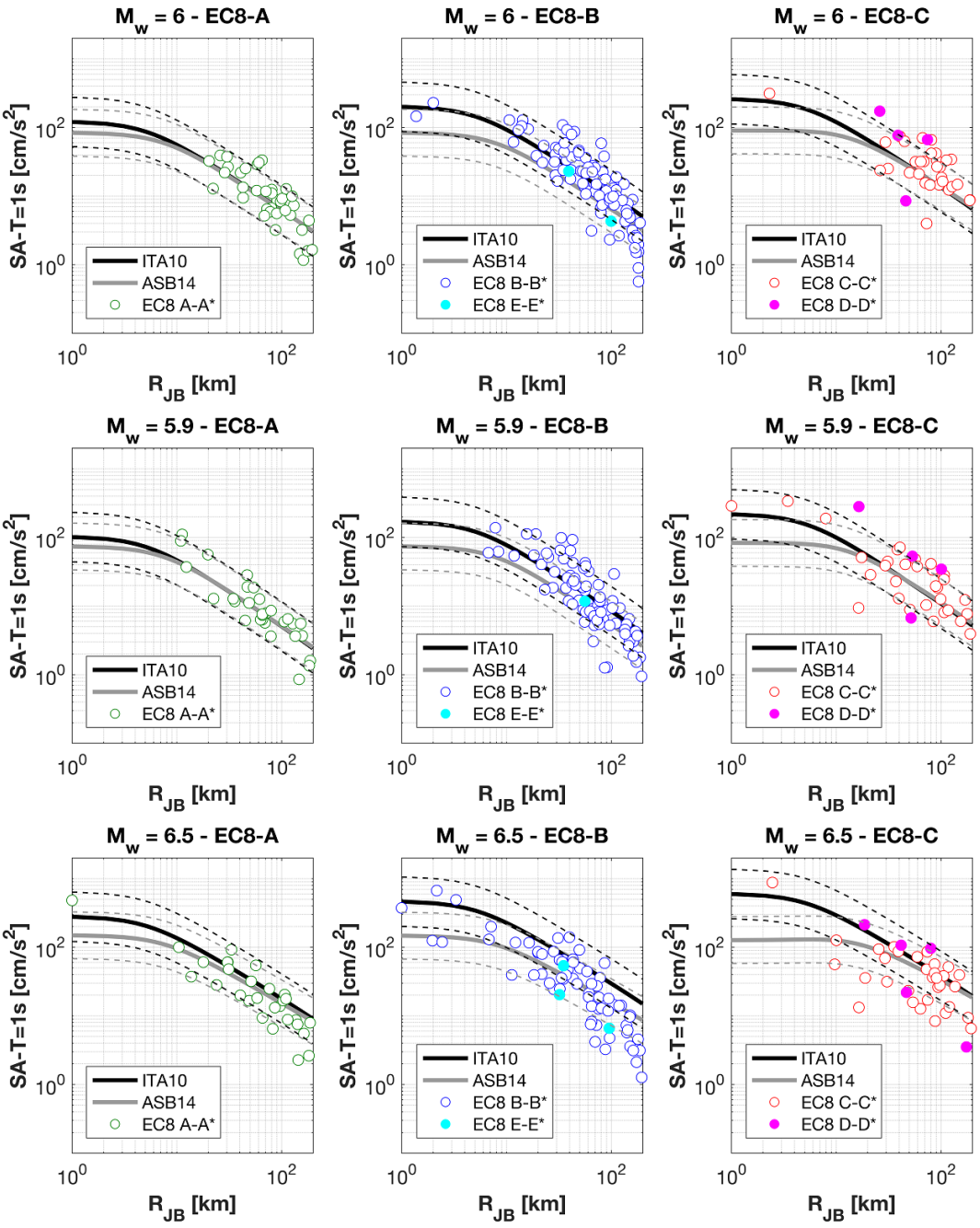

Figure 6.4: Observed horizontal SA (1.0s) against ITA10 (black curve) and ASB14 (grey line): left EC8 A sites, Middle EC8 B and E sites; right EC8 C and D sites. Top: Amatrice earthquake, Middle: Ussita earthquake, Bottom: Norcia earthquake

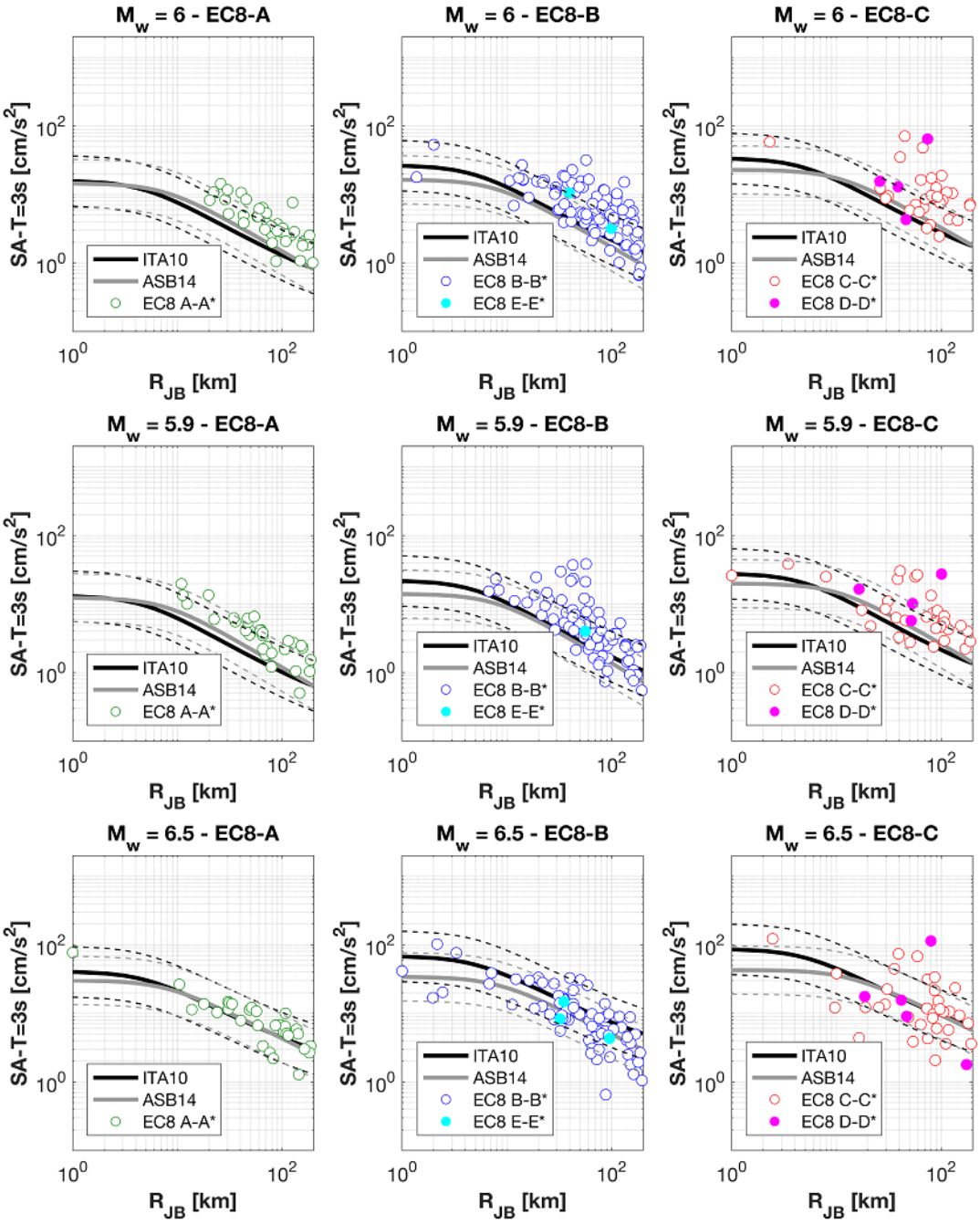

Figure 6.5: Observed horizontal SA (3.0s) against ITA10 (black curve) and ASB14 (grey line): left EC8 A sites, Middle EC8 B and E sites; right EC8 C and D sites. Top: Amatrice earthquake, Middle: Ussita earthquake, Bottom: Norcia earthquake

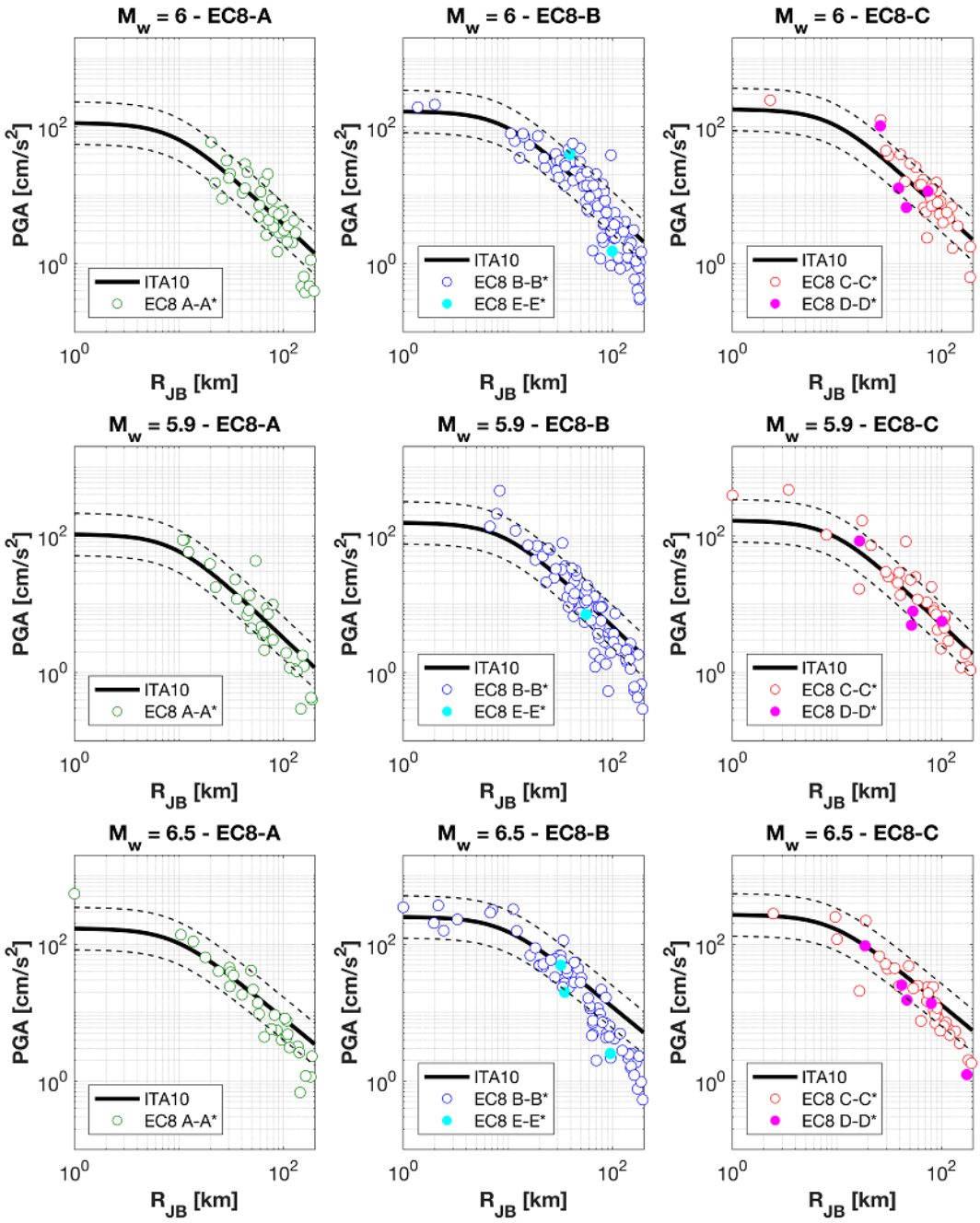

Figure 6.6: Observed vertical PGA against ITA10 (black curve) and ASB14 (grey line): left EC8 A sites, Middle EC8 B and E sites; right EC8 C and D sites. Top: Amatrice earthquake, Middle: Ussita earthquake, Bottom: Norcia earthquake

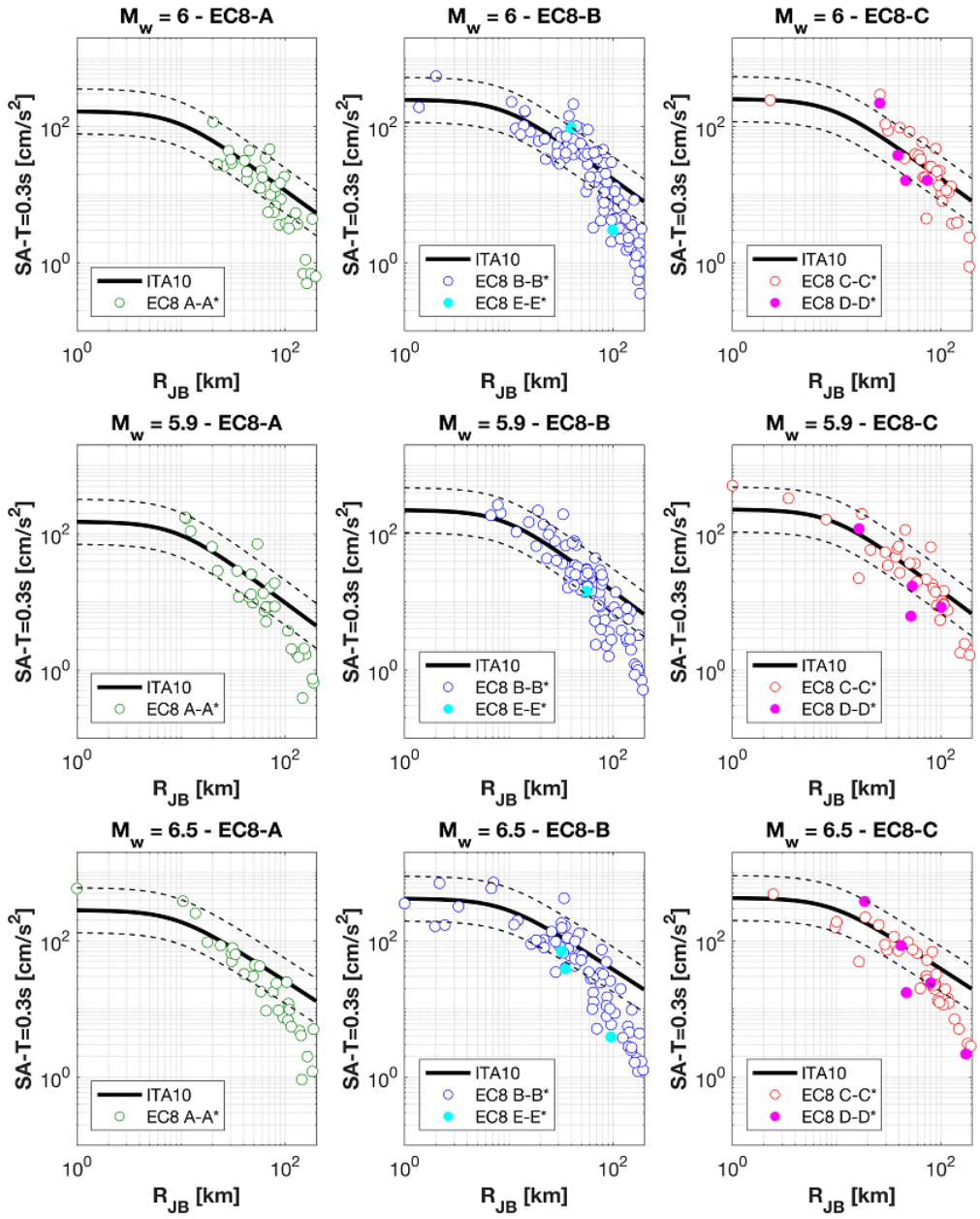

Figure 6.7: Observed vertical SA (0.3s) against ITA10 (black curve) and ASB14 (grey line): left EC8 A sites, Middle EC8 B and E sites; right EC8 C and D sites. Top: Amatrice earthquake, Middle: Ussita earthquake, Bottom: Norcia earthquake.

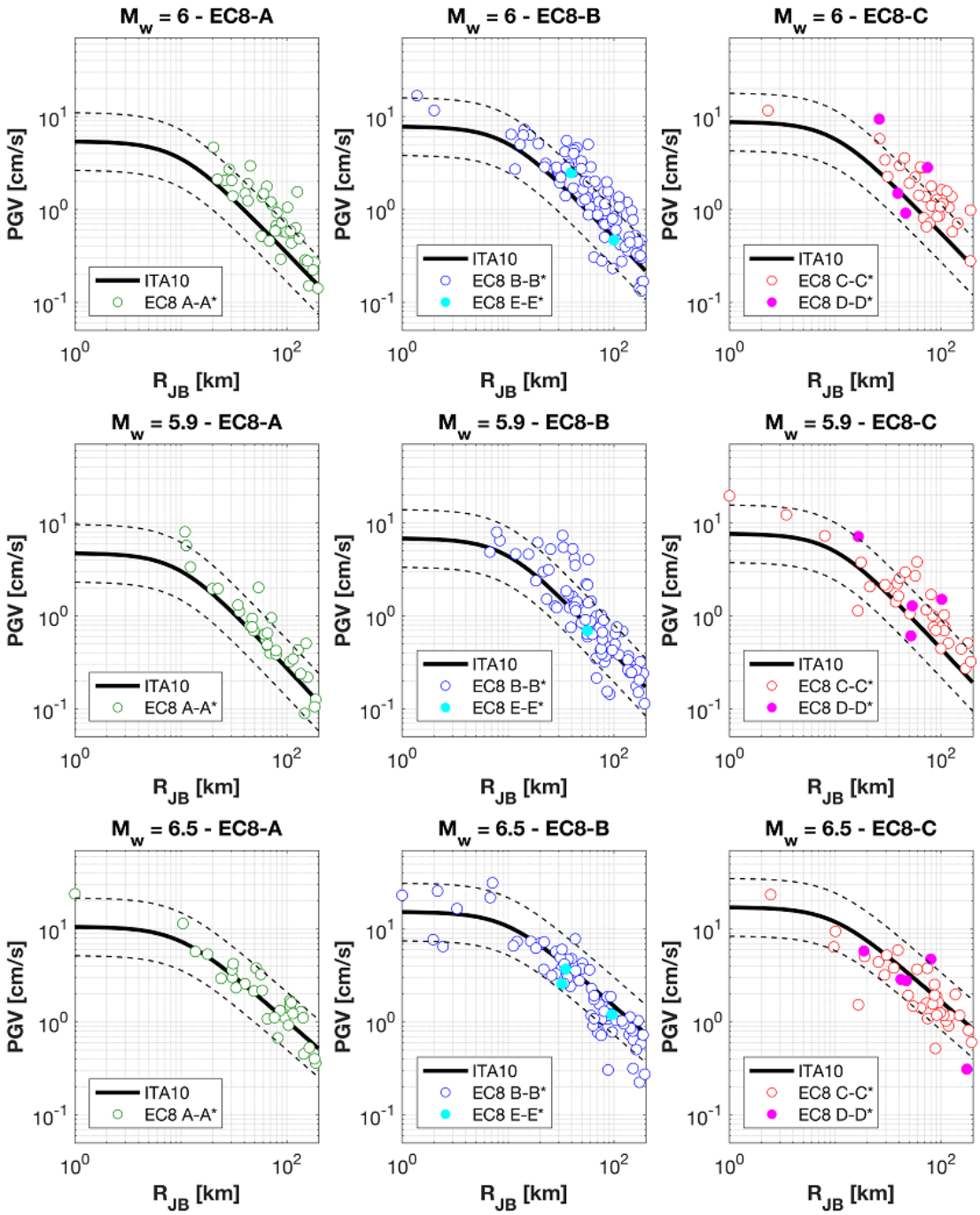

Figure 6.8: Observed vertical PGV against ITA10 (black curve) and ASB14 (grey line): left EC8 A sites, Middle EC8 B and E sites; right EC8 C and D sites. Top: Amatrice earthquake, Middle: Ussita earthquake, Bottom: Norcia earthquake.

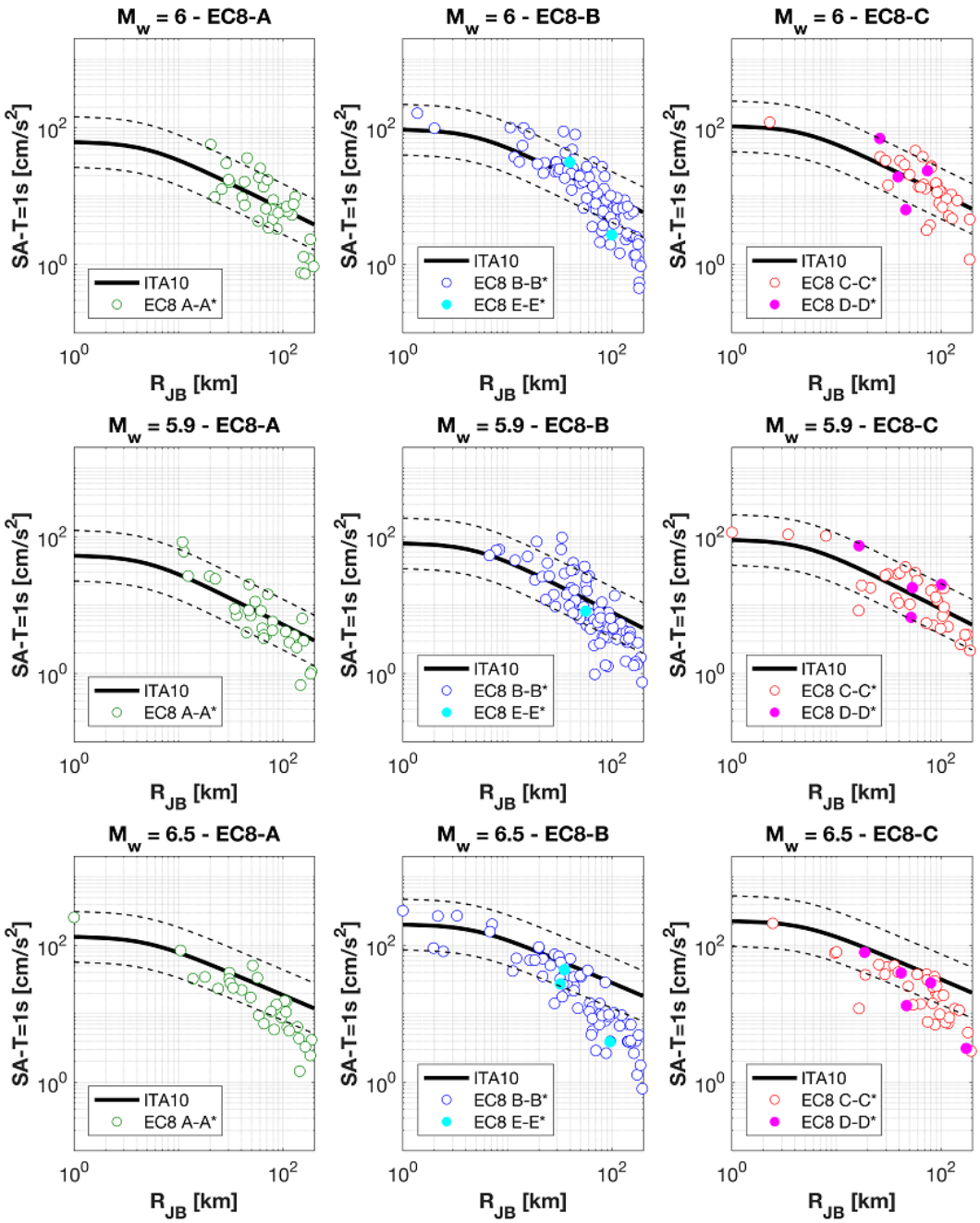

Figure 6.9: Observed vertical SA (1.0s) against ITA10 (black curve) and ASB14 (grey line): left EC8 A sites, Middle EC8 B and E sites; right EC8 C and D sites. Top: Amatrice earthquake, Middle: Ussita earthquake, Bottom: Norcia earthquake

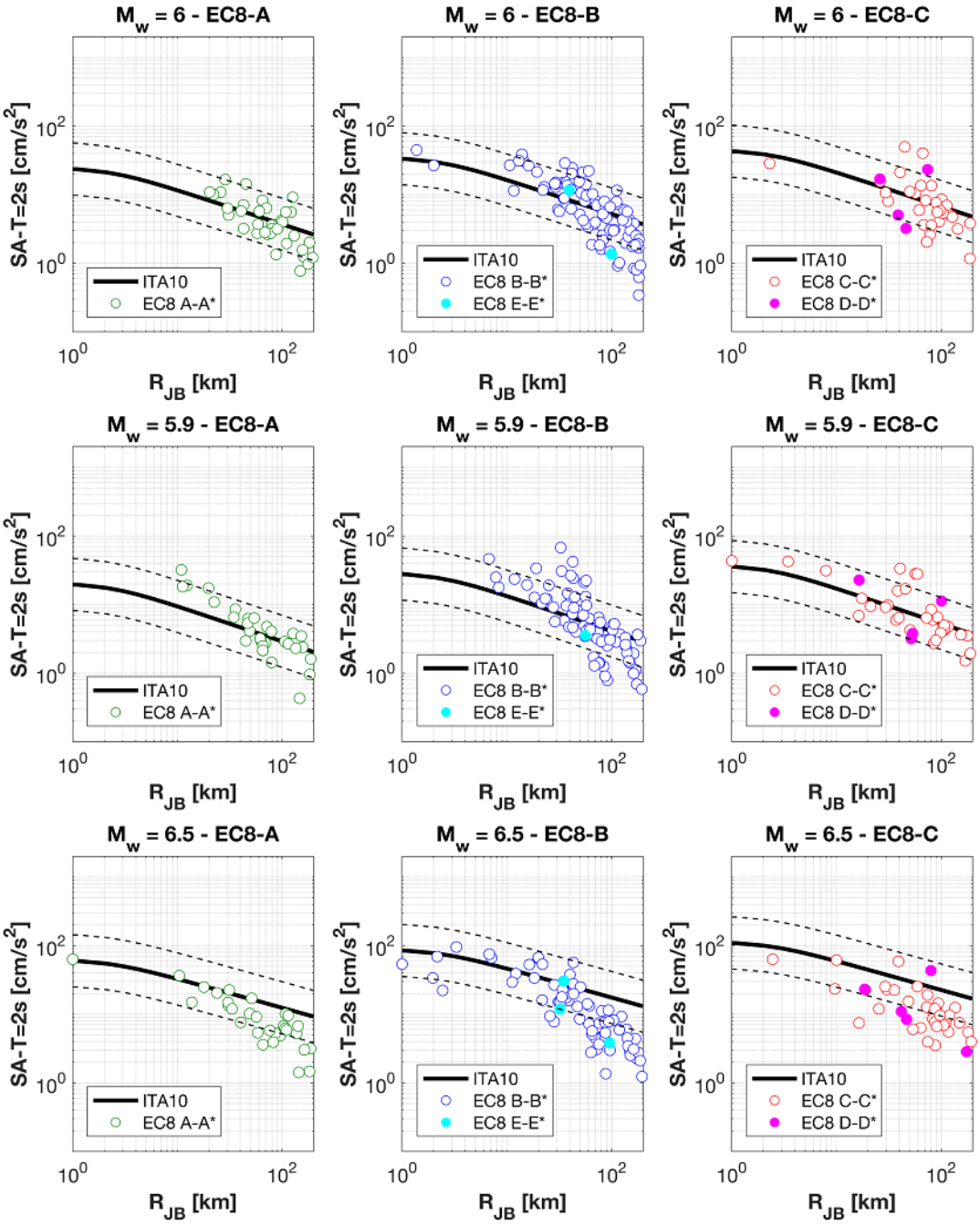

Figure 6.10: Observed vertical SA (2.0s) against ITA10 (black curve) and ASB14 (grey line): left EC8 A sites, Middle EC8 B and E sites; right EC8 C and D sites. Top: Amatrice earthquake, Middle: Ussita earthquake, Bottom: Norcia earthquake

6.1 Residual analysis

In order to estimate the overall performance of the GMPEs against the recording data, the residuals, calculated as the natural logarithm of the difference between observations and predictions by Bindi et al (2010), have been plotted in function of distance, for the geometric mean of the horizontal components (Figures 6.11- 6.12).

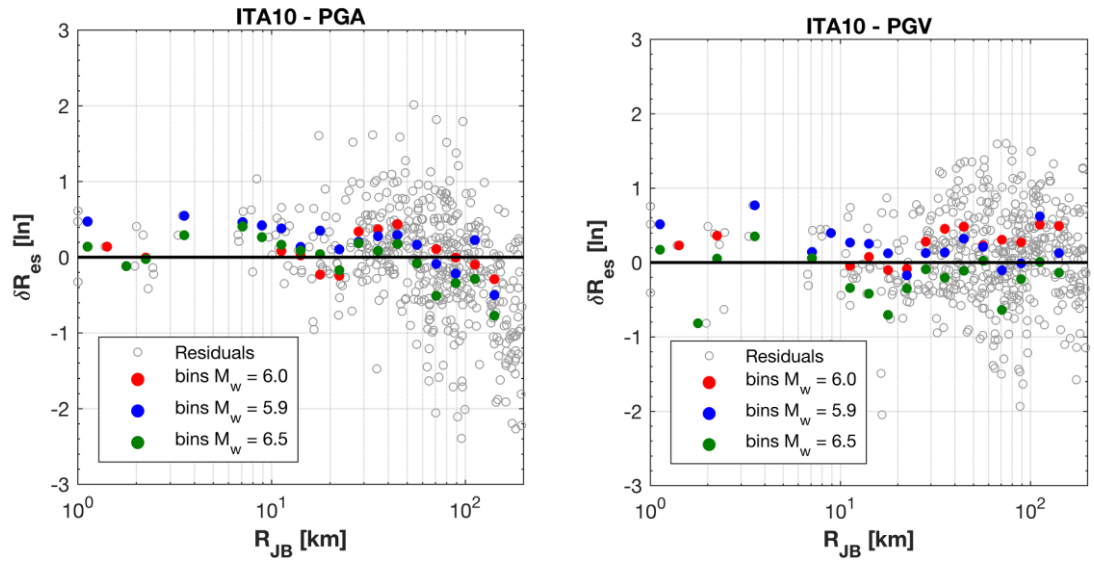

Figure 6.11. Residuals of the three main events plotted against Joyner-Boore distance, for geometric mean of horizontal components: PGA (left) and PGV (right)

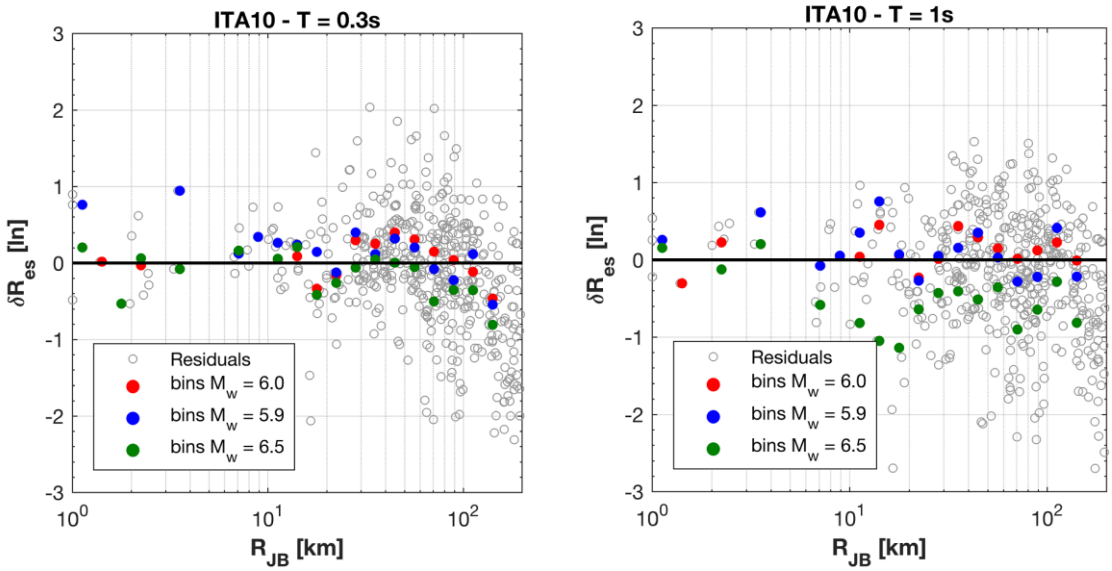

Figure 6.12. Residuals of the three main events plotted against Joyner-Boore distance, for geometric mean of horizontal components: SA (0.3s) (left) and SA(1.0) (right).

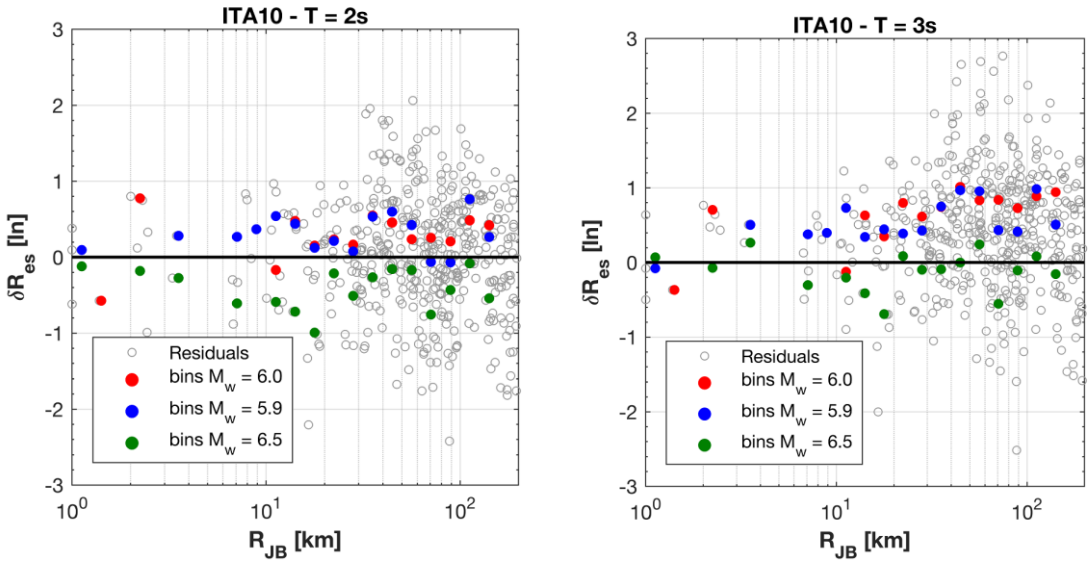

Figure 6.13. Residuals of the three main events plotted against Joyner-Boore distance, for geometric mean of SA (2.0s) (left) and SA(3.0) (right) horizontal components.

The between event term, defined as the average of the residuals for each event, has been plotted in Figure 6.14. The event term measures the overall misfit of recordings with respect to an attenuation model. In particular we observe that the ground motion level generated by the Mw 6.5 event is, on average, lower than the predictions by the Bindi et al (2010).

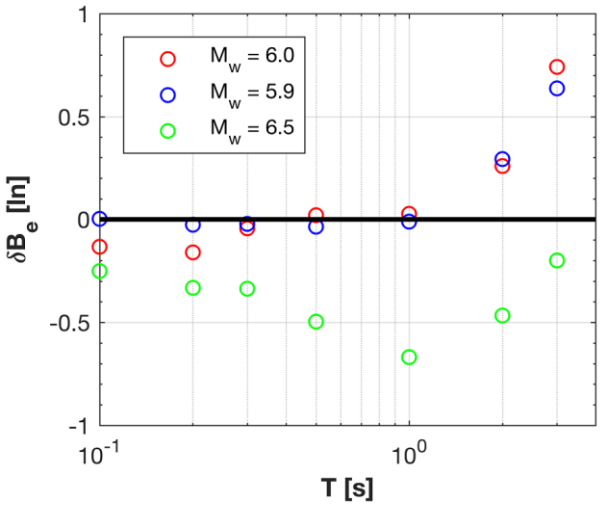

Figure 6.14. Between-event term of the three main events plotted against period, for geometric mean of horizontal components.

7. Elastic and Inelastic Response Spectra from 24/08/2016 event

In this section, elastic and inelastic response spectra of the ground motions during the first event (M6.0 24/08/2016) are provided. With regard to elastic response the pseudo-spectral acceleration (PSA), pseudo-spectral velocity (PSV) and spectral displacement (SD) are reported for all the available records for three different values of damping ratio, (z), that is 2%, 5% and 10%. Additionally, constant-strength inelastic displacement ratios C_R are provided for the horizontal components of ground motion. C_R is defined as the ratio of maximum inelastic displacement response to maximum elastic displacement of the corresponding linear infinitely elastic system, Eq. .

$$C_R = \frac{\delta_{inelastic}^{\max}}{SD(T)}$$

These spectra were calculated for 5% damped, elastic-perfectly plastic oscillators and are reported at three values of reduction factor R=2,4,6, where R is defined as the ratio of elastic response spectral acceleration to yield spectral acceleration, Eq. .

$$R = \frac{PSA(T)}{PSA_{yield}(T)}$$

The relevant plots are provided below in sequence of increasing epicentral distance (first horizontal then vertical components) and do not follow the rest of the report's figure enumeration.

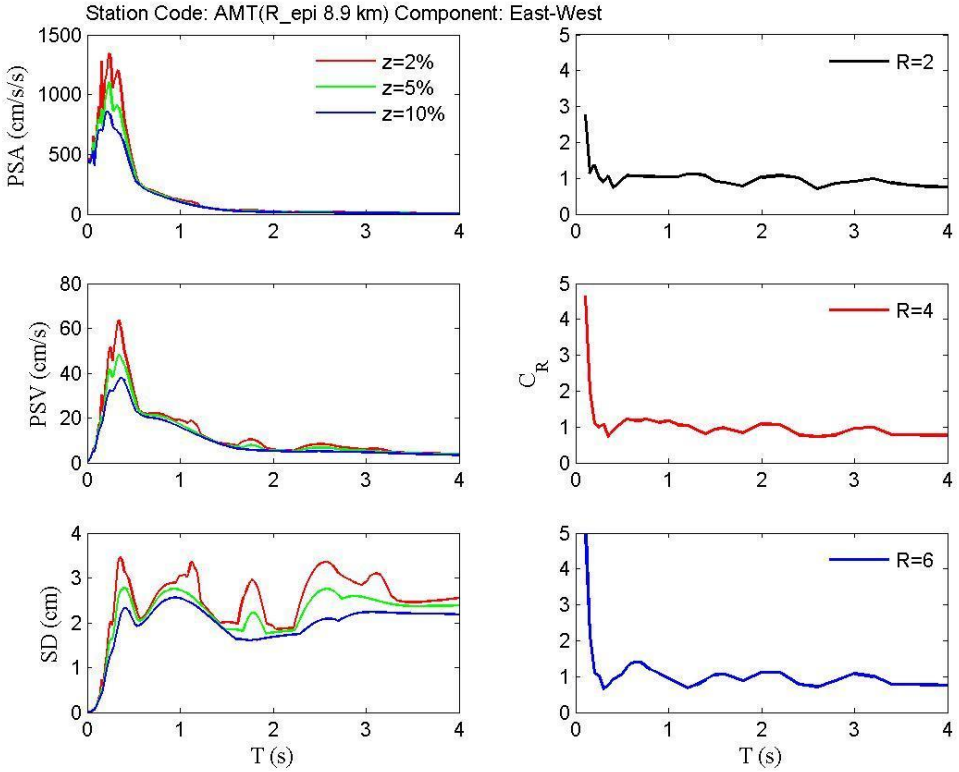

Figure 7.1. AMT station, East-West component: pseudo-acceleration (PSA), pseudo-velocity (PSV) and displacement (SD) elastic response spectra for different damping values (left); inelastic displacement ratios for different reduction factors (right).

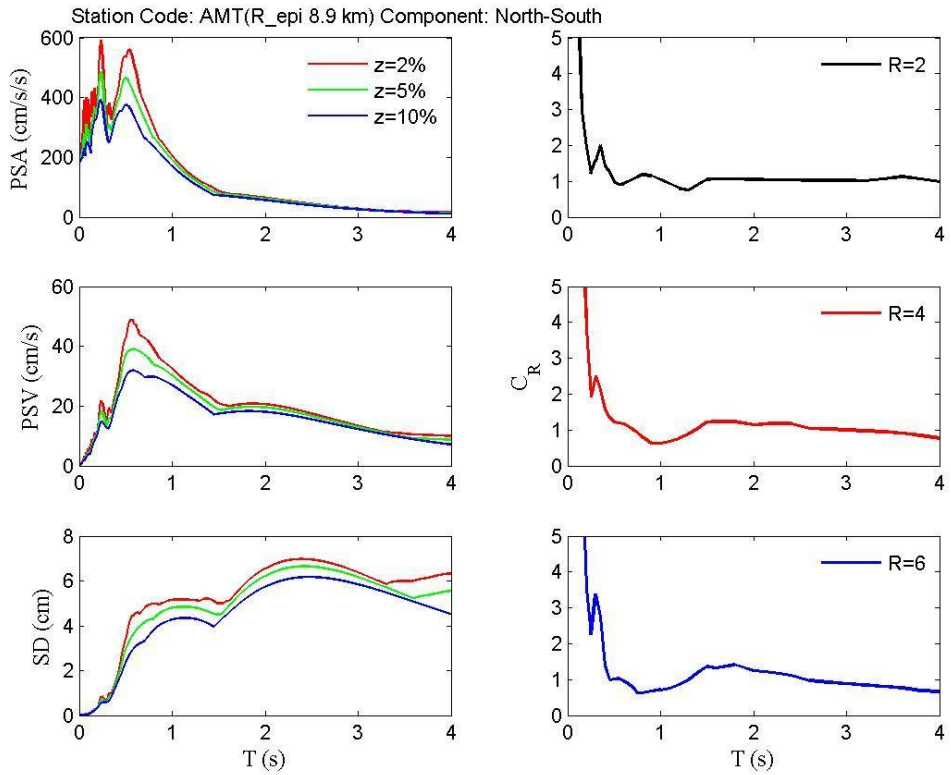

Figure 7.2. AMT station, North-South component: pseudo-acceleration (PSA), pseudo-velocity (PSV) and displacement (SD) elastic response spectra for different damping values (left); inelastic displacement ratios for different reduction factors (right).

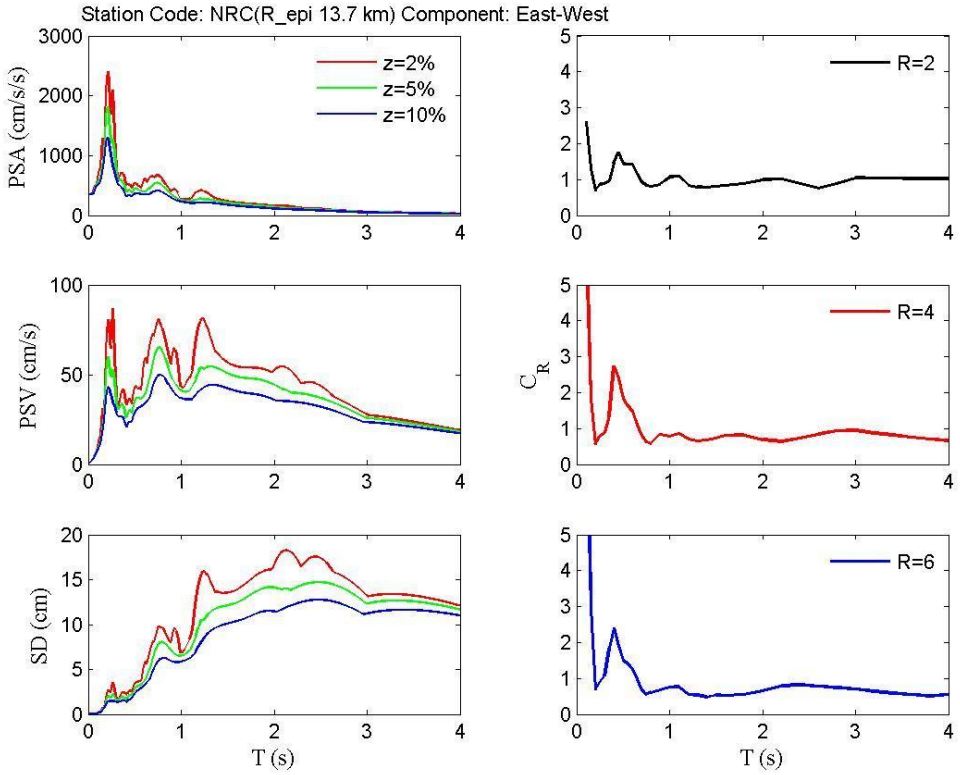

Figure 7.3. NRC station,East-West component: pseudo-acceleration (PSA), pseudo-velocity (PSV) and displacement (SD) elastic response spectra for different damping values (left); inelastic displacement ratios for different reduction factors (right).

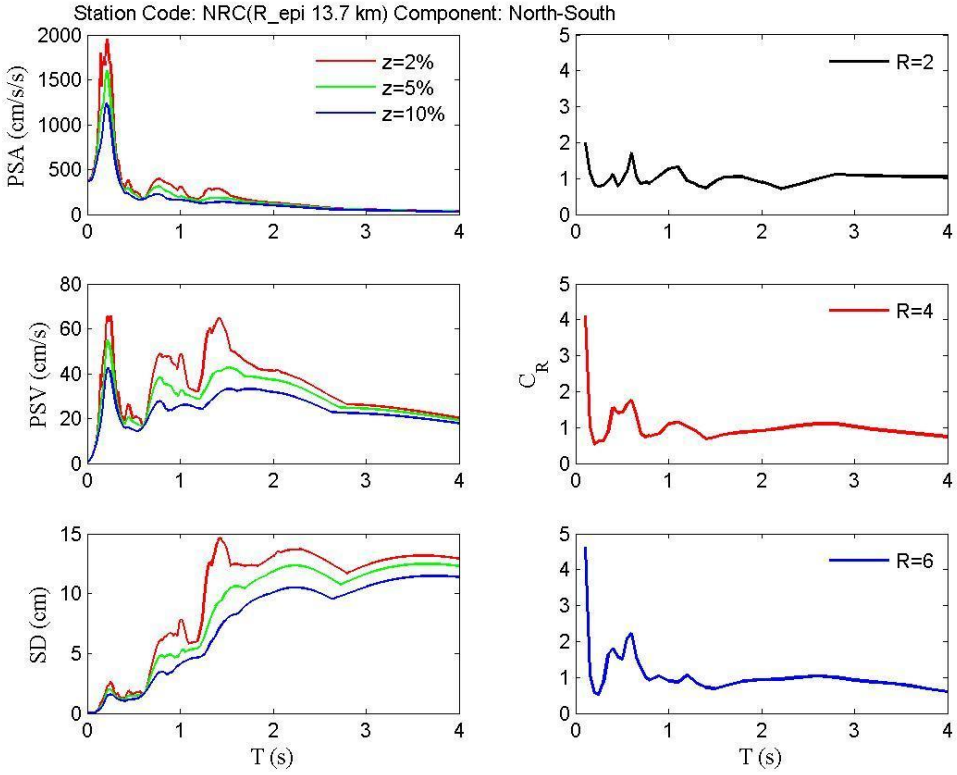

Figure 7.4. NRC station, North-South component: pseudo-acceleration (PSA), pseudo-velocity (PSV) and displacement (SD) elastic response spectra for different damping values (left); inelastic displacement ratios for different reduction factors (right).

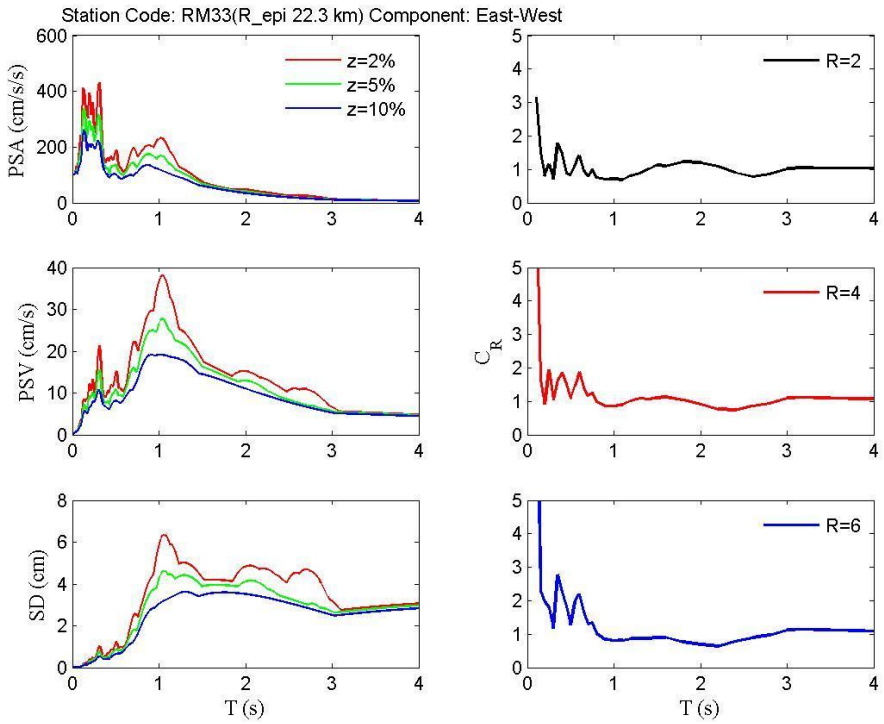

Figure 7.5. RM33 station, East-West component: pseudo-acceleration (PSA), pseudo-velocity (PSV) and displacement (SD) elastic response spectra for different damping values (left); inelastic displacement ratios for different reduction factors (right).

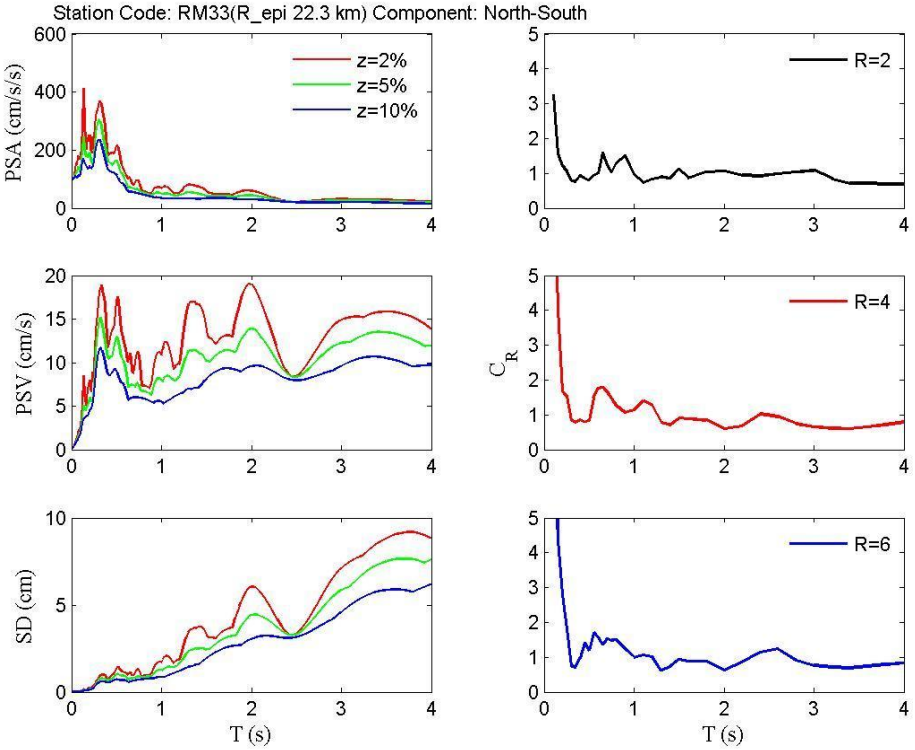

Figure 7.6. RM33 station, North-South component: pseudo-acceleration (PSA), pseudo-velocity (PSV) and displacement (SD) elastic response spectra for different damping values (left); inelastic displacement ratios for different reduction factors (right).

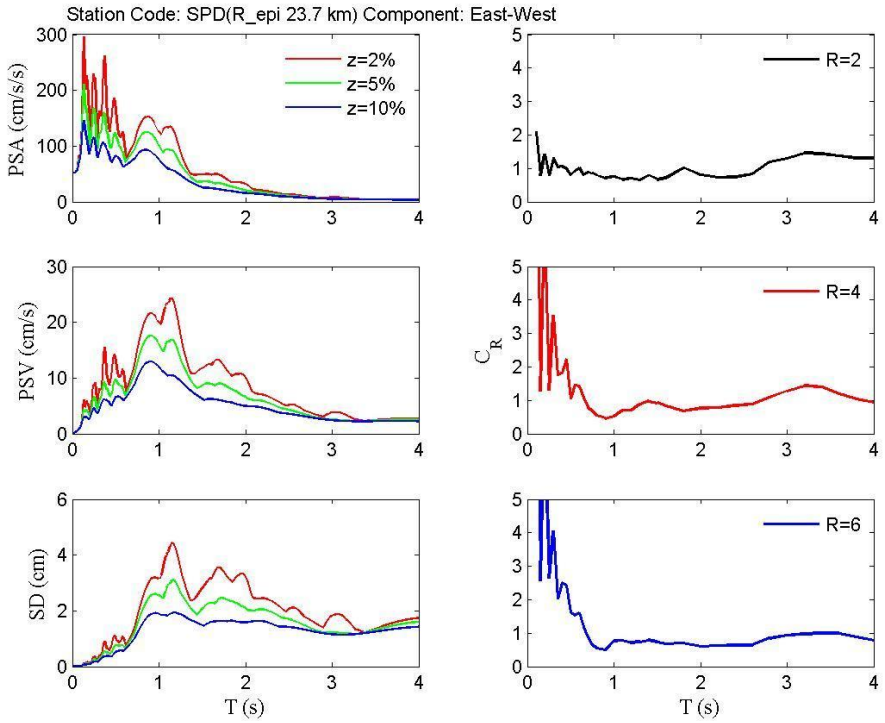

Figure 7.7. RM33 station, East-West component: pseudo-acceleration (PSA), pseudo-velocity (PSV) and displacement (SD) elastic response spectra for different damping values (left); inelastic displacement ratios for different reduction factors (right).

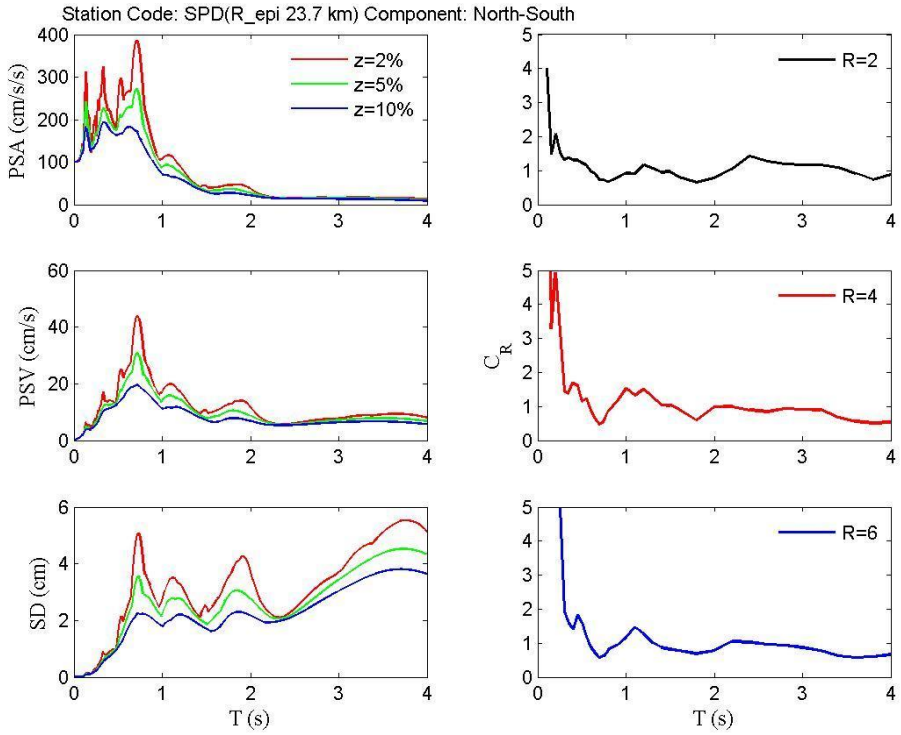

Figure 7.8. RM33 station, North-South component: pseudo-acceleration (PSA), pseudo-velocity (PSV) and displacement (SD) elastic response spectra for different damping values (left); inelastic displacement ratios for different reduction factors (right).

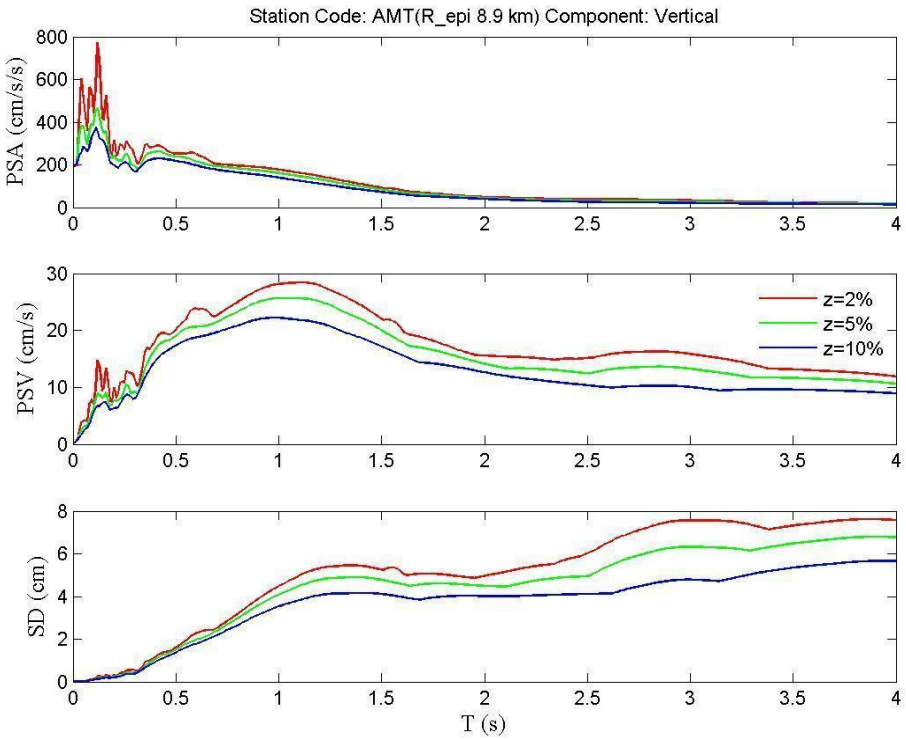

Figure 7.9. AMT station, vertical component: pseudo-acceleration (PSA), pseudo-velocity (PSV) and displacement (SD) elastic response spectra for different damping values.

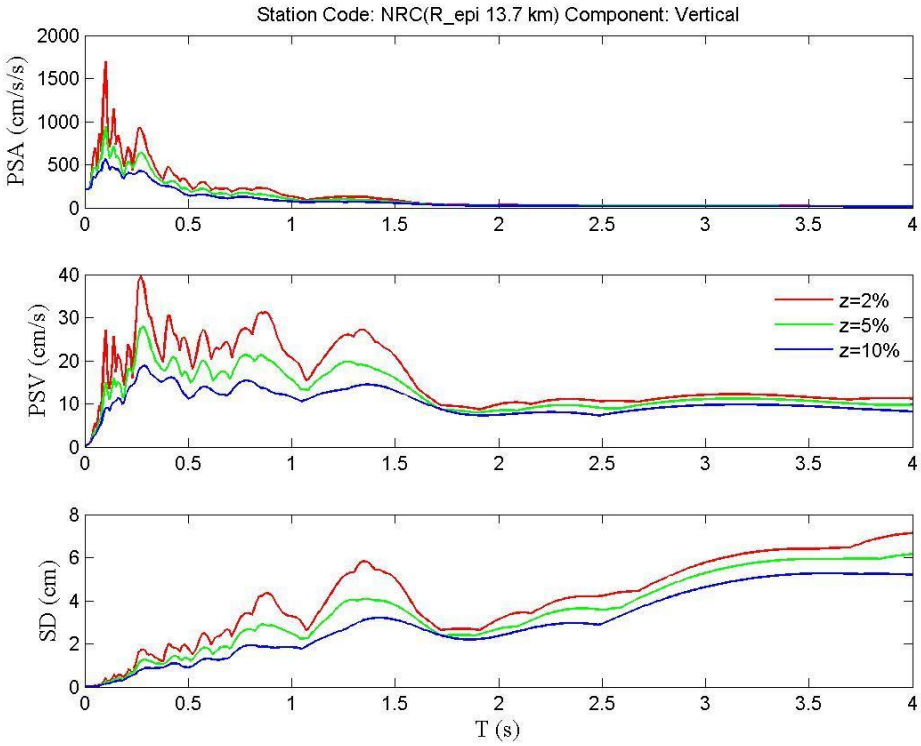

Figure 7.10. NRC station, vertical component: pseudo-acceleration (PSA), pseudo-velocity (PSV) and displacement (SD) elastic response spectra for different damping values.

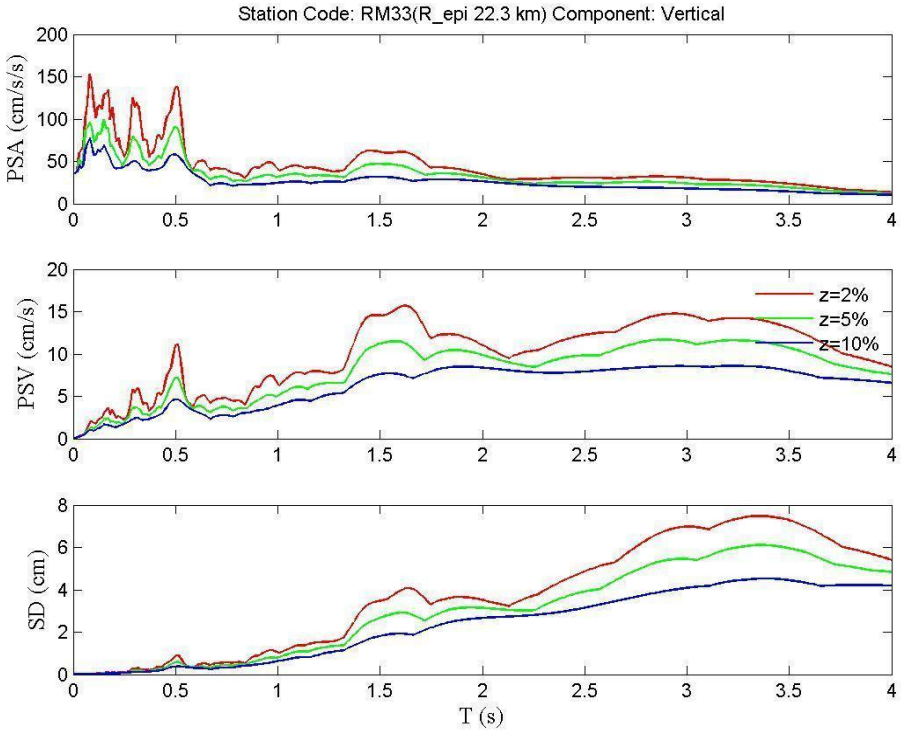

Figure 7.11. RM33 station, vertical component: pseudo-acceleration (PSA), pseudo-velocity (PSV) and displacement (SD) elastic response spectra for different damping values.

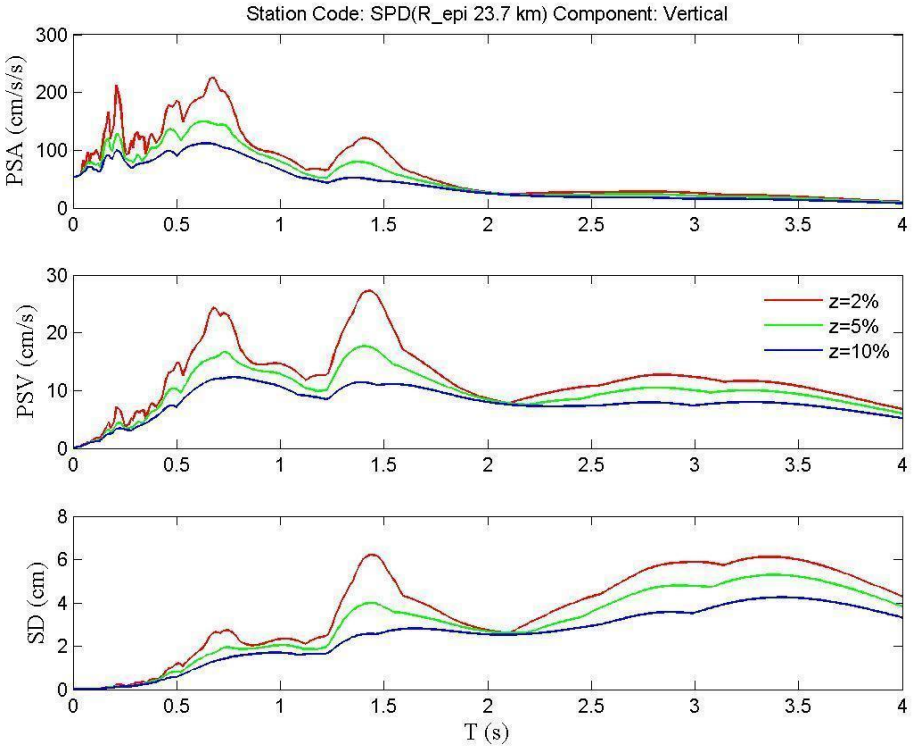

Figure 7.12. SPD station, vertical component: pseudo-acceleration (PSA), pseudo-velocity (PSV) and displacement (SD) elastic response spectra for different damping values.

8. Elastic response spectra for different events recorded at the same sites

Among the available data, accelerometric stations that (i) recorded all the four events and (ii) observed a maximum PGA higher than 0.3g in at least one event have been selected. These stations are AMT, NOR and NRC. The corresponding elastic response spectra are here reported for comparison.

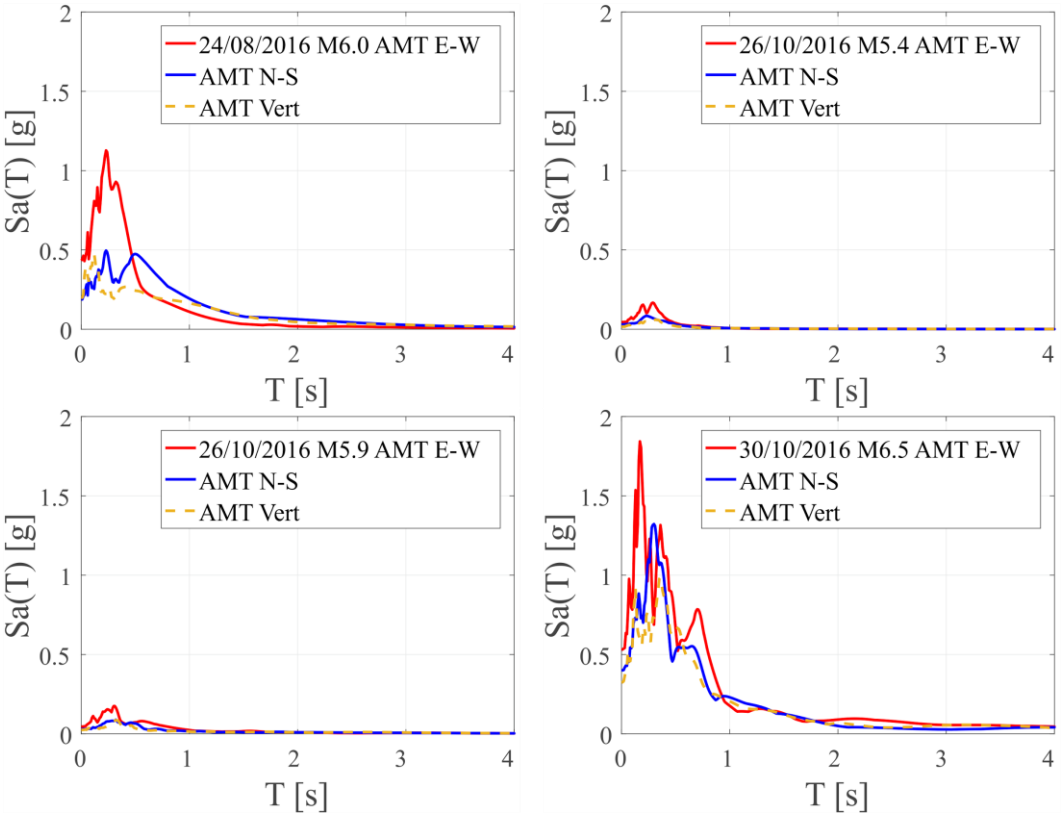

Figure 8.1. Pseudo-acceleration elastic response spectra recorded by the AMT station.

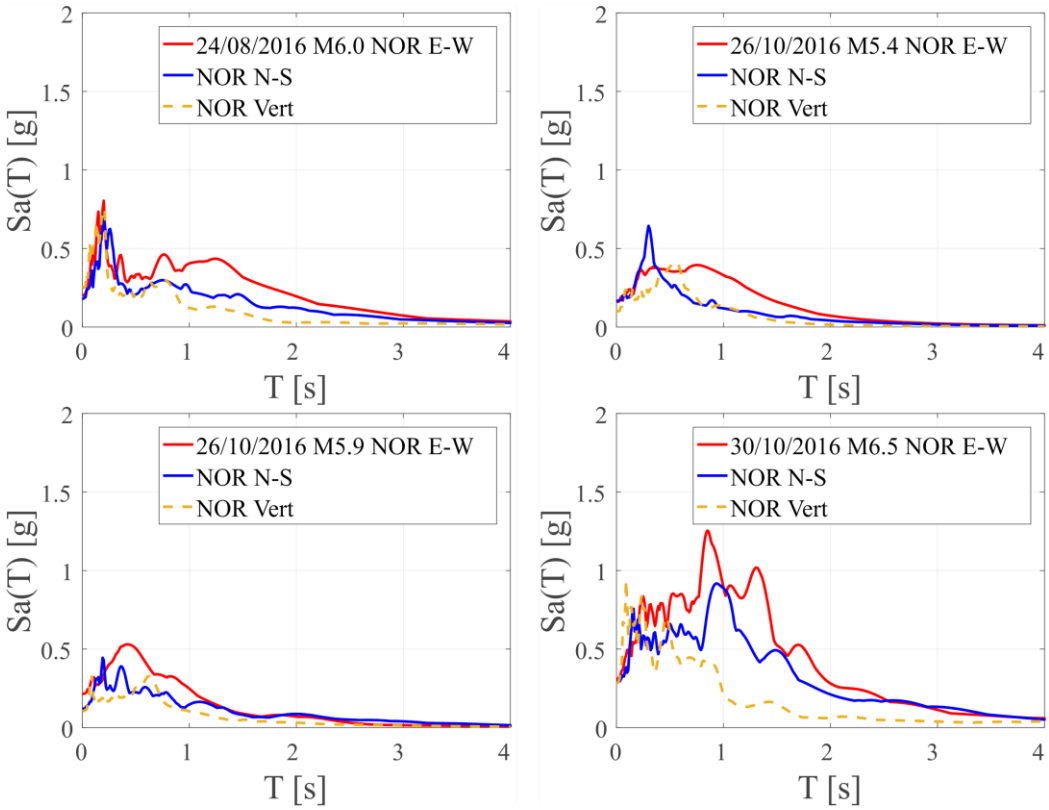

Figure 8.2. Pseudo-acceleration elastic response spectra recorded by the NOR station

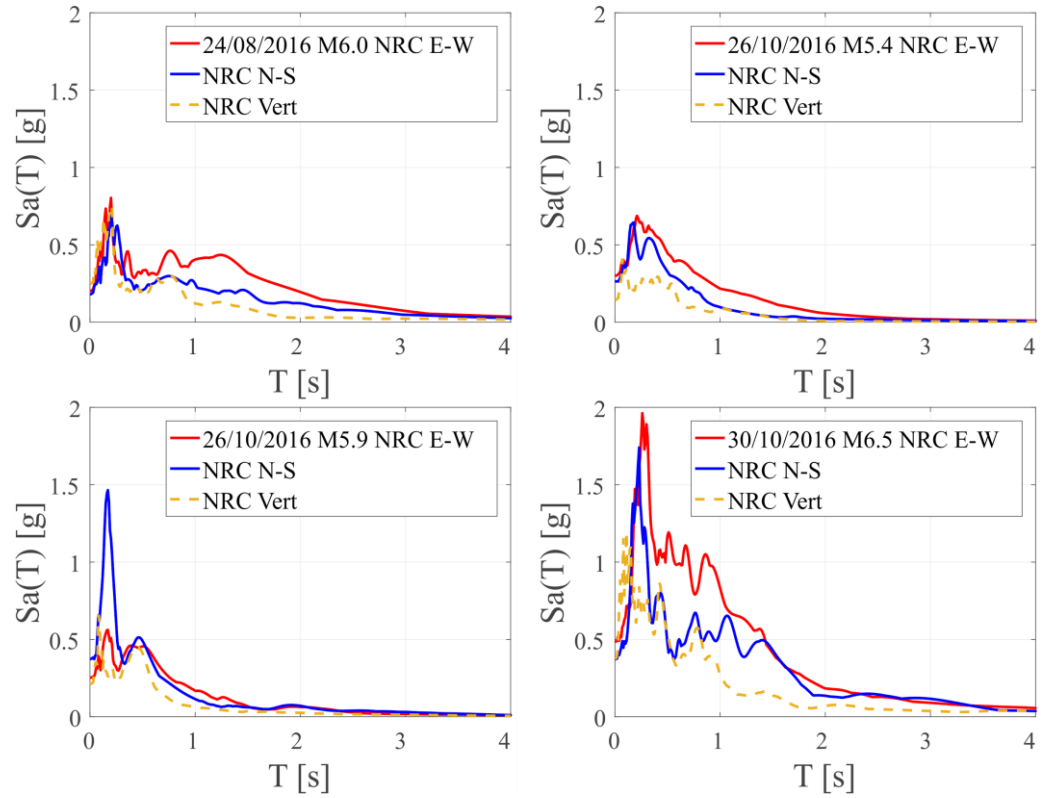

Figure 8.3. Pseudo-acceleration elastic response spectra recorded by the NRC station

A M6.0 event occurred in the 1997 (the 26th of September) in the same geographic area. The event was recorded by twenty stations: NCR and CLF were among them. Data from these stations are available for three of

the four earthquake analysed in this report: 24/08/2016 M6.0, 26/10/2016 M5.4 and 30/10/2016 M6.5. Recorded signals are reported in the following figures for comparison.

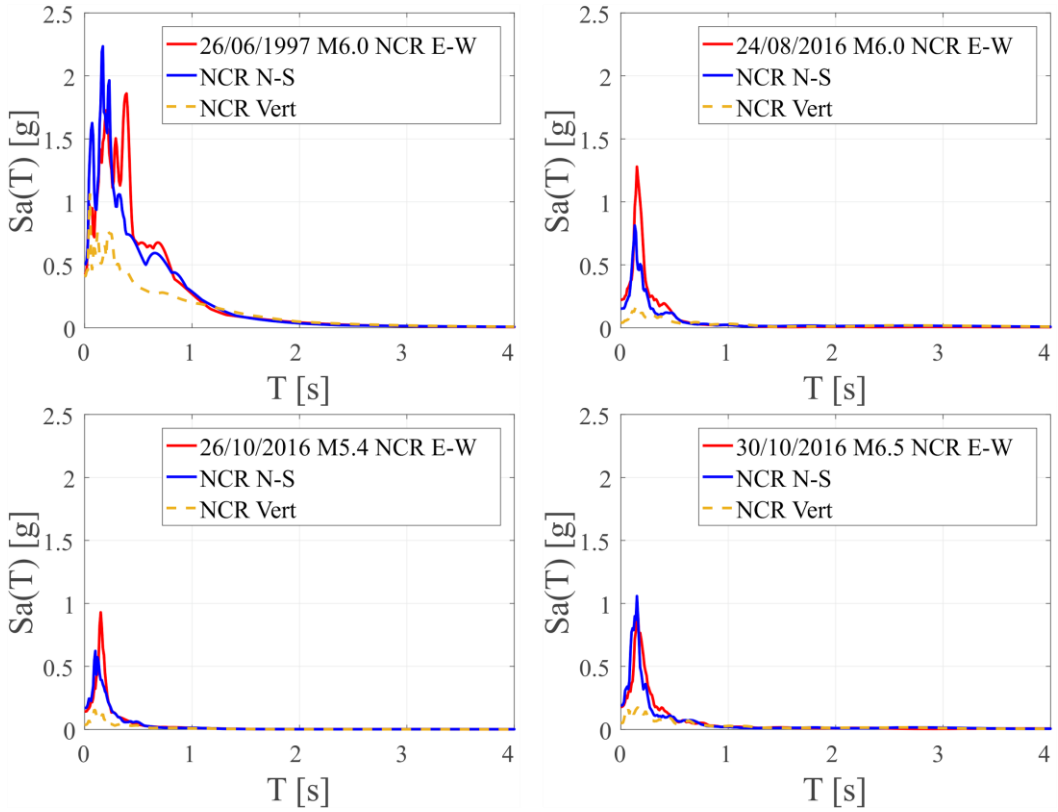

Figure 8.4. Pseudo-acceleration elastic response spectra recorded by the NCR station

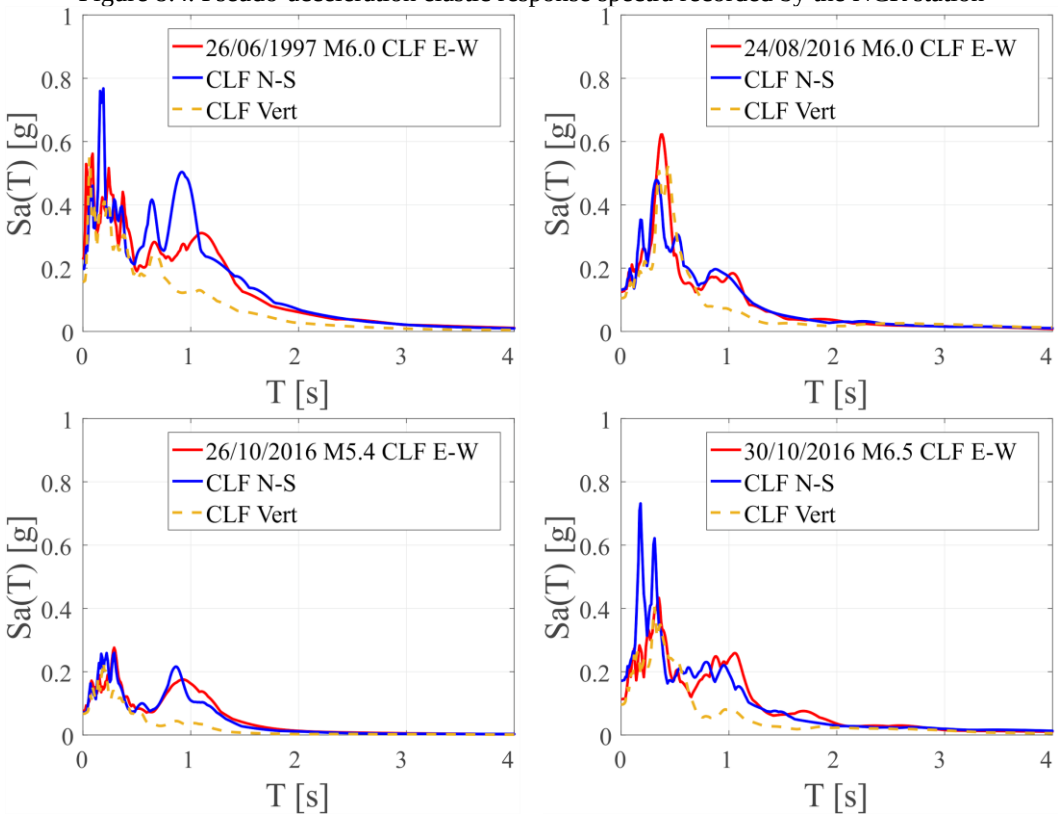

Figure 8.5. Pseudo-acceleration elastic response spectra recorded by the CLF station

The map of the accelerometric stations considered in this section is reported below together with the epicenter of the four recent events and the one of the 1997 event.

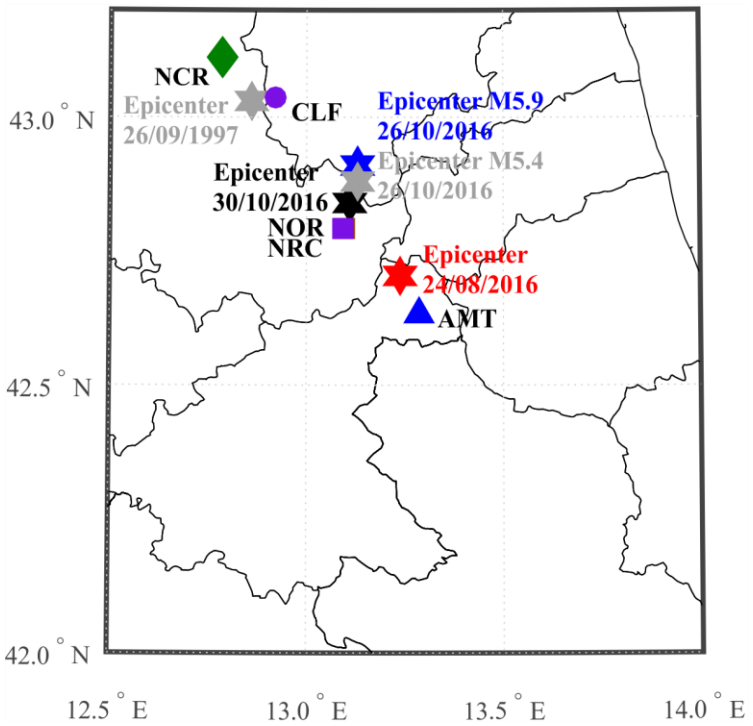

Figure 8.6. Map of the accelerometric station and epicenter locations considered in this section.

9. The Italian seismic code and recorded spectra

The pseudo-acceleration response spectra associated to the horizontal ground motions recorded during the 24/08/2016 event by the four stations with lowest epicentral distance (AMT, NRC, RM33 and SPD) are compared with the elastic spectra provided by the Italian seismic code (NTC2008) at the corresponding sites for soil class provided in Appedix 1 and four different return periods (T_R): 50, 475, 975 and 2475 years. Note that comparison of individual earthquake recordings with probabilistic hazard is a delicate issue and no direct conclusions can be drawn to validate hazard (see Iervolino, 2013).

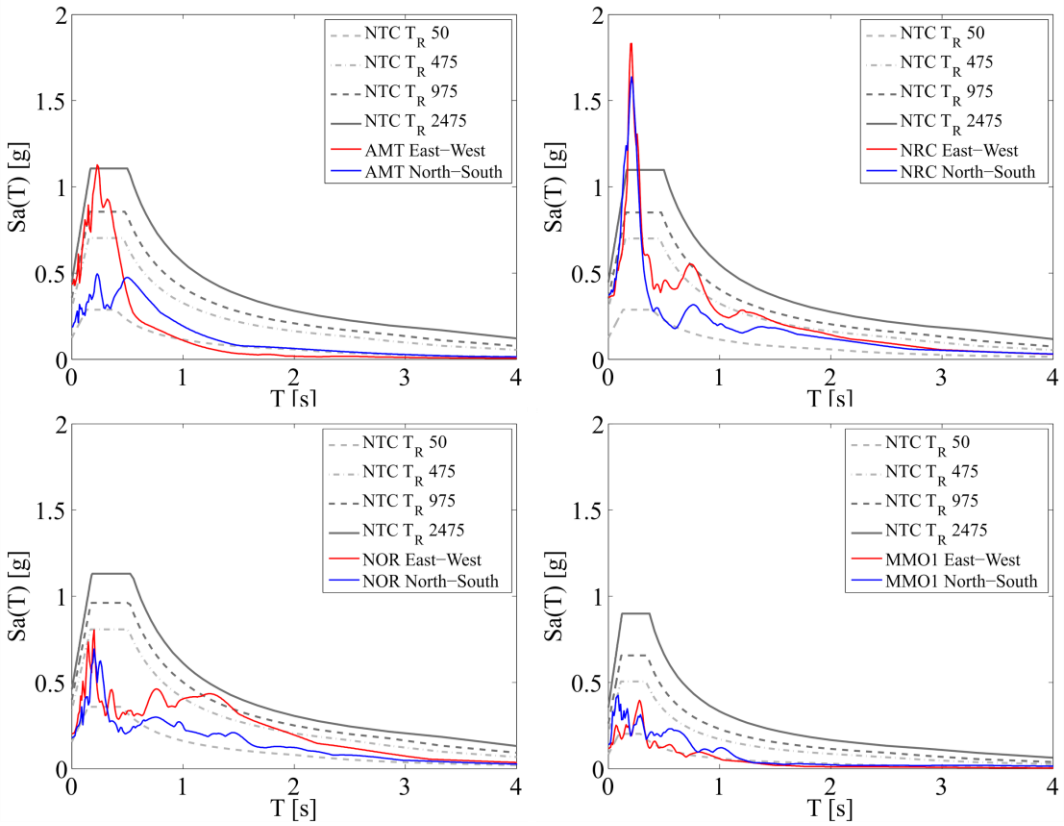

Figure 9.1. Comparison of four epicentral stations' response spectra (horizontal components) with respect to the Italian code elastic response spectra at various return periods.

Referring to the geographical coordinates of the epicentre (42.70N; 13.24E), the hazard disaggregation (Iervolino et al., 2011) was computed for the PGA and for the pseudo-spectral acceleration at 1s vibration period, PSA(T=1s), for two T_R (475 and 2475 years) by means of REXEL v 3.5 (Iervolino et al., 2010), as shown in the following figures.

The disaggregations have a single modal value for both considered return periods. In the case of PGA and T_R=475 years, modal magnitude and distance are around 5.8 and 10 km, respectively. Increasing the return period to 2475 years, magnitude modal value increases to about 6.8 while the corresponding value of distance remains centred on 10 km. Similarly, for PSA(T=1s) and T_R=475 years, modal magnitude and distance are about 6.3 and 10 km, respectively. For T_R=2475 years, the magnitude of the mode increases to 6.8 while the distance remains equal to about 10 km. It is worth noting that, for a given return period, disaggregation of PSA(T=1s) shows a non-negligible contribution of higher distances with respect to the case of the disaggregation of PGA. This is an expected result, see Iervolino et al. (2011), and is more evident for lower return periods. It may be concluded that, according to the hazard assessment of the area, exceedance of high-frequencies spectral accelerations corresponding to 475yr and 2475yr is most likely caused by a close moderate-magnitude earthquake, which is, in fact, compatible to what was observed.

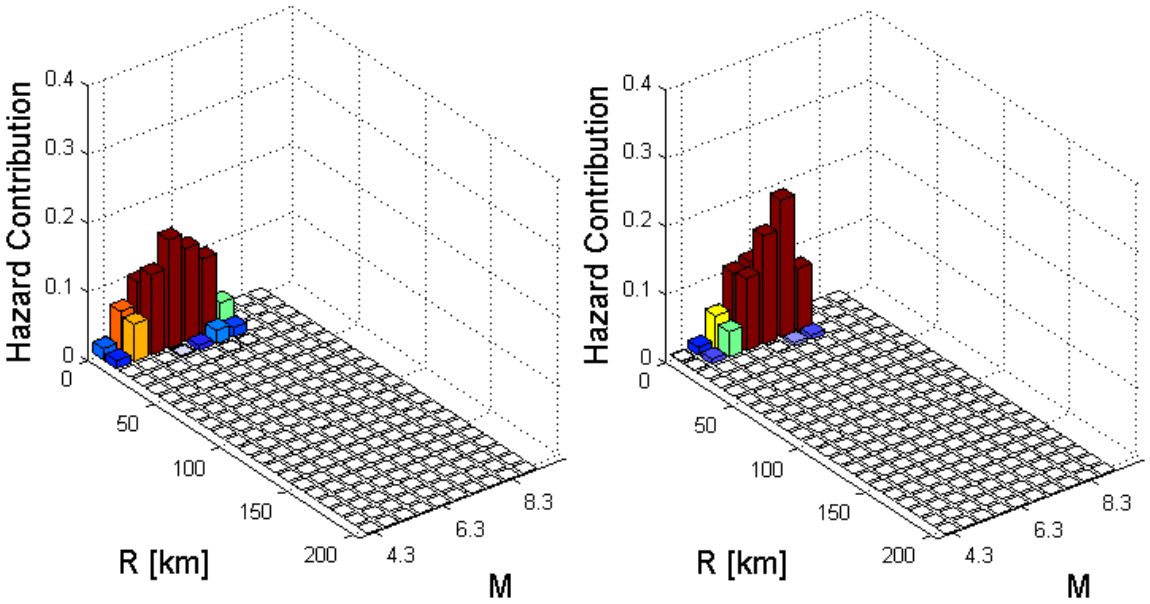

Figure 9.2. Disaggregation of PGA: T_R=475 years (sx) and 2475 years (dx)

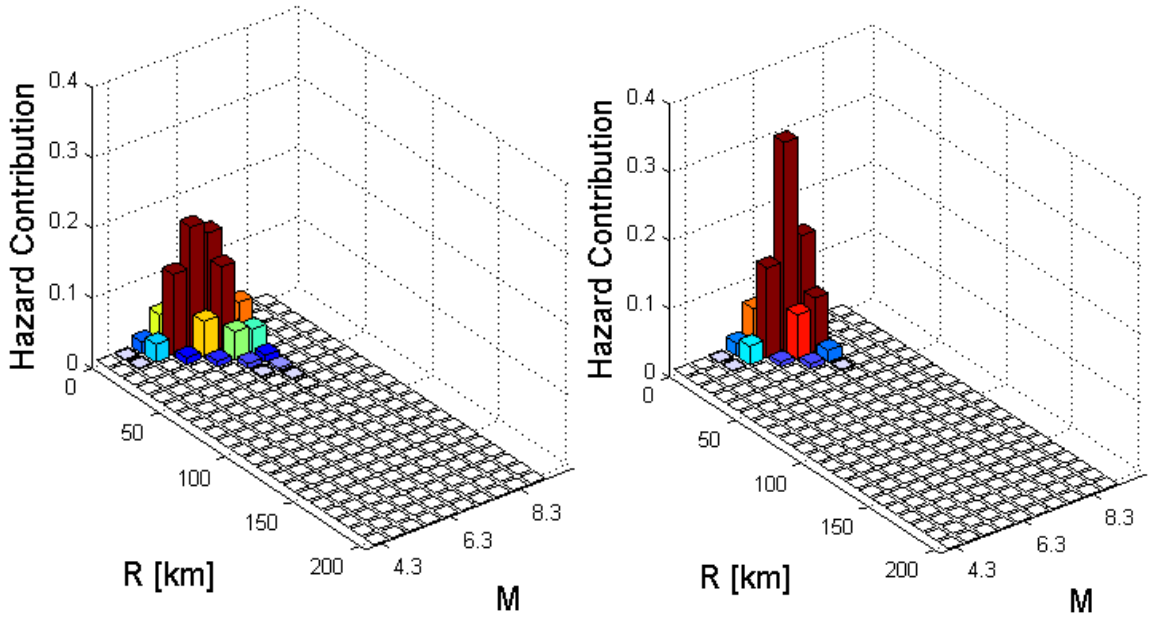

Figure 9.3. Disaggregation of PSA(T=1s): T_R=475 years (sx) and 2475 years (dx)

For each of the four events, elastic spectra recorded by the station with highest PGA are compared with the median response spectrum provided by the Ambraseys et al. (1996) GMPE and with the corresponding 16th and 84th percentile interval (rupture mechanism is accounted for according to Bommer et al. 2003). In the same plot, elastic spectra are also compared with the design spectra provided by the NTC at the corresponding sites. Selected stations are NRC, CMI, CMI and FCC[5] for the M6.0, M5.4, M5.9 and M6.5 event, respectively. Comparisons are reported in the following figures.

[5] It is worth noting that records from some RAN stations (FCC, PRE and RQT) are currently under technical revisions and are not available on the online databases. However, FCC records, which to the authors seem to have no problems are shown here. If confirmed, FCC records are the strongest recorded in Italy to date.

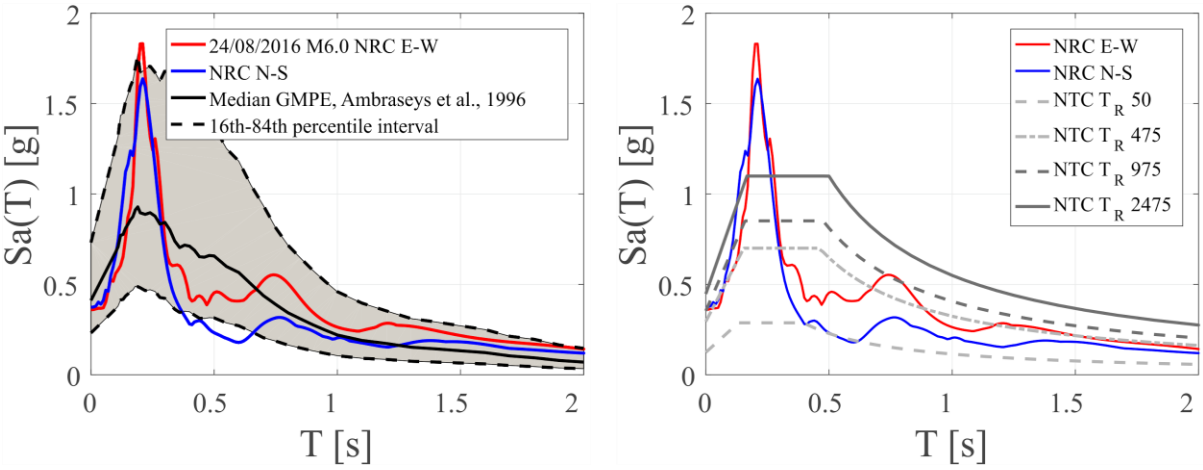

Figure 9.4. Comparison between elastic pseudo-acceleration response spectra of the NRC station (event M6.0) and GMPE (left) and elastic code spectra from NTC2008 (soil B) (right)

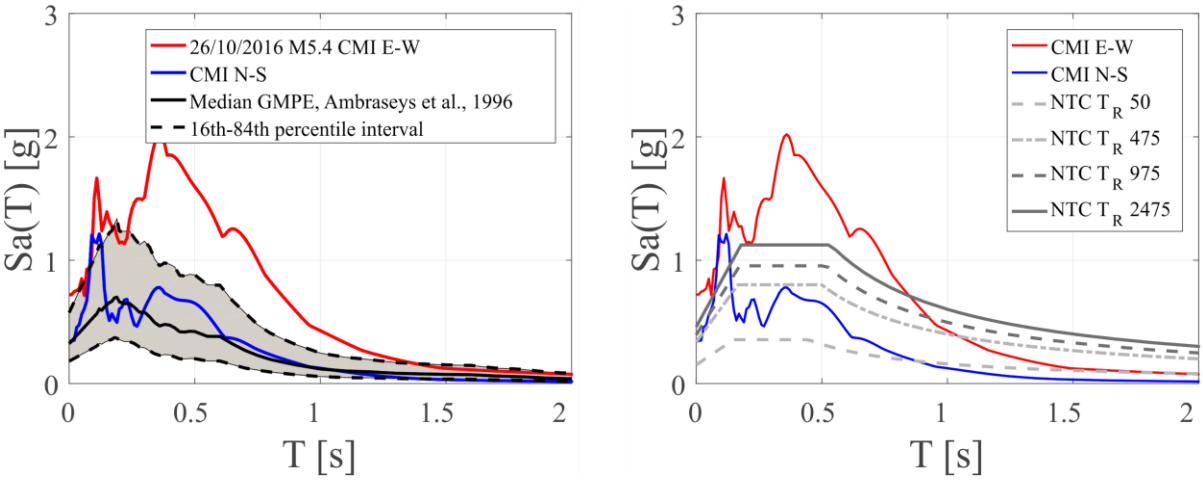

Figure 9.5. Comparison between elastic pseudo-acceleration response spectra of the CMI station (event M5.4) and GMPE (left) and elastic code spectra from NTC2008 (soil C) (right)

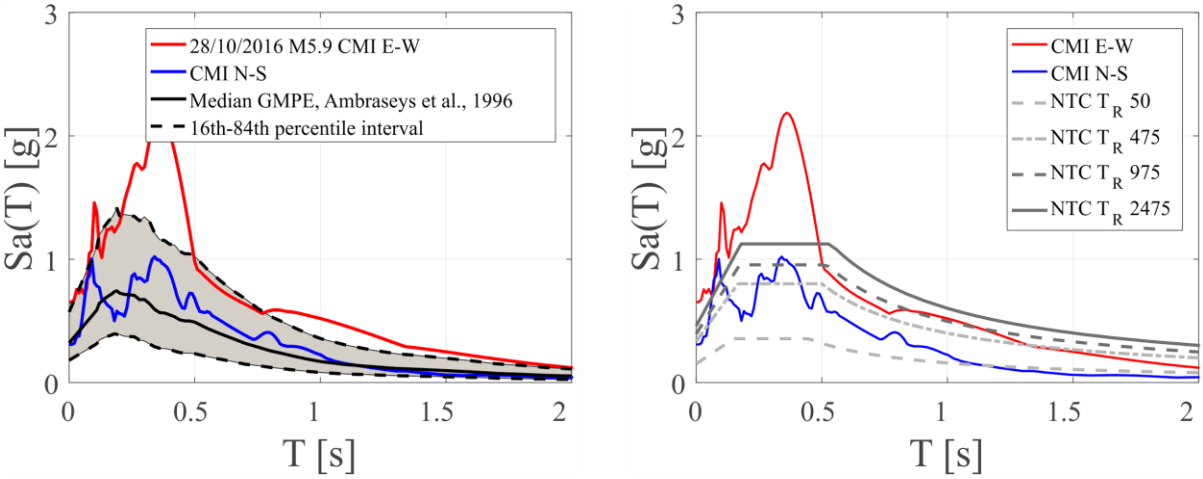

Figure 9.6. Comparison between elastic pseudo-acceleration response spectra of the CMI station (event M5.9) and GMPE (left) and elastic code spectra from NTC2008 (soil C) (right)

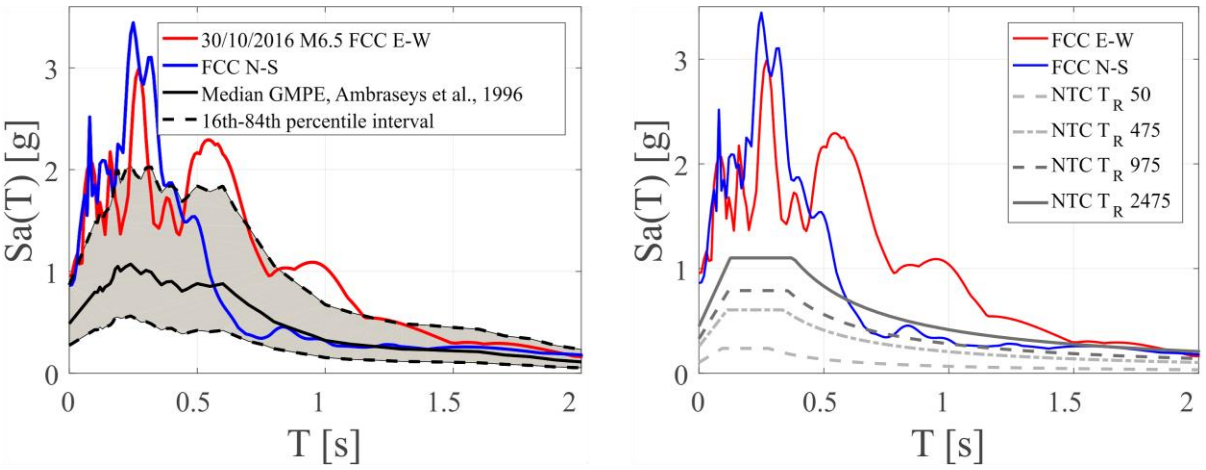

Figure 9.7. Comparison between elastic pseudo-acceleration response spectra of the FCC station (event M6.5) and GMPE (left) and elastic code spectra from NTC2008 (soil A) (right)

10. Pulse-like near-source ground motions

Pulse-like near-source ground motions may be the result of rupture directivity, a phenomenon that may lead seismic waves generated at different points along the rupture front to arrive at a near-source site simultaneously. This can lead to a constructive wave interference effect, which is manifested in the form of a double-sided velocity pulse that delivers most of the seismic energy early in the record (Somerville et al., 1997). Such impulsive behaviour of near-source ground motions has been probably found in Italian seismic events of normal faulting style before (e.g., L'Aquila 2009 M_w6.3 event – see Chioccarelli and Iervolino, 2010). In this preliminary investigation for such rupture directivity effects, the continuous wavelet transform algorithm suggested by Baker (2007) was implemented for all recordings (horizontal components) of the four principal events (24/08/2016 M_w6.0, 26/10/2016 M_w5.4, 26/10/2016 M_w5.9, 30/10/2016 M_w6.5) within an epicentral distance of 50km and for all orientations. The parameters of the preliminary finite-fault geometry used are available at http://esm.mi.ingv.it (for the time is being source models for the 24/08/2016 M_w6.0 and the 30/10/2016 M_w6.5 events are attributed to Tinti et al. 2016, personal communication by E.Tinti). A map of the various epicenters along with the stations for which noteable pulses we detected in the strike-normal (fault-normal, FN) component, can be seen in Figure 10.1 (note that no impulsive ground motions were detected in the case of the 26/10/2016 M_w5.9 shock).

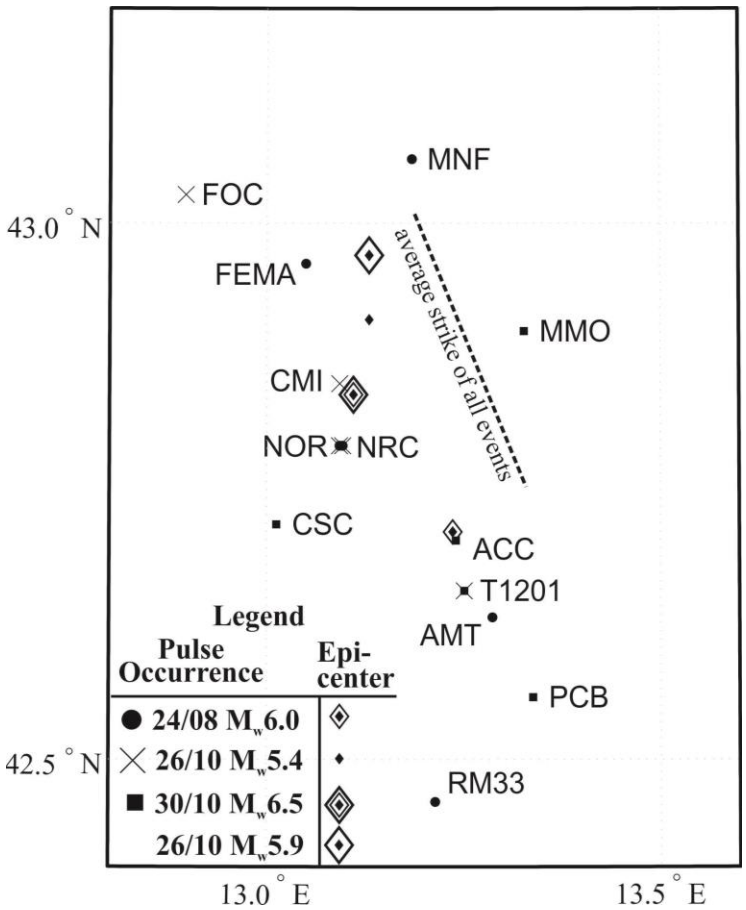

Figure 10.1. Surface projection of rupture plane; province borders and some NS stations shown on the map.

Another general overview is offered by Figure 10.2, where extracted pulse periods from all shocks are compared with an empirical regression model for pulse duration (Baltzopoulos et al., 2016).

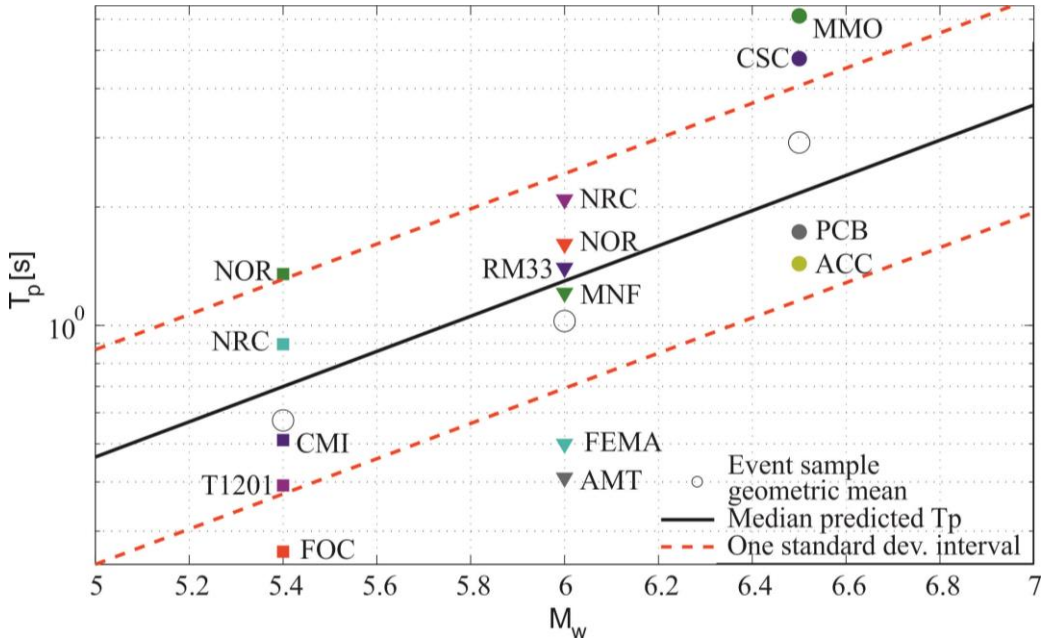

Figure 10.2. Extracted pulses' durations (periods T_p) shown against median prediction and $\pm\sigma$ interval (Baltzopoulos et al., 2016 model).

Out of all the records investigated belonging to the 24/08/2016 M_w6.0 shock, the six ground motions recorded at Amatrice (AMT), Norcia (NRC), Norcia Le Castellina (NOR), Montereale (RM33), Monte Fema (FEMA) and Fiastra (MNF) exhibited impulsive characteristics over a multitude of orientations, as expressed by a Pulse Indicator (PI) score in excess of 0.85 (see Baker, 2007). The record at Amatrice revealed two distinct pulses, one being predominant in the fault-normal (FN) and the other longer pulse in the fault-parallel (FP) direction. The FN pulse has a pulse period T_p of 0.40s while the FP 0.98s. The Norcia record on the other hand was found to contain a 2.09s period pulse mostly towards orientations that lie between the FN and FP without being decidedly prevalent in any of the perpendicular/parallel directions to the strike. Note that some deviation of directivity pulses from the strictly FN orientation is not unheard of in dip-slip faulting. Finally, the ground motions recorded at the stations of Fiastra and Montereale were found to contain pulses in the FN direction with T_p of 1.4s and 1.2s respectively, also hinting at rupture directivity effects, despite the lower velocity amplitude due to the greater distance from the fault and consequent attenuation.

In the following Figures, a polar plot is presented for each station displaying the PI score per azimuth as well as the velocity time histories at the most relevant directions (original signal and extracted pulse superimposed).

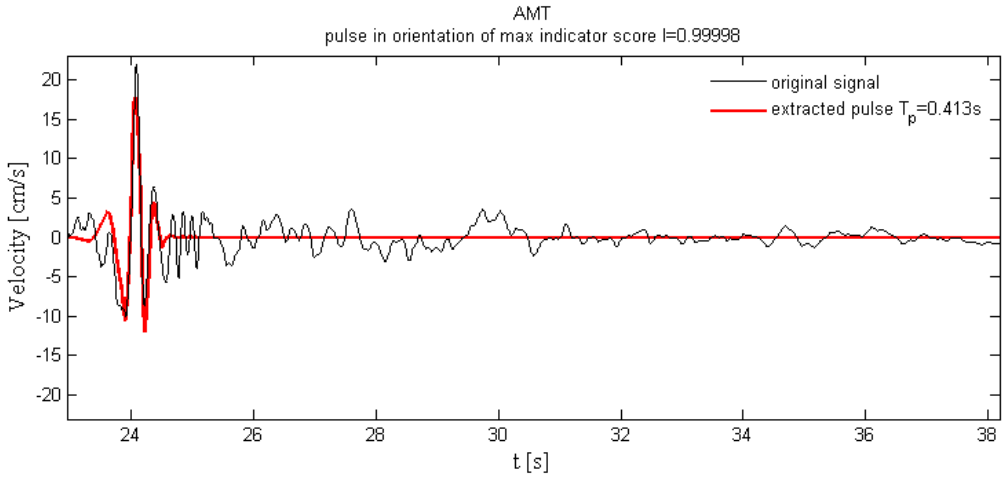

Figure 10.3 Original velocity time-history and CWT extracted pulse and residual signal for the fault-normal component of the Amatrice record - 24/08/2016 M_w6.0 event.

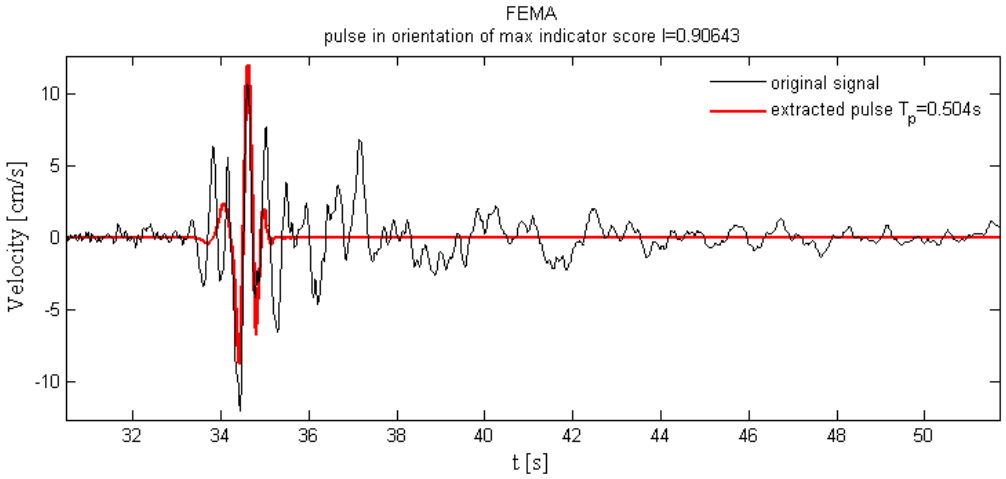

Figure 10.4 Original velocity time-history and CWT extracted pulse and residual signal for the fault-normal component of the Monte Fema record - 24/08/2016 M_w6.0 event.

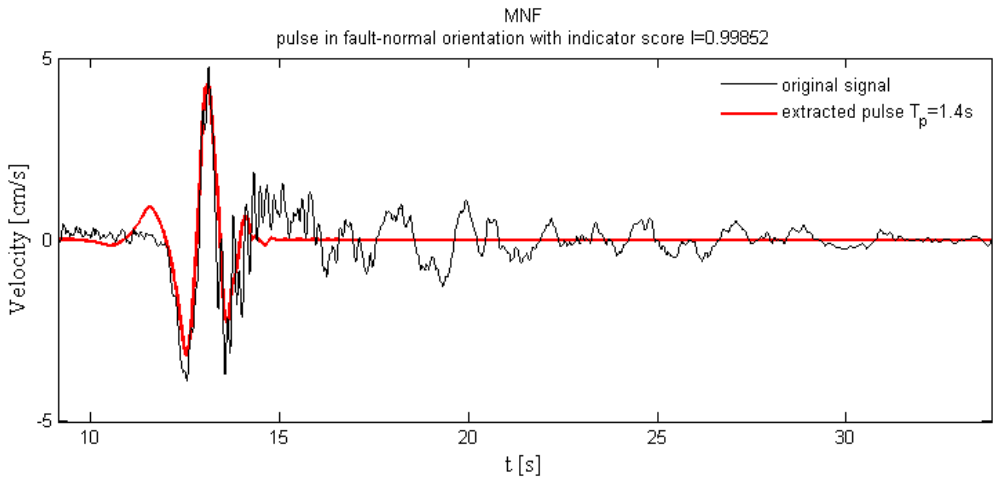

Figure 10.5 Original velocity time-history and CWT extracted pulse and residual signal for the fault-normal component of the Fiastra record - 24/08/2016 M_w6.0 event.

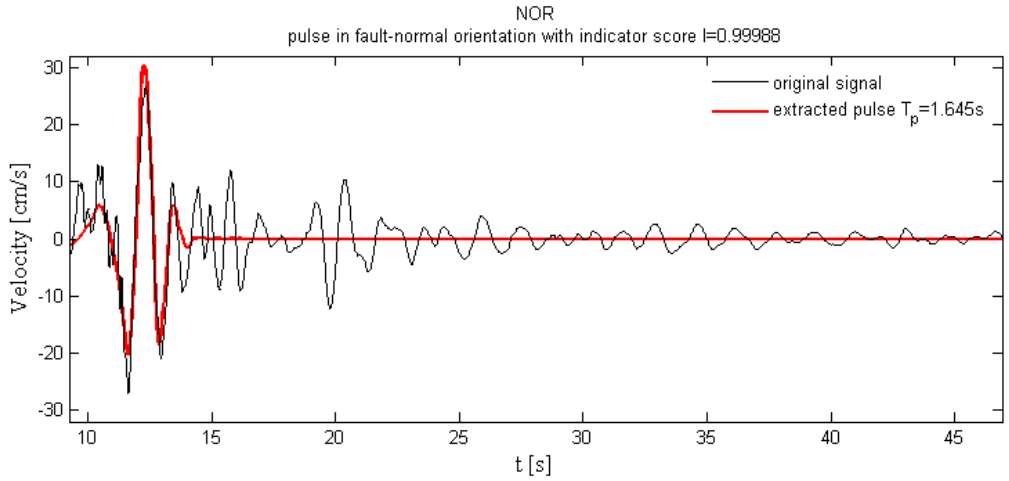

Figure 10.6 Original velocity time-history and CWT extracted pulse and residual signal for the fault-normal component of the Norcia (Le Castellina) record - 24/08/2016 M_w6.0 event.

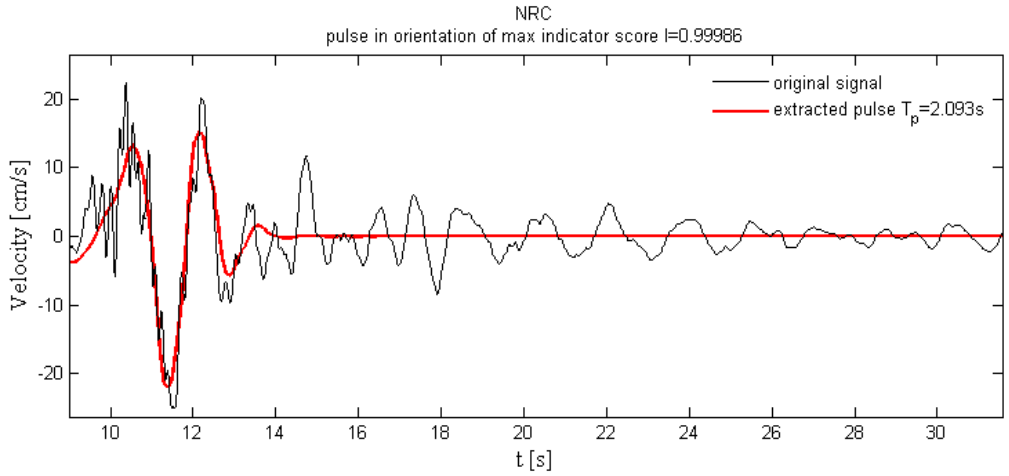

Figure 10.7 Original velocity time-history and CWT extracted pulse and residual signal for the fault-normal component of the Norcia (NRC) record - 24/08/2016 M_w6.0 event.

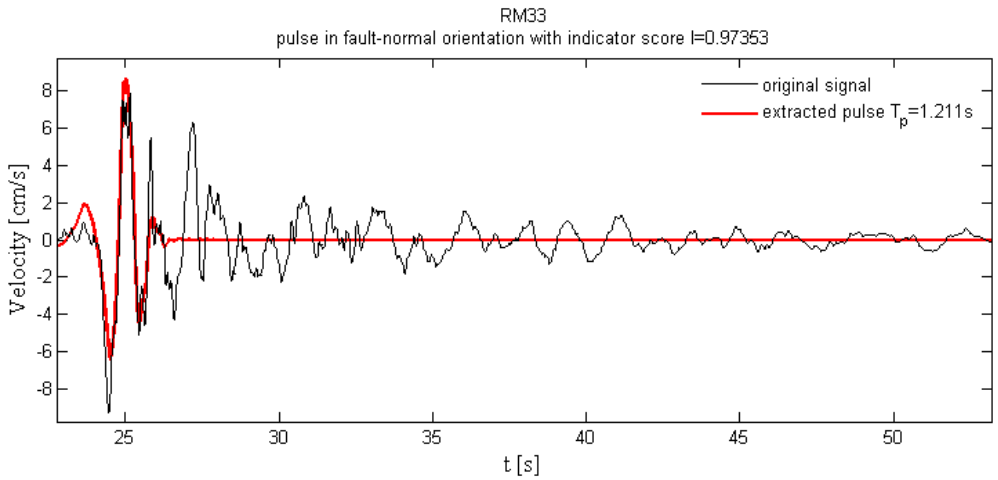

Figure 10.8 Original velocity time-history and CWT extracted pulse and residual signal for the fault-normal component of the Monte Reale record - 24/08/2016 M_w6.0 event.

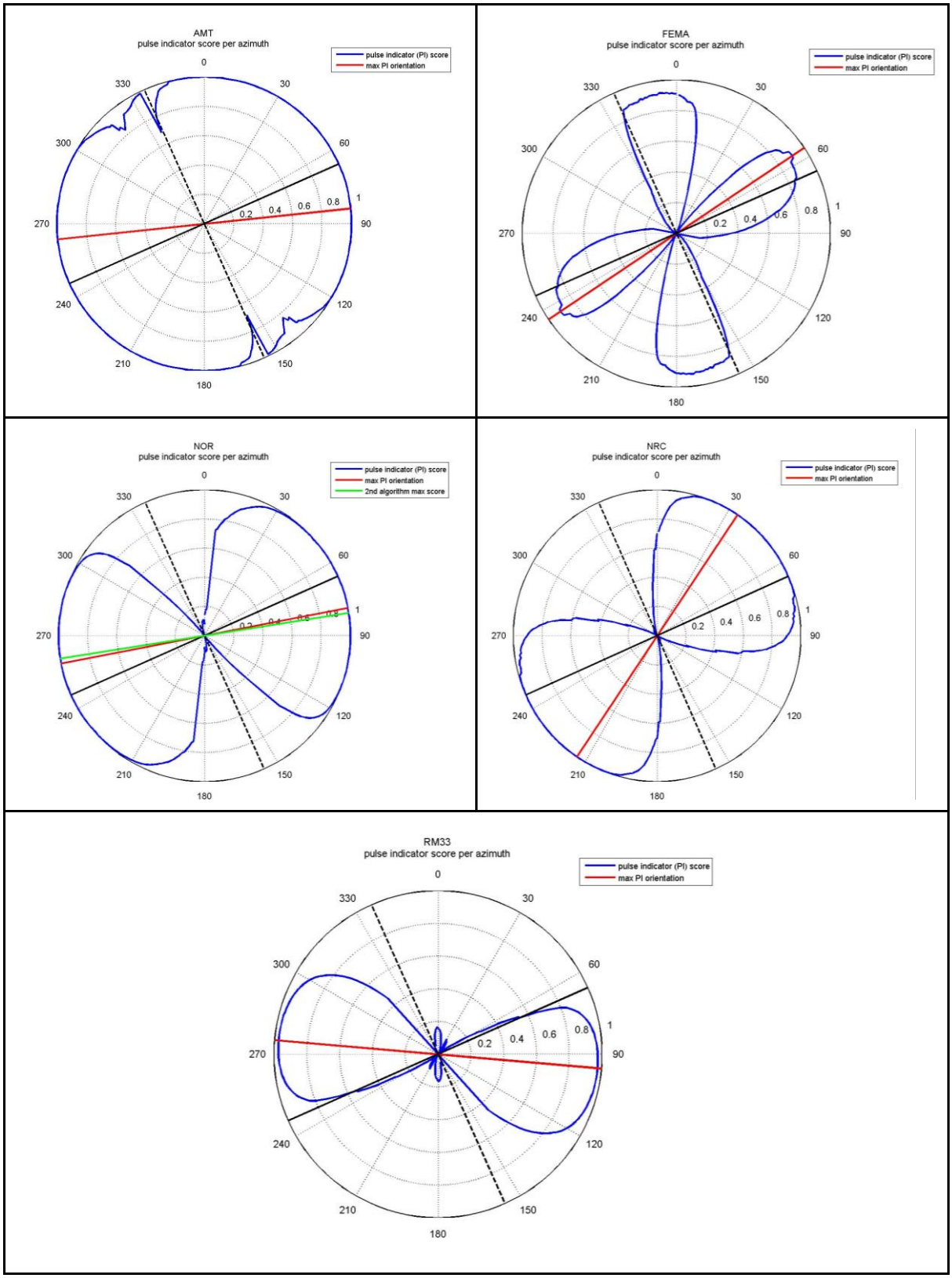

Figure 10.9. Polar plots of pulse indicator score per azimuth for the 24/08/2016 M_w6.0 event records.

Another point of interest is a comparison of the impulsive velocity traces recorded within the vicinity of Norcia (accelerometric stations NRC and NOR) with the signals recorded at the base of two nearby structures under seismic monitoring by the Italian National Civil Protection (data available at http://www.mot1.it/ossdownload/). Figure 10.10 attests to the fact that the observed pulses are not localized site-specific occurrences, but seem to affect a wider area. This observation, in combination with the fact that such pulses were not observed at these locations during the subsequent M_w5.9 and M_w6.5 events , lends more credibility to the assumption that these impulsive features are more likely linked to rupture directivity[6].

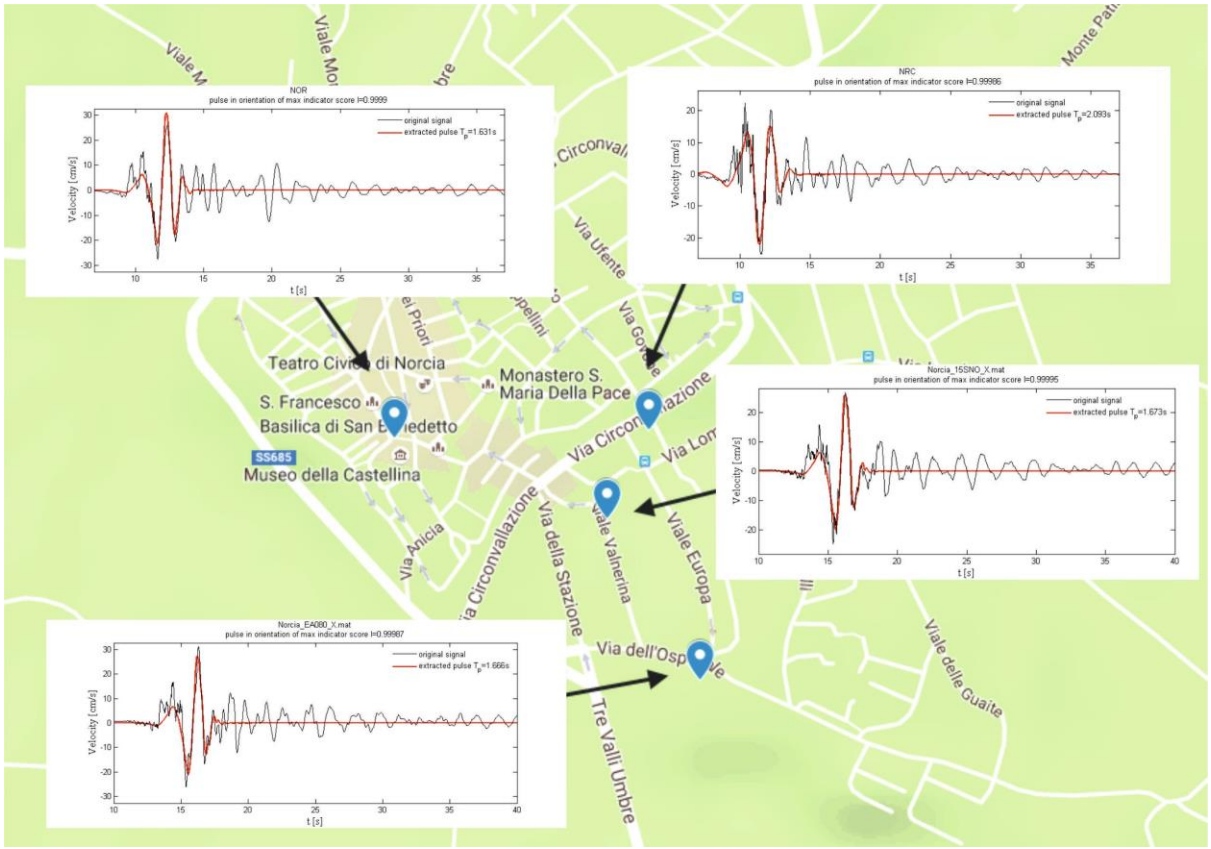

Figure 10.10. Coherence of impulsive velocity traces recorded in the vicinity of Norcia during the 24/08/2016 M_w6.0 event.

During the 26/10/2016 M_w5.9 event, none of the 45 NS records examined revealed pulses that could be reasonably related to rupture directivity effects. This is an important result regardless, given that such pulses were detected in prior and subsequent events in this sequence, as it reinforces the level of confidence that NS pulses actually extracted from the other events are related to rupture directivity rather than to some consistent site-related effect (this is also a good point for a reminder that constructive interference leading to coherent pulses in the NS region is governed by a certain amount of uncertainty and cannot be taken for granted a priori - see Iervolino and Cornell, 2008).

[6] It should be underlined that these are preliminary conclusions based on data available at this time and maybe subject to reappraisal as the accelerometric records at Norcia are under scrutiny regarding polarity and orientation of the sensors.

On the other hand, examination of the 26/10/2016 M_w5.4 event revealed some notable FN pulses, albeit of briefer duration than those detected during the M_w6.0 and M_w6.5 shocks. However, this is to be expected, as pulse duration is known to scale with magnitude (see Figure 10.2) as it has been proposed that it is connected to rise-time of co-seismic slip.

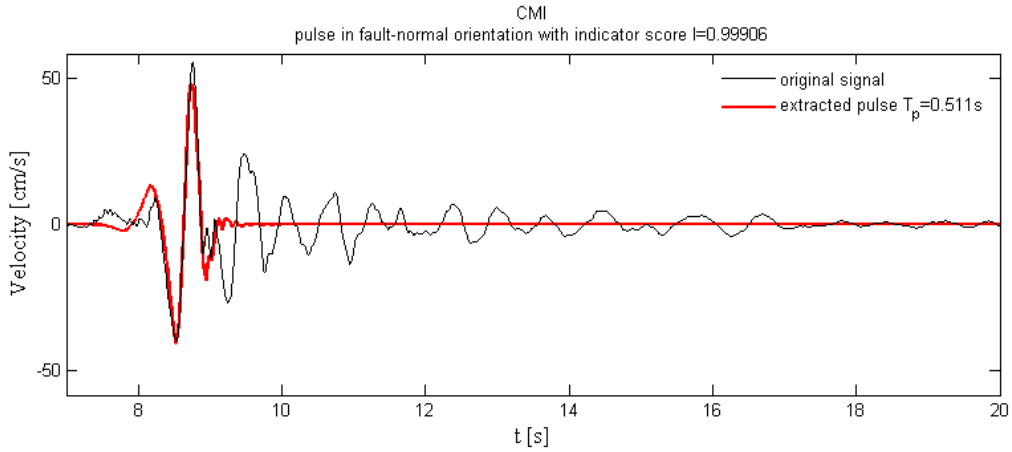

Figure 10.11. Original velocity time-history and CWT extracted pulse and residual signal for the fault-normal component of the Campi record - 26/10/2016 M_w5.4 event.

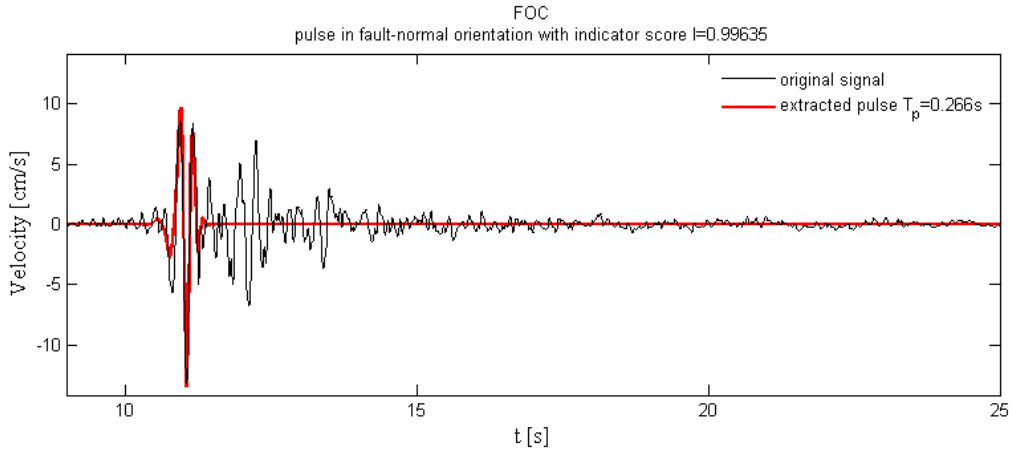

Figure 10.12. Original velocity time-history and CWT extracted pulse and residual signal for the fault-normal component of the FOC record - 26/10/2016 M_w5.4 event.

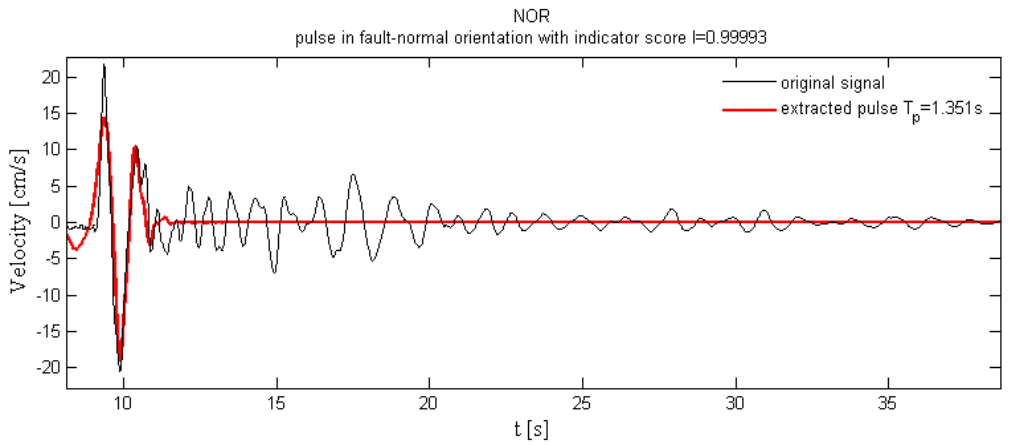

Figure 10.13. Original velocity time-history and CWT extracted pulse and residual signal for the fault-normal component of the Norcia Le Castellina (NOR) record - 26/10/2016 M_w5.4 event.

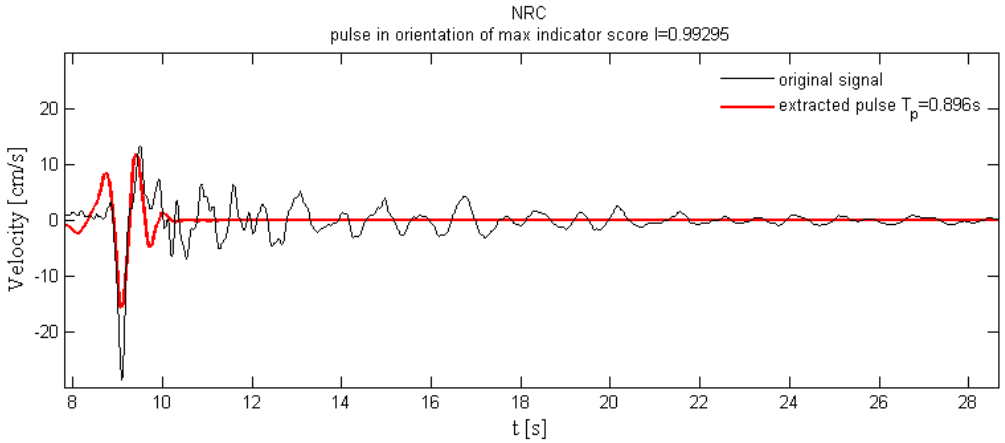

Figure 10.14. Original velocity time-history and CWT extracted pulse and residual signal for the fault-normal component of the Norcia (NRC) record - 26/10/2016 M_w5.4 event.

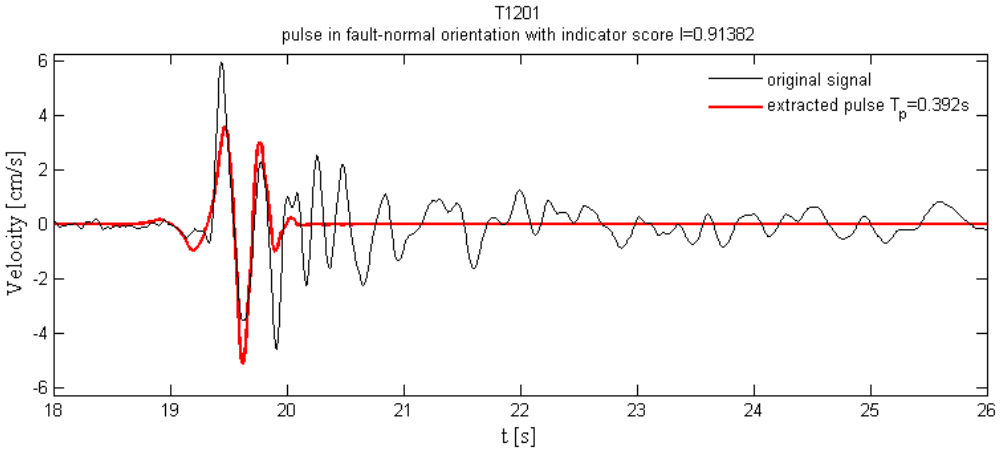

Figure 10.15. Original velocity time-history and CWT extracted pulse and residual signal for the fault-normal component of the mobile station T1201 record - 26/10/2016 M_w5.4 event.

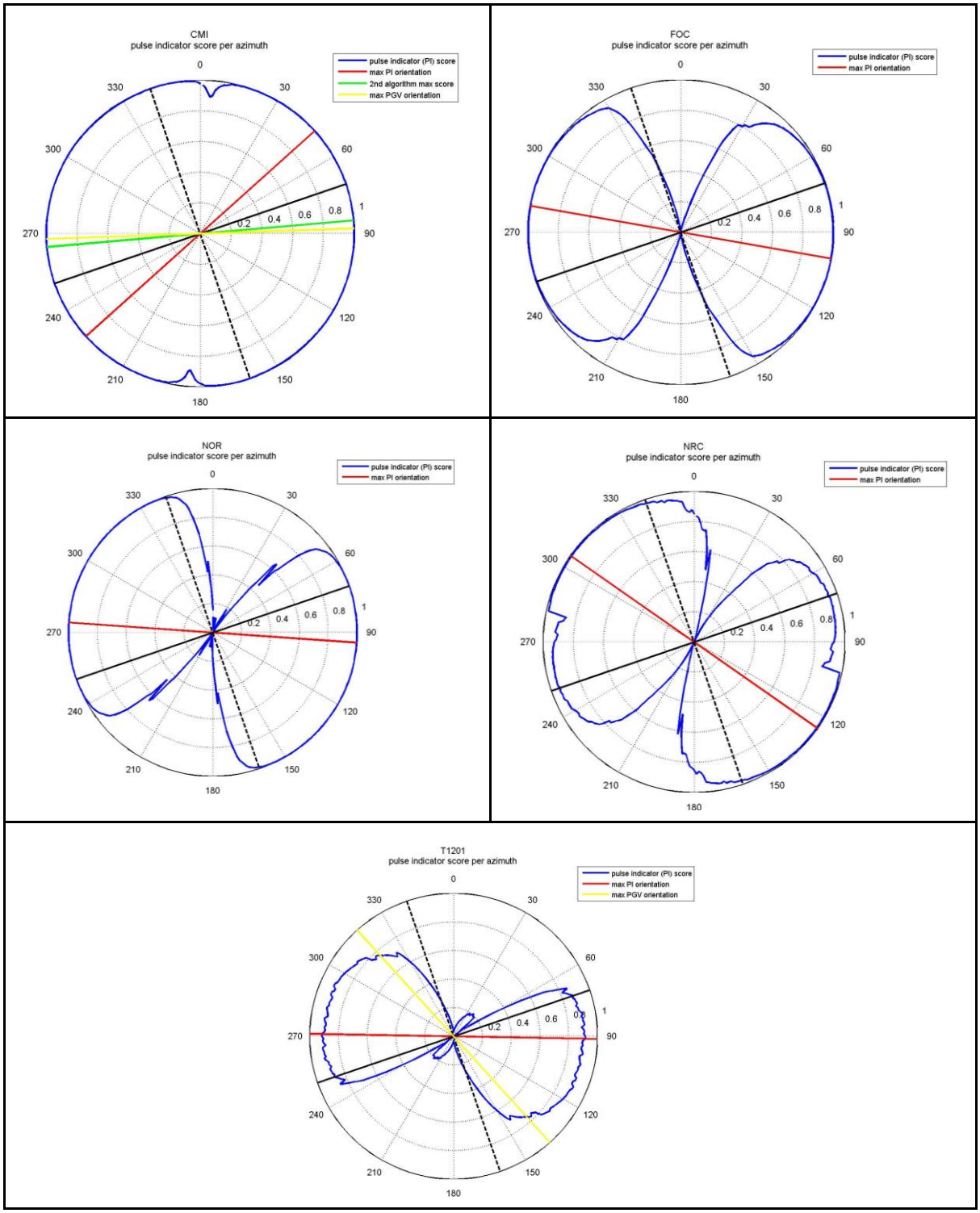

Figure 10.16. Polar plots of pulse indicator score per azimuth for the 26/10/2016 M_w5.4 event records.

Finally, a preliminary examination of about 60 ground motions recorded during the 30/10/2016 M_w6.5 event, revealed three groups of noteworthy NS pulses. Two very clear medium-duration pulses at the Accumoli and PCB stations, two long-duration pulses at the CSC and MMO stations and a very prominent FP-oriented impulsive velocity trace at the mobile station T1201 (pulses in the fault-parallel direction are not generally to be expected due to rupture directivity, but this particular waveform was deemed interesting enough to be reported here).

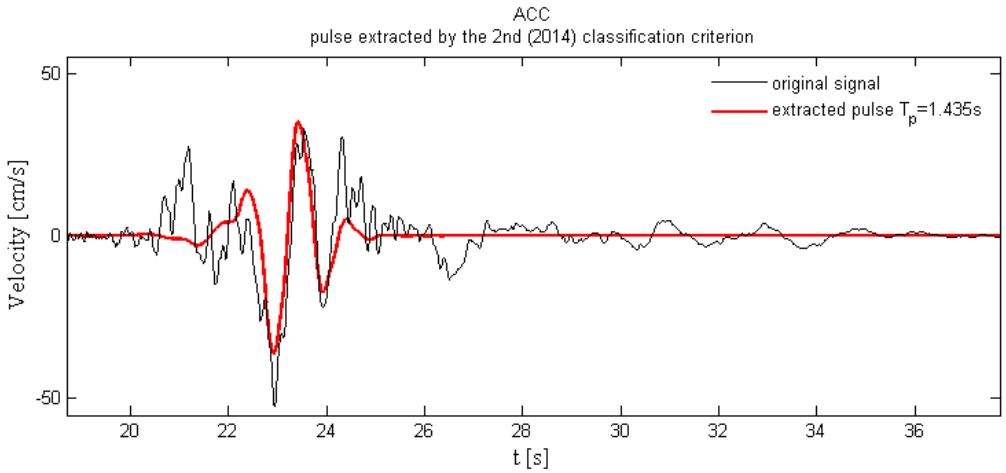

Figure 10.17. Original velocity time-history and CWT extracted pulse and residual signal for the quasi- fault-normal component of the Accumoli record - 30/10/2016 M_w6.5 event.

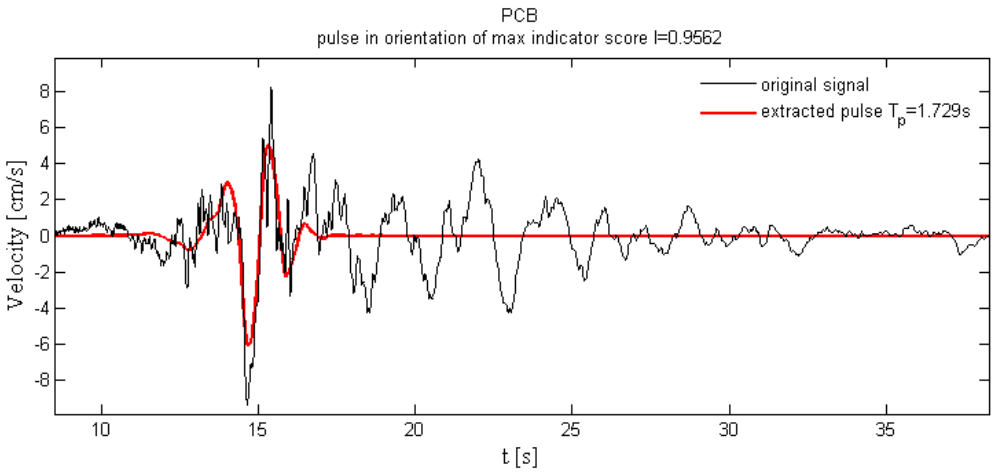

Figure 10.18. Original velocity time-history and CWT extracted pulse and residual signal for the quasi- fault-normal component of the PCB record - 30/10/2016 M_w6.5 event.

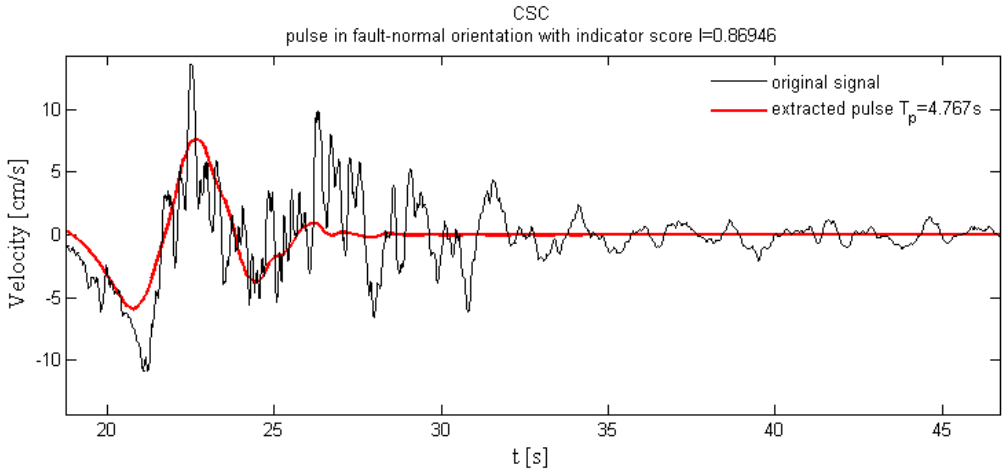

Figure 10.19. Original velocity time-history and CWT extracted pulse and residual signal for the fault-normal component of the CSC record - 30/10/2016 M_w6.5 event.

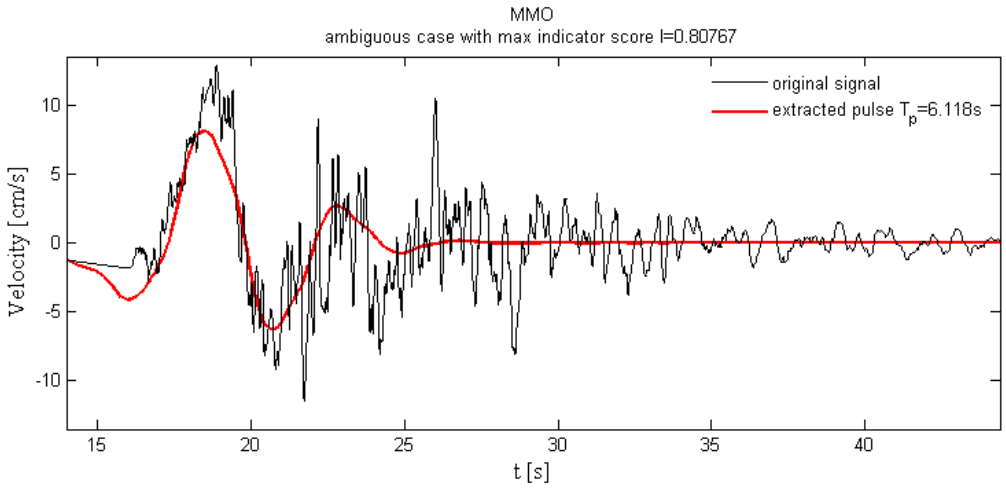

Figure 10.20. Original velocity time-history and CWT extracted pulse and residual signal for the fault-normal component of the MMO record - 30/10/2016 M_w6.5 event.

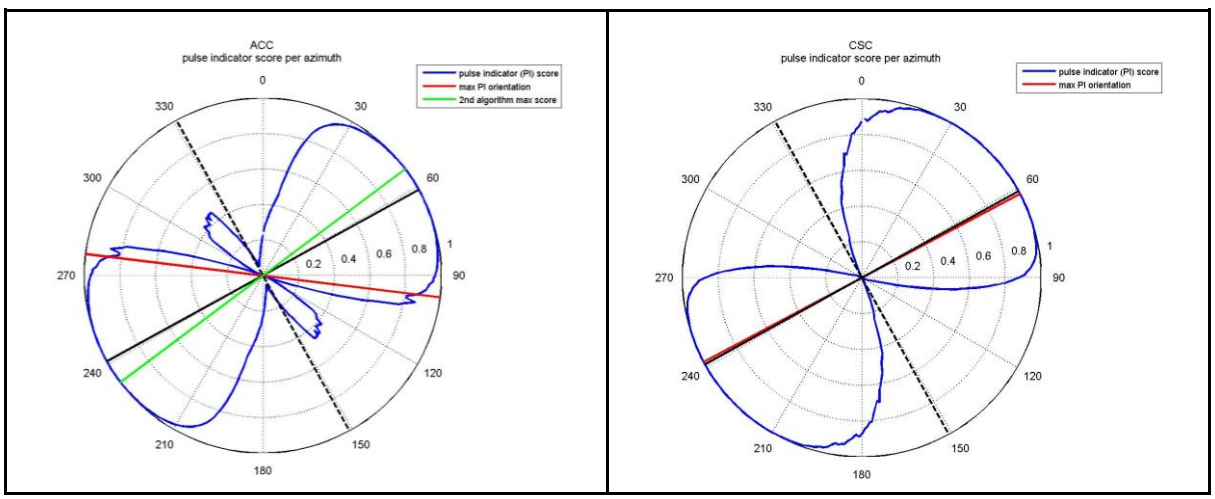

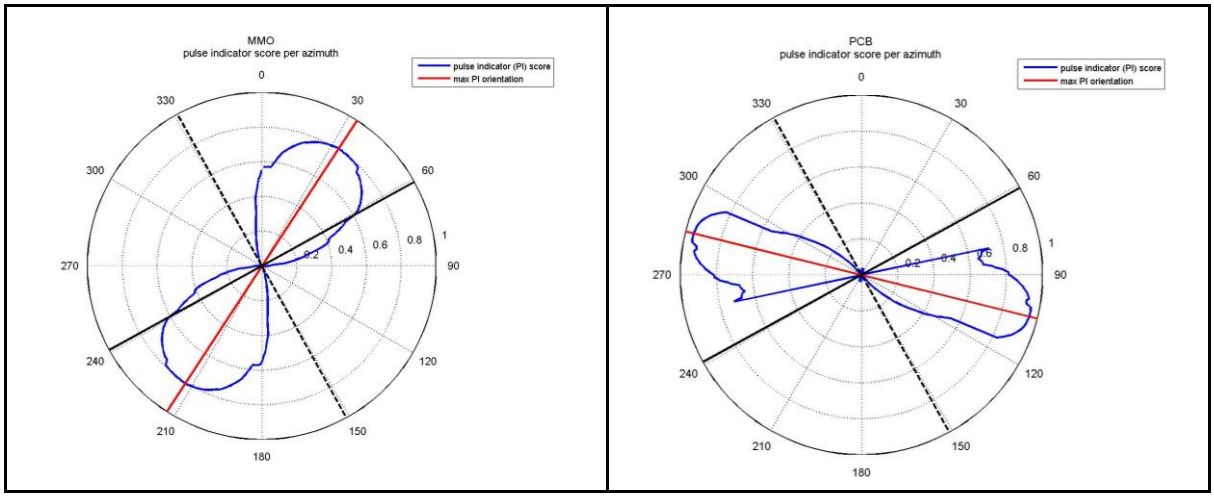

Figure 10.21. Polar plots of pulse indicator score per azimuth for the 30/10/2016 M_w6.5 event records.

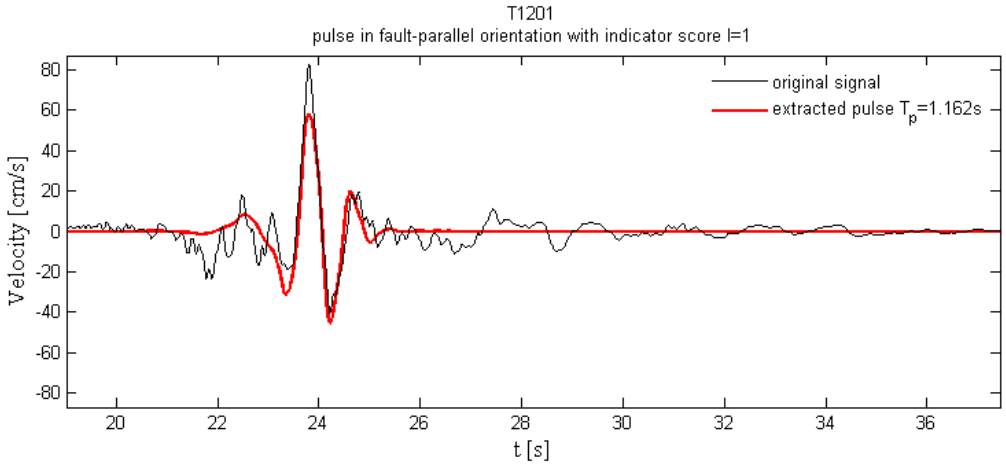

Figure 10.22. Original velocity time-history and CWT extracted pulse and residual signal for the fault-parallel component of the mobile station T1201 record - 30/10/2016 M_w6.5 event.

11. Illustration (example) of damage accumulation during the sequence on a single degree of freedom system

In this illustrative example of cumulative structural damage, we consider a simplified structure consisting of a single degree of freedom (SDoF) non-linear oscillator, subjected to an actual recorded sequence of strong ground motion. The structure is assumed located at Norcia and the accelerograms employed in the analysis are (both horizontal components of) the four NRC station recordings (event dates can be seen in Figures 11.1, 11.2). The SDoF structural system is characterized by a natural vibration period of 0.40s, a yield acceleration of 0.30g and a quadrilinear monotonic backbone (static pushover) exhibiting post-yield hardening ratio of 20%, capping ductility (ratio of displacement at onset of strength degradation to yield displacement) of 5.0, post-capping (negative-slope) stiffness ratio of 50% and a residual strength plateau equal to 50% of yield strength (backbone curve can be seen in Figures 11.1, 11.2 as dashed-line envelopes of the hysteresis loops). Fracture ductility is set at 8.0 and hysteretic behavior is governed by a peak-oriented model that does not include cyclic degradation.

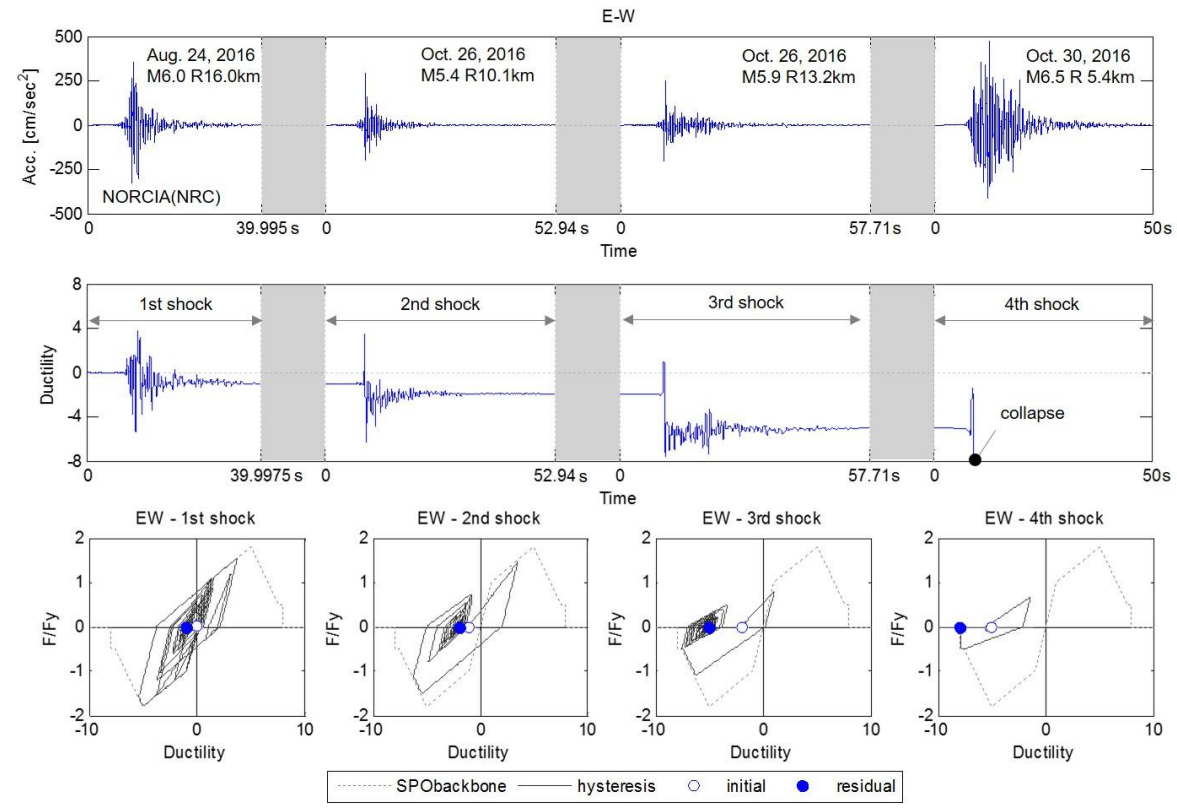

Figure 11.1 Earthquake sequence and time history responses in EW;
(top): seismic sequence; (middle): ductility; (bottom): hysteresis loop at each shock.

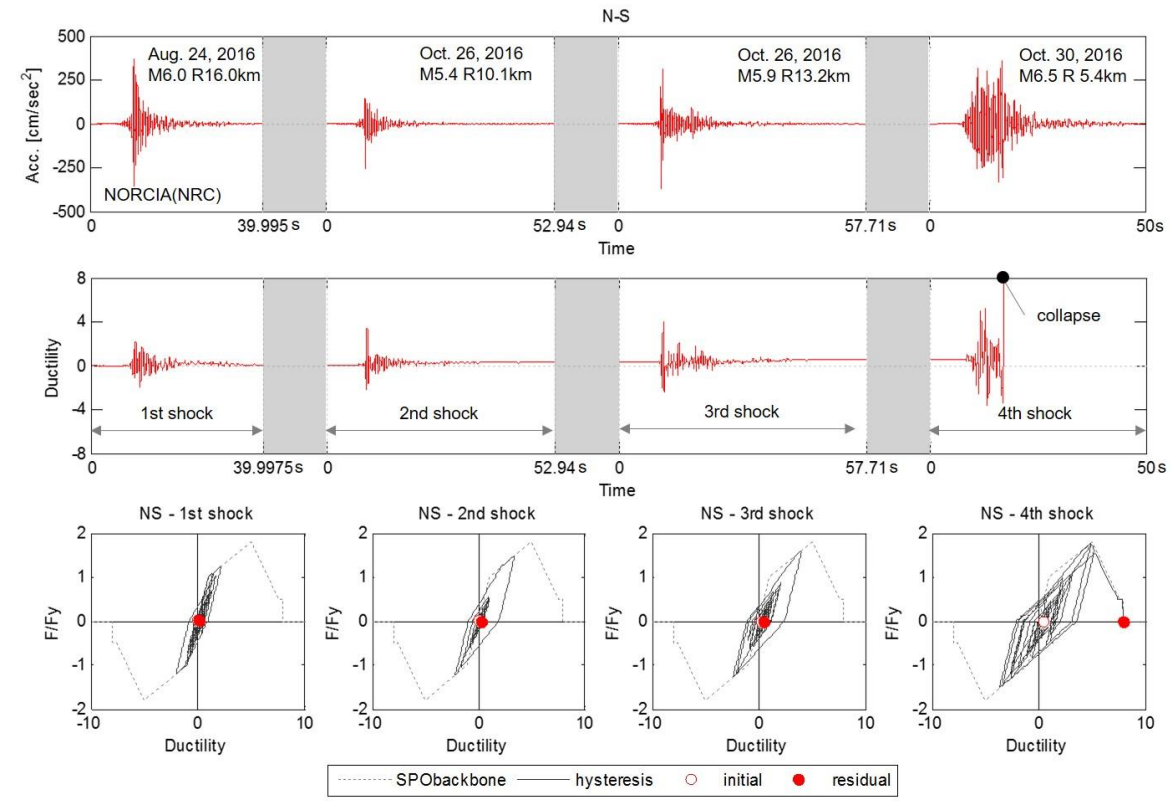

Figure 11.2. Earthquake sequence and time history responses in NS ;
(top): seismic sequence; (middle): ductility; (bottom): hysteresis loop at each shock.

It can be observed in Figure 11.1 (cumulative response to the EW component of the sequence recorded at NRC) that the first three shocks cause considerable residual drift to accumulate in the example structure, while the fourth shock leads to rapid collapse after hardly a single hysteretic cycle, due to the notable loss of strength experienced during the second and third shock. In fact, the large inelastic excursion experienced at the very beginning of the second accelerogram could be related to its impulsive nature (note that the EW component is oriented more towards the fault-normal - see previous section). On the other hand, in Figure 11.2 (cumulative response to the NS component of the sequence recorded at NRC) the accumulation of residual deformations is less noticeable than for the EW component and the arrival of the fourth shock leads to a more prolonged hysteretic response but one that leads to eventual collapse nonetheless, due to the consistently high acceleration amplitude of the fourth record over many cycles.

Data and resources

Manually Processed and unprocessed strong-motion records
Engineering strong-motion database: http://esm.mi.ingv.ithttp://esm.mi.ingv.it/ http://esm.mi.ingv.it/
Automatically processed and raw strong-motion records
Rapid response Strong Motion database http://www.orfeus-eu.org/opencms/rrsm/http://www.orfeus-eu.org/opencms/rrsm/ http://www.orfeus-eu.org/opencms/rrsm/
Raw strong-motion records
European Integrated Data Archive http://www.orfeus-eu.org/data/eida/
Italian Department of Civil Protection: http://ran.protezionecivile.it/ , http://www.mot1.it/ossdownload/
Shakemaps
Italy ShakeMaps http://shakemap.rm.ingv.it/http://shakemap.rm.ingv.it/ http://shakemap.rm.ingv.it/
Real time earthquake catalogue
ISIDe - Italian Seismological Instrumental and Parametric Database http://iside.rm.ingv.ithttp://iside.rm.ingv.it/ http://iside.rm.ingv.it/
Historical catalogue
Catalogo Parametrico dei Terremoti Italiani **http://emidius.mi.ingv.it/CPTI/**http://emidius.mi.ingv.it/CPTI/ http://emidius.mi.ingv.it/CPTI/
Macroseismic data
Database macrosismico Italiano http://emidius.mi.ingv.it/CPTI15-DBMI15/http://emidius.mi.ingv.it/CPTI15-DBMI15/

References

Ambraseys NN, Simpson KA, Bommer JJ. (1996) Prediction of horizontal response spectra in Europe. Earthquake Engineering and Structural Dynamics, 25:371–400.

Baker J.W. (2007) Quantitative Classification of Near-Fault Ground Motions Using Wavelet Analysis. Bulletin of the Seismological Society of America, 97(5):1486–1501.

Baltzopoulos G., Vamvatsikos D., Iervolino I. (2016) Analytical modelling of near-source pulse-like seismic demand for multi-linear backbone oscillators. Earthquake Engineering and Structural Dynamics. 45(11): 1797–1815.

Bindi, D., F. Pacor, L. Luzi, R. Puglia, M. Massa, G. Ameri, and R. Paolucci (2011). Ground motion prediction equations derived from the Italian strong motion database, Bull. Earthq. Eng. 9, 1899–1920.

Bommer, J. J., J. Douglas, and F. O. Strasser (2003). Style-of-faulting in ground-motion prediction equations, Bull. Earthq. Eng. 1, 171–203.

Chioccarelli E., Iervolino I. (2010). Near-Source Seismic Demand and Pulse-Like Records: a Discussion for L'Aquila Earthquake. Earthquake Engineering and Structural Dynamics. 39(9):1039–1062.

Faenza, L., and A. Michelini (2010), Regression analysis of MCS intensity and ground motion parameters in Italy and its application in ShakeMap, Geophys. J. Int, 180(3), 1138–1152, doi:10.1111/j.1365-246X.2009.04467.x.

Faenza, L., and A. Michelini (2011), Regression analysis of MCS intensity and ground motion spectral accelerations (SAs) in Italy, Geophys. J. Int, 1–16, doi:10.1111/j.1365-246X.2011.05125.x.

Iervolino I. (2013). Probabilities and fallacies: why hazard maps cannot be validated by individual earthquakes. Earthquake Spectra, 29(3): 1125–1136.

Iervolino I., Cornell C.A. (2008). Probability of occurrence of velocity pulses in near-source ground motions. Bulletin of the Seismological Society of America, 98(5): 2262-2277.

Iervolino I., Chioccarelli E., Convertito V. (2011). Engineering design earthquakes from multimodal hazard disaggregation, Soil Dynamics and Earthquake Engineering, 31, 1212-1231.

Iervolino I., Galasso C., Cosenza E. (2010). REXEL: computer aided record selection for code based seismic structural analysis, Bulletin of Earthquake Engineering, 8, 339-362.

Michelini, A., Faenza, L., Lauciani, V., & Malagnini, L. (2008). ShakeMap implementation in Italy. Seismological Research Letters, 79(5), 689–698. http://doi.org/10.1785/gssrl.79.5.689

Paolucci, R., F. Pacor, R. Puglia, G. Ameri, C. Cauzzi, and M. Massa (2011). Record processing in ITACA, the new Italian strong motion database, in Earthquake Data in Engineering Seismology, Geotech- nical, Geological and Earthquake Engineering Series, S. Akkar, P. Gulkan, and T. Van Eck (Editors), Vol. 14(8), 99–113.

Scognamiglio, L., E. Tinti, and A. Michelini (2009), Real-Time Determination of Seismic Moment Tensor for the Italian Region, BULLETIN OF THE SEISMOLOGICAL SOCIETY OF AMERICA, 99(4), 2223–2242.

Somerville P.G., Smith N.F., Graves R.W., Abrahamson N.A. (1997) Modification of empirical strong ground motion attenuation relations to include the amplitude and duration effects of rupture directivity. Seismological Research Letters, 68:199–222.

Tinti, E., Scognamiglio, L., Michelini A. and Cocco M. (2016), Slip heterogeneity and directivity of the ML 6.0, 2016, Amatrice earthquake estimated with rapid finite-fault inversion, 1–8, doi:10.1002/(ISSN)1944-8007.

Appendix 1

Stations highlighted in gray are not used in the analysis; asterisk following EC8 site classification indicates that the classification is based on inferred, rather than measured, $V_{s,30}$.

Net code	Station code	EC8 class.	Station latitude	Station longitude
BA	PZUN	B*	40.6458	15.807
FR	SMPL	A*	42.094	9.285
IT	0CAN		43.4723	12.6308
IT	AMT	B*	42.63246	13.28618
IT	ANB	B*	43.59229	13.50741
IT	ANT	A*	42.41811	13.0786
IT	AQF	B*	42.38054	13.35474
IT	AQK	B	42.34497	13.40095
IT	AQV	B	42.37722	13.34389
IT	ASP	C*	42.848	13.6479
IT	ATN	A*	41.62032	13.80115
IT	AVL	C*	40.92283	14.78704
IT	AVZ	C	42.02746	13.42593
IT	BCN	C*	40.63435	15.38238
IT	BGR	B*	43.88951	11.99129
IT	BNE	C*	41.12756	14.78488
IT	BRS	A*	42.32427	13.59007
IT	BSS	B*	42.19173	13.84527
IT	BTT2	D	41.99833	13.54306
IT	BVG	C	42.93237	12.61107
IT	BZZ	B	42.33703	13.46858
IT	CCT	C*	43.3683	12.2346
IT	CER	B*	41.2595	15.9102
IT	CLF	D	43.03671	12.92043
IT	CLN	B*	42.08522	13.52072
IT	CMB	B*	41.5628	14.6523
IT	CME	A*	43.9543	10.3012
IT	CPS	B	42.27162	13.7583
IT	CRP	C*	44.7823	10.8703
IT	CSA	C*	43.00802	12.5906
IT	CSD	B	42.75405	12.00354
IT	CSN	B	44.13701	12.24141
IT	CSO1	B*	42.10093	13.08804
IT	CSS	B	41.48579	13.82309
IT	CTD	B*	42.38837	12.9477
IT	CTS	C*	43.49199	12.2234
IT	CVM	A*	42.99409	11.28231
IT	DUR	B*	41.6611	14.4565
IT	FAZ	C	44.29802	11.89075
IT	FBR	C*	43.3436	12.9119
IT	FIE	B*	43.80725	11.29439
IT	FMG	A*	42.26803	13.11722
IT	FOC	C*	43.0263	12.89651

IT	FOS	B*	43.01459	12.83513
IT	FRT		41.6926	13.255
IT	FSS	C*	43.69048	12.81007
IT	GBB	B*	43.35697	12.59725
IT	GBP	C	43.31381	12.58949
IT	GNU	A*	42.80382	12.57015
IT	GRN	A*	41.81346	13.31699
IT	GSA	B	42.42069	13.51936
IT	LSS	A	42.55824	12.96889
IT	MCR	C*	43.79989	12.44751
IT	MCS	B*	43.99437	12.10744
IT	MLF	B	40.9944	15.6527
IT	MMP1	B*	42.24923	12.74832
IT	MNF	A*	43.05968	13.18447
IT	MNG	A*	41.70354	15.95803
IT	MNT	A*	43.1397	11.18279
IT	MTL	B	43.24944	13.00834
IT	NAP	C*	40.79926	14.17961
IT	NCR	E	43.11158	12.78467
IT	NRC	B	42.79254	13.09648
IT	NRN	A*	42.51556	12.51944
IT	ORP	B	41.27923	15.26506
IT	PAN	B*	43.00581	12.14362
IT	PGG	B*	42.32287	13.53945
IT	PNC	B*	42.84745	11.6936
IT	PNN	C	43.81816	12.26285
IT	PSC	A	41.81204	13.7892
IT	PTI	B*	43.06657	13.65708
IT	PTL	B*	43.42733	12.4486
IT	PVF	B*	44.3331	10.82523
IT	PZI1	B*	42.4356	13.3262
IT	RDG	A*	41.9264	15.8792
IT	RQT	B*	42.81309	13.31103
IT	RTI	D	42.43028	12.8291
IT	SAG	A*	40.93156	15.18763
IT	SBC	A	41.91316	13.10552
IT	SCF	B*	42.26512	13.99849
IT	SDM	A*	42.28971	13.55765
IT	SGMA	B*	41.6845	14.9644
IT	SGPA	B	41.6876	14.9629
IT	SGPA	B	41.6876	14.9629
IT	SGSC	B*	41.6892	14.9581
IT	SGSC	B*	41.6892	14.9581
IT	SIG	C*	43.3308	12.7408
IT	SNG	C	43.68558	13.22616
IT	SNI	B*	42.632	12.5536
IT	SNM	B*	43.93433	12.44929
IT	SNS1	C*	43.5735	12.1312
IT	SOR		41.7203	13.6136
IT	SPD	B*	42.51514	13.37104
IT	SPM	A*	42.72324	12.75127
IT	SPO1		42.7344	12.7363
IT	SSC	E	42.87473	11.87679
IT	SSG	B*	43.56986	12.14632
IT	SSO		43.5715	12.154
IT	STF	B*	43.90811	11.79446
IT	SUL	A*	42.089	13.934

IT	SULA	C*	42.0734	13.9166
IT	SULC	C*	42.068	13.909
IT	SULP	B*	42.085	13.9274
IT	TLN	B*	43.2159	13.25838
IT	TOD	A*	42.73817	12.38728
IT	TRE	C*	42.8765	12.7358
IT	TRL	A*	42.46131	12.93231
IT	TRN1	D*	42.5582	12.6461
IT	TRV	B*	41.78294	14.55071
IT	TSC	A*	42.42261	11.8696
IT	TVL	B*	41.89302	12.77322
IT	UMB	B*	43.25444	12.2556
IT	VAL	B*	43.1593	12.6017
IT	VLL	B*	41.67047	12.77267
IT	VLN	C*	43.14273	11.89472
IT	VNF1	C*	41.4805	14.0501
IT	VSE	B*	42.12218	14.70719
IV	ACER	B*	40.7867	15.9427
IV	APEC	B*	43.55846	12.41991
IV	APRC		41.75738	15.54308
IV	ASOL	A*	45.8003	11.9023
IV	ATCC	B*	43.18514	12.63994
IV	ATFO	B*	43.3666	12.5715
IV	ATLO	B*	43.3152	12.4073
IV	ATPC	B*	43.4807	12.457
IV	ATTE	A*	43.1979	12.3536
IV	ATVO	B*	43.38211	12.40663
IV	BDI	B*	44.0624	10.597
IV	BIOG	B*	41.1999	15.13263
IV	BOB	B*	44.7679	9.4478
IV	BRIS	B*	44.2245	11.7666
IV	BSSO	A*	41.5461	14.5938
IV	CADA	B*	43.1942	13.7614
IV	CAFE	A*	41.028	15.2366
IV	CDCA	C*	43.4584	12.2336
IV	CERA	A*	41.5978	14.0183
IV	CIMA	B*	43.3053	13.67009
IV	CMPO	C*	44.5808	11.8056
IV	COR1	B*	43.6318	13.0003
IV	CPGN	B*	43.8011	12.3205
IV	CRMI	B*	43.7956	10.9795
IV	CRND	C*	45.8361	12.0131
IV	CTL8	C*	45.2755	9.7621
IV	FAEN	C*	44.2895	11.877
IV	FERS	C	44.9035	11.5406
IV	FIU1	B*	43.18856	12.9316
IV	FOSV	B*	43.29483	12.76117
IV	FRE8	A*	46.015	12.3552
IV	GAG1	B*	43.2381	13.0674
IV	GATE	B*	41.51315	14.9102
IV	GUMA	B*	43.0627	13.3352
IV	IMOL	C*	44.35955	11.74248
IV	LEOD	C*	45.4582	10.1234
IV	MCEL	A*	40.3249	15.8019
IV	MDAR	B*	43.1927	13.1427
IV	MELA	A*	41.7059	15.127
IV	MGAB	A*	42.91263	12.11214

IV	MGR	B*	40.1376	15.5535
IV	MNTV	C*	45.1495	10.7897
IV	MOCO	B*	41.37	15.158
IV	MODE	C*	44.6297	10.9492
IV	MRB1	B*	41.1227	14.96815
IV	MRLC	B*	40.7564	15.48892
IV	MSAG	A*	41.712	15.9096
IV	MTRZ	B*	44.3128	11.4248
IV	MURB	B*	43.263	12.5246
IV	NDIM	C*	44.8873	10.8987
IV	NEVI	B*	44.5834	10.3163
IV	NRCA	B*	42.83355	13.11427
IV	OPPE	C*	45.3082	11.1724
IV	ORZI	C*	45.4056	9.9307
IV	OSSC	B*	43.5236	11.2458
IV	PAOL	A*	41.03121	14.56749
IV	PCRO	B*	43.6077	13.5323
IV	PIEI	A*	43.53567	12.535
IV	PIGN	A*	41.2	14.17989
IV	POFI	A*	41.71743	13.71202
IV	PP3	C*	43.3778	13.6095
IV	PTRJ	A*	41.3641	14.529
IV	RM33	B*	42.509	13.2145
IV	RNI2	A*	41.70328	14.1524
IV	ROM9	B*	41.82842	12.51553
IV	ROVR	A*	45.6468	11.0721
IV	SACS	B*	42.84906	11.90967
IV	SALO	A*	45.6183	10.5243
IV	SANR	C*	45.64	11.6099
IV	SBPO	C*	45.0511	10.9199
IV	SERM	C*	45.01	11.2958
IV	SGG	A*	41.38667	14.37917
IV	SGTA	B*	41.135	15.365
IV	SIRI	B*	40.1821	15.8675
IV	SNAL	A*	40.9254	15.2091
IV	SNTG	A*	43.255	12.9406
IV	SSFR	A*	43.4363	12.7822
IV	SSM1	B*	43.22878	13.17696
IV	STAL	B*	46.2601	12.7104
IV	TERO	B*	42.62279	13.60393
IV	TRE1	B*	43.3112	13.31285
IV	TREG	C*	45.523	11.1606
IV	TRIV	B*	41.7666	14.5502
IV	VAGA	A*	41.4154	14.2342
IV	VENL	D*	45.4167	12.3765
IV	VITU	A*	41.18326	14.63015
IV	VOBA	C*	45.6429	10.504
IV	VULT	B*	40.9549	15.6163
IV	ZCCA	B*	44.35085	10.9765
IV	ZEN8	A*	45.6378	10.7319
IV	ZOVE	B*	45.4536	11.4876
MN	AQU	B*	42.35388	13.40193
MN	BLY		44.7488	17.1839
MN	CUC	A*	39.9938	15.8155
MN	VLC	A*	44.1594	10.3864
OX	ACOM		46.548	13.5137
OX	AGOR		46.2329	12.0472

OX	CGRP		45.8806	11.8047
OX	CIMO		46.3116	12.4448
OX	CLUD		46.4569	12.8814
OX	MPRI		46.2408	12.9877
OX	SABO	B*	45.9875	13.6336
OX	VARN		45.9922	12.1051
OX	ZOU2		46.5584	12.9729
ST	DOSS		45.8808	11.1884
ST	VARA	A*	45.826	10.8965